Durham E-Theses

Solar neutrino physics at dark matter direct detection experiments

REID, ELLIOTT,MACKENZIE,TAYLOR

Solar neutrino physics at dark matter direct detection experiments

Elliott Reid

A Thesis presented for the degree of
Doctor of Philosophy

Institute for Particle Physics Phenomenology
Department of Physics
Durham University
United Kingdom

July 2021

Solar neutrino physics at dark matter direct detection experiments

Elliott Reid

Submitted for the degree of Doctor of Philosophy

July 2021

Abstract: As the sensitivity of direct detection experiments improves, they will soon be subject to a new, irreducible background from the coherent elastic scattering of solar neutrinos with nuclei. The presence of new physics can modify this scattering rate, and signals of neutrino scattering may appear in direct detection experiments sooner than expected. In this thesis, we explore the effects of several simplified models of new physics on neutrino scattering at direct detection experiments. We introduce the neutrino contour, a projection of the modified coherent neutrino scattering rate on a dark matter parameter space. This contour can be used to quickly identify whether a direct detection experiment could set competitive constraints on a given model, or conversely, whether the model could produce a large enough neutrino scattering rate to hinder searches for dark matter at that experiment. We discuss the subtleties that arise while computing constraints from the results of one experiment, CDMSlite, in particular the challenges of including electron scattering in the analysis. Finally, we calculate the sensitivity of several future direct detection experiments to one model, the $U(1)_{L_\mu - L_\tau}$. We find that the upcoming LUX-ZEPLIN experiment will be able to test solutions to two ongoing problems in fundamental physics: the muon g-2 anomaly and the H_0 tension.

Contents

Declaration

The work in this thesis is based on research carried out in the Department of Physics at Durham University. No part of this thesis has been submitted elsewhere for any degree or qualification. Parts of this work are based on articles that have been published, as follows:

- Chapter 2 is partly based on Ref. [1], *"Surrogate Models for Direct Dark Matter Detection"*, published in the Journal of Cosmology and Astroparticle Physics.

- Chapter 5 is partly based on Ref. [2], *"How high is the neutrino floor?"*, published in the Journal of Cosmology and Astroparticle Physics.

- Chapter 7 is based on Ref. [3], *"Solar neutrino probes of the muon anomalous magnetic moment in the gauged $U(1)_{L_\mu - L_\tau}$"*, published in the Journal of High Energy Physics.

Additionally, parts are based on joint work that is in the process of being prepared for publication:

- Chapter 5 is partly based on Ref. [4], *"Medium effects in supernovae constraints on light mediators"* currently under review.

- Chapter 6 is based on my contribution to ongoing work with the SuperCDMS collaboration.

Acknowledgements

First and foremost, I would like to thank my supervisor, David Cerdeño. David has been a constant source of guidance, wisdom, and encouragement, and I could not have asked for a better mentor. I would also like to thank Jeppe Andersen, who supervised me in the final months of my PhD. Over the course of my PhD I have had the privilege of working with many brilliant people. I extend my thanks to all of my collaborators, including Andrew Cheek, Dorian Praia do Amaral, Patrick Foldenauer, Holger Schulz, Pedro Machado, Andres Olivares del Campo, Marina Cermeño, and the SuperCDMS collaboration. I am also grateful to the STFC for providing the funding that allowed me to pursue my research, and to the Invisibles and MultiDark networks for supporting my travels to Fermilab and Spain, respectively.

I would not have been able complete this thesis without the support of countless wonderful colleagues at the IPPP. The spirit of community I found there was exceptional, and I would like to thank each and every person who helped to make me feel so welcome and accepted. To the residents of OC118, thank you for the advice, the friendship, and most of all the shenanigans. To Alex Lenz and the outreach team, thank you for giving me the opportunity to share the joy of physics with the world. To everyone who participated in Plot of the Month, journal club, the Soupdicate, El Club de Español, the inaugural squash ball foot golf world championships and so much more, you are all greatly appreciated. Special thanks must also go to everyone who helped with the proofreading of this work: Lucy, Jonny, Asli, Ryan, Jack, Joseph, Dorian, and Andrew.

The last 15 months have been challenging for all of us, and I have again benefited

from the support of many exceptional friends and loved ones who have my undying gratitude. To Andrea, thank you for everything you bring into my life. To Andrew and Parisa, without you this lockdown would have been unbearable. To Jamie, Jake, Will, Paul, Sophie, and Hazel, I love you all dearly. To my many friends of more than two legs: Balthie, Emmy, Bee, and others, thank you for filling my life with so much happiness.

Finally, I would like to thank my whole family, without whom I, and by extension this thesis, would not exist. This work is dedicated to all of you, but especially to you, Mum, for your endless patience, love, and kindness.

Thank you all.

Chapter 1

Introduction

The development of the Standard Model (SM) is rightly regarded as one of the great successes of modern particle physics. Over the past four decades, the predictions of the SM have consistently matched observations in high-energy physics experiments. However, despite these successes it is widely accepted that the SM provides an incomplete description of nature[2]. A vast quantity of evidence from cosmology and astrophysics indicates that the entire breadth of particles described in the SM accounts for only 15% of the total matter content of the Universe [8–10]. The remaining 85%, termed dark matter (DM), is a fundamental part of the standard Lambda cold dark matter (ΛCDM) model of cosmology [11]. DM plays a crucial role in our understanding of galaxy formation [12], and the presence of a large halo of relic DM in every galaxy is required to explain current observations [13]. Determining the nature of DM is one of the most pressing challenges facing particle physicists and cosmologists today, as it is inevitably linked to new physics beyond the SM.

The mystery of DM has motivated a huge array of novel experimental efforts to detect it [14–20]. In most cases, the design of these experiments has been tailored to search for a specific model of DM. However, the extreme sensitivity that is required to perform searches for the elusive DM may allow these experiments to study other

---

[2]Many excellent texts have been written on the subject of the SM (see e.g. Refs [5–7]). In the remainder of this work we will assume a basic level of understanding of its structure.

unexplored models of physics beyond the SM. As researchers, it is our responsibility to ensure that any experimental data that is gathered, often at great cost in both time and money, is utilised for the greatest possible benefit.

One SM particle which seems particularly well suited to study at DM experiments is the neutrino. Neutrinos are produced in copious quantities by many astrophysical phenomena, and their study, like that of DM, is one of the main efforts of astroparticle physics. The spectra of neutrinos in the universe today are believed to span at least 19 orders of magnitude in energy [21, 22], so they have the potential to generate signals in a wide range of DM experiments.

In this thesis, we will examine the prospects of studying neutrinos in one class of DM experiment: the direct detection (DD) experiment. As we will see, the energy window studied at these experiments makes them particularly sensitive to the interactions of solar neutrinos. While DD experiments are much smaller in scale than many dedicated neutrino experiments, they can nevertheless provide useful, complementary information in the search for additional physics beyond the SM which may affect neutrino scattering. We will focus in particular on simplified models which introduce new, light mediators, as they are well-suited to study at DD experiments.

In Chapter 2, we will discuss the motivation for and key principles of DM direct detection. We will introduce a simplified model of a DD experiment, as well as a few real-world experiments, which will serve as useful examples in the later parts of the thesis. We will also discuss my contribution to Ref. [1], in which we studied a generalised DM model in the context of DD experiments.

Chapter 3 takes the form of a brief history of neutrino physics in the 20th Century, with the aim of introducing concepts that will be of importance in the later chapters. These include the basic principles of neutrino detection, neutrino production in the Sun, neutrino oscillations both in vacuum and in matter, and finally a brief discussion of neutrino mass terms.

In Chapter 4 we will introduce the simplified models of new physics that we aim to

study using DD experiments. As was stated earlier, these have been chosen because their properties lend themselves to study at DD experiments. We will briefly review the existing constraints on the models, and the channels through which we expect them to produce signals in future DD experiments.

In Chapter 5, we will study the signals of new physics that would be produced in the simplified DD experiments we described in Chapter 2. The first part of this chapter is based on Ref. [2], in which we projected the effects of simplified models of new physics in the neutrino sector onto the canonical DM parameter space that is most commonly studied at DD experiments. This projection can serve as a useful tool, allowing us to infer the effects of new physics interacting in the neutrino sector on future searches for DM. We will also argue that it can be used to translate the reach of a DD experiment in the DM parameter space into an estimate of its sensitivity to new neutrino physics. In the second part of the chapter, we will discuss our ongoing efforts to recompute constraints from supernovae on some of the models from Chapter 4. Earlier works suggested that these were far more constraining that other limits from particle physics experiments, but they employed many approximations that warrant further examination.

Chapter 6 will focus on one DD experiment in particular: CDMSlite. Where before we had made many generalisations in order to obtain results that were applicable to a wide range of experiments, here we will consider the specific challenges that arise when computing constraints from neutrino scattering at a DD experiment. This chapter is based on ongoing work with the SuperCDMS collaboration, and several of the problems introduced here have not yet been resolved. However, an awareness of these problems and the accuracy of approximate methods will be important to the work of the following chapter.

Finally, in Chapter 7 we will study in detail the prospects of using future DD experiments to study of one of our simplified models: the $U(1)_{L_\mu - L_\tau}$. This model is of particular relevance as it can provide solutions to two unresolved mysteries in fundamental physics, the muon g-2 anomaly, and the H_0 tension. We will examine

whether future DD experiments will be able to test possible solutions to these problems, and compare their prospects with the reach of other upcoming particle physics experiments. This chapter is based on my contributions to Ref. [3].

Chapter 2

Direct detection of dark matter

The archetypal dark matter direct detection experiment of the past twenty years has its origins in a cosmic coincidence known as the WIMP miracle. As particle physicists sought to understand the nature of dark matter, they looked to cosmology to provide clues about its properties. The natural place to look was the early universe.

Almost all the matter present in the universe today was generated shortly after the Big Bang, through a series of processes which depended heavily on the various interactions between particles. At the end of the inflationary epoch the universe underwent reheating, as the potential energy of the inflaton was converted into the particle species we observe today. In these early moments, SM particles existed in thermal equilibrium with each other, their relative abundances determined by their masses, their scattering cross sections, and the Hubble expansion rate, H. As the universe expanded and cooled, the heavier of these particles began to drop out of thermal equilibrium, with particles and antiparticles annihilating into photons, or else decaying into lighter species. After the vast majority of antimatter had annihilated, however, a small but significant quantity of matter remained. This was due to an asymmetry in the abundances of matter and antimatter in the early universe, generated through a process known as baryogenesis, whose exact mechanism is still not known [23].

At some point during this period dark matter must have been generated, its relic

density settling near the value we measure today. The crucial question is therefore: can the requirement that dark matter is produced in the correct quantities in the early universe tell us anything about its fundamental properties?

Today, the landscape of potential dark matter candidates is vast, and many mechanisms for dark matter production have been suggested. One of the first and simplest mechanisms to be proposed was freeze-out [24]. Under this scenario, in the earliest moments after reheating, DM existed in thermal equilibrium with the surrounding medium. Its abundance, like those of the SM particles, evolved in a manner described by a Boltzmann equation [25],

$$\frac{\mathrm{d}n}{\mathrm{d}t} + 3Hn = -\langle \sigma v \rangle \left(n^2 - n_{eq}^2 \right) , \qquad (2.0.1)$$

with n the DM number density, n_{eq} the equilibrium density and $\langle \sigma v \rangle$ the thermally averaged annihilation cross section, assuming equal cross sections for annihilation and production [24]. Eventually, as the medium cooled, the DM decoupled at a time determined by it mass and scattering cross sections. As the DM candidate is assumed to be stable, the resulting yield[1] should give the same relic density measured today.

The WIMP miracle was the realisation that a weak-scale particle, i.e. one with both mass and coupling around the electroweak scale, could be generated through freeze-out with approximately the correct relic density to account for dark matter today. With a mass of more than a GeV, the particle, generically dubbed a weakly interacting massive particle or WIMP, would be an example of cold dark matter, and is therefore compatible with the ΛCDM model of cosmology [26]. Even more excitingly, a WIMP dark matter candidate was compatible with models of supersymmetry (SUSY) which seemed very well motivated in the 1990s and 2000s, where it was often identified with the lightest neutralino state [27].

Various arguments were used to place early bounds on the parameter space within

---

[1]The yield is the ratio of the number density and entropy density, $Y = n/s$. Is it useful as a measure of number density that does not change as the universe expands.

which a WIMP could lie. The so-called Lee-Weinberg limit places a lower bound on the mass of such a particle, $m_\chi \gtrsim 1.3$ GeV, (see e.g. [28]) while unitarity considerations place an upper bound of $m_\chi \lesssim 340$ TeV [29]. Solving Equation (2.0.1) to obtain the observed DM abundance yields a velocity-averaged annihilation cross section during freeze-out of $\langle \sigma v \rangle \approx 2.5 \times 10^{-26}$ cm^3/s for WIMPs within this mass range, close to the weak interaction strength at the electroweak scale. These bounds and expected values define a parameter space in which we expect a WIMP to exist, although all can be circumvented or are dependent on our choice of models of particle physics and cosmology [30, 31].

Although the WIMP cross section during freeze-out can be inferred from the measured yield, albeit with significant model dependencies, the process of translating this to a predicted signal in terrestrial particle physics experiments is non-trivial. Under certain well developed theories, such as the Minimal and Next-to-Minimal Supersymmetric Standard Models (MSSM and NMSSM), preferred values of the WIMP mass and couplings were derived, with those simplest SUSY scenarios favouring WIMP-nucleon scattering cross sections between 10^{-41} and 10^{-48} cm^2 [32]. However, as with the above values from cosmology, these predictions are highly sensitive to the choice of theory [33, 34].

Ultimately, if DM is assumed to be particle-like in nature, we are unlikely to determine its exact properties without detecting its signatures in particle physics experiments. While collider physicists considered the possibility of producing SUSY particles at the (then upcoming) LHC, others focused on detecting the dark matter particles that should already exist in our galaxy. A combination of observations and simulation indicate that the local DM density is approximately $\rho_0 \approx 0.4$ GeV cm^{-3} [35]. Assuming an approximately homogeneous local DM distribution there would be at least one 100 GeV WIMP per litre of space on Earth.

DD experiments aim to detect the signals of particles in the DM halo scattering with atomic matter on Earth. For more than two decades, ever larger and more sensitive DD experiments have been developed to explore greater regions of the

canonical WIMP parameter space, with no signal of dark matter ever being confirmed in multiple experiments. In the remainder of this work, we will discuss the new challenges that face experimental efforts to probe yet smaller WIMP couplings, the novel methods that are being applied to face these challenges, and ultimately, how these incredibly sensitive machines can be used to place constraints on other areas of new physics, most notably in the neutrino sector. First, though, we will review the simplified, canonical WIMP model, and the characteristic signal that DD experiments hope to observe.

2.1   WIMP signals in direct detection experiments

The landscape of DD experiments is almost as diverse as the array of DM candidates they search for. Since their inception, these experiments have utilised a wide array of technologies and identifiers to try to distinguish a potential DM signal from the many competing backgrounds. A few of these we will discuss further when we introduce some of the past and future DD experiments in Section 2.2. However, just as we will use a simplified model for our canonical WIMP candidate, we will also consider a simplified, idealised DD experiment. This will hopefully be useful as a pedagogical tool, and it can also be helpful when making predictions about potential future experiments, whose exact detector properties are not yet fixed.

The simplified DD experiment searches for signals of WIMPs scattering with atomic nuclei. These it detects from the recoils of nuclei within the detector mass, and it bins the detected events based on their energy. Naturally, other particles may also scatter within the detector, forming a background to the search. It is crucial that these backgrounds are minimised and that those that remain are well under-stood, so that an analysis can subtract them from the spectrum and determine whether any additional signal events have been detected. For the moment we will

ignore backgrounds, as they are specific to individual DD experiments, and focus on predicting the WIMP signal. WIMPs may also scatter with atomic electrons within the detector, however these events are usually more difficult to distinguish from backgrounds, for reasons we will discuss more in Section 2.2. In our simplified experiment we will ignore electron scattering events.

The expected differential rate, often expressed in units of $\text{kg}^{-1} \text{ day}^{-1} \text{ keV}^{-1}$, from the non-relativistic elastic scattering of a DM particle, χ, with mass m_χ off a target nucleus with mass m_A in our experiment is

$$\frac{dR}{dE_R} = \frac{\rho_0}{m_A \, m_\chi} \varepsilon(E_R) \int_{E_R'} dE_R' \, \text{Gauss}(E_R', E_R) \int_{v_{min}} d\vec{v} \, v f(\vec{v}) \frac{d\sigma_{\chi A}}{dE_R'} \,, \qquad (2.1.1)$$

where ρ_0 is the local DM density and $f(\vec{v})$ is the DM velocity distribution, which we will discuss in more detail shortly. $\varepsilon(E_R)$ is the energy dependent efficiency, and for most DD experiments is approximately flat within the main sensitivity range. In our simplified experiment we replace it with a Heaviside function $\Theta(E_R - E_T)$, where E_T is the threshold energy below which the experiment cannot detect the recoil. A Gaussian smearing function is usually employed to simulate the energy resolution of the detector, but in our simplified DD experiment we will assume perfect energy determination, so $\text{Gauss}(E_R', E_R) = \delta(E_R' - E_R)$.

The particle physics of DM-nucleus scattering is encoded in the differential cross section, $d\sigma_{\chi A}/dE_R$. More general cross sections will be considered in Section 2.3, but for now we will use the simplest, canonical WIMP model. In this model, the DM couples to nucleons through a spin-independent (SI) operator, with equal couplings to protons and neutrons. In order to make comparisons between detectors employing different target nuclei, the differential WIMP-nucleus cross section can be related to the SI WIMP-nucleon cross section, $\sigma_{\chi N}^{(SI)}$, by [36, 37]

$$\frac{d\sigma_{\chi A}}{dE_R} = \frac{m_A \sigma_{\chi N}^{(SI)}}{2\mu_{\chi N}^2 v^2} \left| \mathcal{F}_{SI}(E_R) \right|^2 \,, \qquad (2.1.2)$$

where $\mu_{\chi N}$ is the WIMP-nucleon reduced mass, and $\mathcal{F}_{\mathcal{SI}}(\mathcal{E}_\mathcal{R})$ describes the nuclear response. If the momentum transferred in the scattering event is not much larger

than the radius of the target nucleus (a few keV for most nuclei [38]) the WIMP will scatter coherently, without probing the inner structure of the nucleus. For larger momentum transfers than this, $F_{SI}(E_R)$ replicates the resulting decrease in the cross section due to the gradual loss of coherence. In our SI scattering model, the nuclear response function can be decomposed into

$$|\mathcal{F}_{SI}(E_R)|^2 = A^2 \, |F_{SI}(E_R)|^2 , \qquad (2.1.3)$$

with A the number of nucleons in the target nucleus. $F_{SI}(E_R)$ is the nuclear form factor, and encodes the complex, target-specific effects of scattering within the many-body system of the nucleus at finite momentum transfer. It is normalised so that $F_{SI}(0) = 1$, and at higher momentum transfer we approximate it using a Helm form factor [39].

The expected number of events found in each energy bin, k, is then calculated by integrating the differential scattering rate,

$$N_k = \epsilon \int_{E_k}^{E_{k+1}} dE_R \, \frac{dR}{dE_R}, \qquad (2.1.4)$$

where the exposure, $\epsilon = M^{\text{fid}} t$, is the product of the fiducial detector mass and run-time of the experiment. Only three parameters are therefore required to specify a given DD experiment under our model: the exposure, ϵ; the energy threshold, E_T; and the target isotope, while the WIMP parameter space we are exploring is reduced to just two parameters: the mass, m_χ, and SI WIMP-nucleon cross section, $\sigma_{\chi N}^{SI}$. Lighter WIMPs will transfer less momentum during a collision, and so m_χ can be reconstructed from the spectral shape observed in a detector [40]. This also means that the energy threshold of a DD experiment will limit the minimum WIMP mass to which it will be sensitive. Examples of some spectra predicted for WIMPs of different masses are shown in Figure 2.1.

The final piece of information needed to calculate the expected signal in our experiment is the WIMP velocity distribution. In order to calculate the scattering rate at a given recoil energy, we integrate over this distribution, with a lower limit on the

integral given by the smallest DM velocity that can lead to a recoil of energy E_R,

$$v_{\min} = \sqrt{m_A E_R/(2\mu_{\chi A}^2)} \tag{2.1.5}$$

with $\mu_{\chi A}$ the DM-nucleus reduced mass. Although we will ultimately be using a highly simplified model for the WIMP velocity distribution in most of this work, I will give a brief overview of the many uncertainties and complexities associated with this key ingredient of all DD analyses.

2.1.1 The WIMP velocity distribution

Determining the density and velocity distribution of particles in the DM halo is extremely challenging. Galaxy rotation curves are most useful in the outer regions of the halo, where dark matter outweighs luminous matter by several orders of magnitude. Even assuming a roughly homogeneous local distribution[1], estimates for the local DM density can vary between $0.2 - 0.5$ GeV cm^{-3} [35, 41]. However, this uncertainty is not too much of an obstacle to our current searches, as any future revision to the accepted value would simply shift all previous constraints on the cross section by a scale factor. Unless stated otherwise, in this work we will take $\rho_0 = 0.4$ GeV cm^{-3}, in line with most modern DD analyses. We should, however, be careful when taking constraints from earlier works, where they may have used a value for the density that is now outdated.

The significant uncertainties associated with the velocity distribution are more challenging to deal with. A revised estimate of the average velocity would result in a change in the shape of the energy spectrum. This would lead to different effects on the constraints obtained from different experiments, as they are sensitive to different ranges of recoil energies. One property we do expect the DM velocity distribution to have is that there should be no WIMPs with speeds higher than the Galactic escape

---

[1]If the DM halo exhibited significant substructure on length scales similar to the size of the solar system, or smaller, the Earth could conceivably be in a region with very little DM present. However, standard WIMPs are not expected to behave this way, so we will not consider this possibility here.

velocity, in the Galactic rest frame. This places an upper limit on the recoil energies we are likely to observe of a few hundred keV.

The simplest commonly used model for the velocity distribution is the standard halo model, or SHM. In this model, the velocities of dark matter particles follow a spherically symmetrical Maxwell-Boltzmann distribution around the centre of the Galaxy, with the average velocity determined by the Jeans equation, and a cutoff at the Galactic escape velocity. This has a few problems [42]. Firstly, simulations of Galactic halo formation don't typically lead to perfectly Gaussian velocity distributions. Secondly, we cannot be certain that the velocity distribution will be spherically symmetric. Proposals have long existed for a "dark disk", a sub-population of dark matter that co-rotates with the Galactic disk [43], and as we learn more about Galactic dynamics it seems more and more likely that additional sub-components exist. Data from the Gaia space telescope has revealed a population of stars moving with a velocity distribution separate to the bulk of the Milky Way [44]. This component has been dubbed the Gaia Sausage, due to its shape in velocity space, and believed to be the result of a collision between the Milky Way and a dwarf galaxy (sometimes called Gaia-Enceladus-Sausage) around 10 billion years ago. The DM that was once present in that dwarf galaxy is expected to follow a similar velocity distribution, leading to an additional "sausage component" to the DM velocity distribution. The exact size of this component in local space is unknown, leading to a further uncertainty [45].

In spite of these shortcomings, the SHM is still widely used in DD analyses. It has been shown that while hydrodynamic simulations can produce velocity distributions that differ from the SHM, the resulting event rates expected at DD experiments do not differ greatly [46]. The SHM therefore remains a useful tool for producing results that are comparable to as many previous results as possible. For the remainder of this work, we will take our velocity distribution from the SHM, in other words, a Maxwellian distribution with a cutoff at the Galactic escape velocity. After being shifted to the lab reference frame, the resulting velocity distribution at a time t

is [47, 48]

$$f(\vec{v}_T, t) = N \left(\frac{3}{2\pi v_{rms}^2} \right)^{3/2} \exp\left(-\frac{3|\vec{v}_T + \vec{v}_E(t)|^2}{2v_{rms}^2} \right) \Theta\left(u_{esc} - |\vec{v}_T + \vec{v}_E(t)| \right), \quad (2.1.6)$$

with $\vec{v}_T$ the WIMP velocity in the lab frame, $\vec{v}_E$ the Earth's velocity in the Galactic rest frame, and $u_{esc} \approx 544$ km s^{-1} the Galactic escape velocity. N is a factor to ensure the correct normalisation, so the integral over the whole velocity distribution is 1. The root-mean-square velocity in the SHM is $v_{rms} = \sqrt{3/2}v_0$, with $v_0 \approx 220$ km s^{-1} the local Galactic rotation velocity.

The velocity of Earth in the Galactic frame, $\vec{v}_E$, varies with a period of 1 year as the Earth revolves around the Sun. This should lead to an annual modulation in the scattering rate of dark matter on Earth. Several DD experiments preserve timing information for the scattering events they record, hoping to use this annual modulation signal to distinguish a dark matter signal from backgrounds. One of the most prominent of these experiments is DAMA/LIBRA, a sodium-iodide based detector that for the past 20 years has been reporting an annually modulating signal whose phase is consistent with a DM origin [49]. The result is puzzling, as the region of WIMP parameter space that could produce such a signal has long been excluded by other DD experiments, and no known model of DM can consistently explain the apparently contradictory results. Two new NaI based detectors, COSINE-100 and ANAIS, are currently operating with very similar experimental conditions to DAMA/LIBRA. Recent results from ANAIS are in strong tension with the DAMA/LIBRA result, further disfavouring a DM explanation for the signal [50].

While annual modulation data may one day play an important role in confirming the source of a measured DM signal, most simple DM analyses do not use timing data, and so are insensitive to the time dependence of $\vec{v}_E$. We therefore replace it in Equation (2.1.6) with its time-averaged value, which is equal to the velocity of the Sun: $\langle v_E \rangle = v_\odot$. This is not exactly the same as v_0, as the Sun has some peculiar motion relative to the rotation of the Galaxy. Including this effect we find $v_\odot = 232$ km s^{-1}.

The direction of $\vec{v}_\odot$ is not important for our simplified DD experiment, as like most current detectors it does not gather directional data and we assume that its sensitivity is independent of the recoil direction. However, directional information has been considered as another way of distinguishing a potential DM signal from backgrounds. The direction of $\vec{v}_\odot$ points roughly in the direction of the constellation Cygnus, so it is from this direction that the WIMPs with the highest velocity are expected to appear, under the assumption of the SHM. Experiments such as DRIFT have never placed the most stringent limits on DM models, but they been responsible for important advances in directional detection technology. Many of these efforts have now joined together under the CYGNUS collaboration [51], with the aim of using directional detection technology to explore regions of the DM parameter space where conventional DD experiments would be limited by backgrounds.

2.2   Past and future direct detection experiments

The simplified models we have constructed both for the properties of DM and the structure of a DD experiment will both be useful when performing general comparisons with the overall landscape of DD constraints, particularly in Chapter 5. For analyses of individual experiments, however, we can greatly improve the accuracy of our results by considering additional detector-specific properties, including efficiency curves, detector resolution, and backgrounds. In this section, I will review some of the recent and upcoming DD experiments that are most relevant to the work of this thesis, but first I will give an overview of how backgrounds are typically handled in DD experiments.

Current constraints on the WIMP parameter space show that, if they exist, WIMPs must have very small couplings to atomic matter, much smaller than those of most SM particles. As a result, backgrounds from SM scattering processes must be tightly controlled to avoid overwhelming any potential DM signature. DD experiments are typically housed in deep underground laboratories with a large rock overburden to

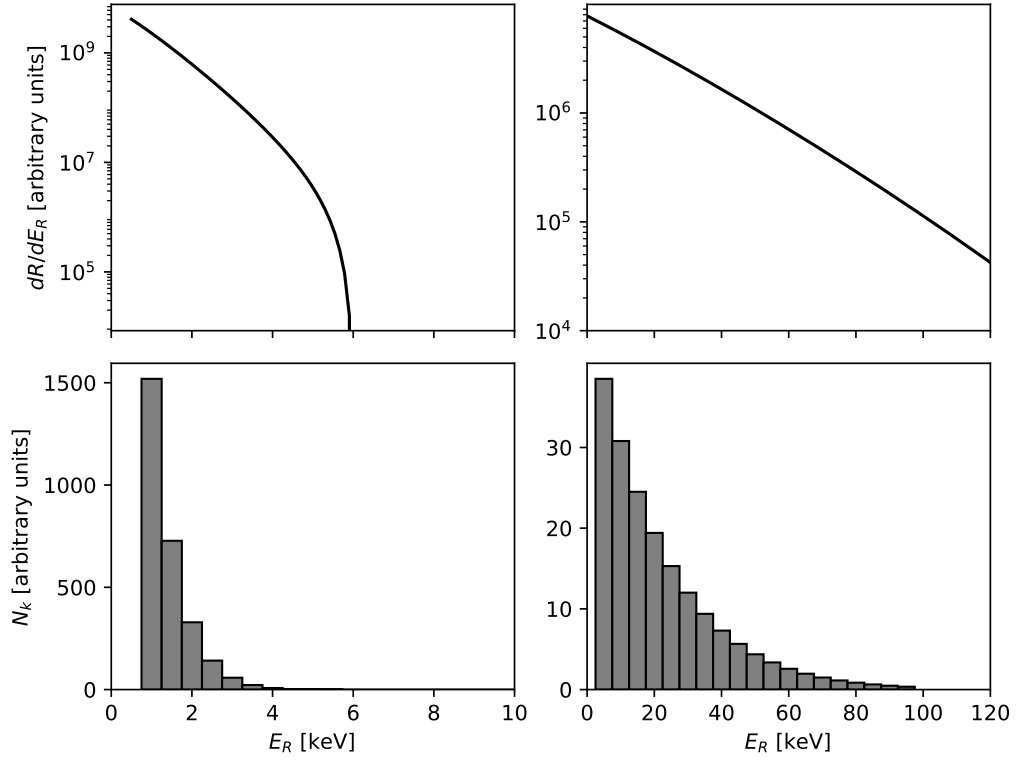Figure 2.1: Examples of differential scattering rates (*top*) and binned energy spectra (*bottom*) produced in our simplified DD experiment by a canonical WIMP scattering with germanium nuclei through a spin-independent coupling, under the simplifying assumptions discussed in this section.
Left: Spectrum for a WIMP with mass $m_\chi = 6$ GeV.
Right: Spectrum for a WIMP with mass $m_\chi = 100$ GeV.

provide shielding from high-energy cosmic rays. These labs are usually located in regions with low background radiation, and the experiments themselves are generally surrounded by multiple layers of radiation-shielding material. Many modern detectors are constructed in advanced cleanrooms with filtration systems to reduce the level of radon gas in the air [52] and ensure the radiopurity of detector components. In spite of these measures, significant numbers of background scattering events are typically expected to occur within any DM detector. Statistical methods are employed to further reduce the level of background in a DD analysis: cuts are made within the parameter space of scattering events to remove regions where more background events occur. To make these cuts, additional information must be gathered about each scattering event. This often includes spatial information, with events close to the surface of the detector volume typically being rejected, as this is where a majority of backgrounds from less-penetrating radiation occur.

The majority of the remaining background events are typically due to particles scattering with atomic electrons. Since we expect to see more signal events from WIMPs scattering with nuclei, we can greatly reduce the background by discriminating between electron- and nuclear-scattering events. To do this, many experiments employ a two-channel detection system. Recoils within the detector are measured via two complementary signals, for example scintillation and ionisation [53, 54], ionisation and phonon excitation [55], or scintillation and phonon excitation [56]. Electron and nuclear scattering events will have different profiles when viewed through both detection channels, allowing some amount of discrimination and rejection of electron scattering events.

- **SuperCDMS and CDMSlite**

  The SuperCDMS collaboration has a long history of setting competitive bounds on WIMP-nucleus interactions using semiconductor detectors operating at millikelvin temperatures. Employing a combination of germanium and silicon semiconductor crystals, the previous iteration of the experiment, SuperCDMS

Soudan, set the most stringent limits on WIMP scattering with germanium nuclei for masses > 12 GeV with a 1690 kg day exposure [57]. In its standard, high-threshold mode, the experiment utilised both phonon and charge detectors to provide the two signals required for excellent rejection of electron scattering events.

Some of the SuperCDMS Soudan detectors were also operated in a low threshold mode called CDMSlite, in which a high voltage was applied to allow detection of sub-keV recoils, at the expense of any ability to distinguish nuclear from electron recoils. Although the total fiducial exposure of CDMSlite was < 80 kg days, the lower threshold allowed it to set constraints on WIMPs with masses as low as ~ 1.5 GeV. However, with no target discrimination there were larger backgrounds than in the high-threshold analysis [58], further limiting the sensitivity to DM candidates with very small couplings to atomic matter.

The next iteration of the SuperCDMS experiment will be SuperCDMS SNO-LAB [55]. Located in an even deeper underground lab, with a larger exposure, lower backgrounds and thresholds, and dedicated detectors designed to operate in the high voltage mode used for CDMSlite, its projected sensitivity covers large portions of as-yet unprobed parameter space. We will later use Super-CDMS SNOLAB as the benchmark for the next generation (G2) of germanium detectors.

- **Xenon1T and LZ**

  One of the most prevalent technologies in DD is the liquid Xenon (LXe) time projection chamber (TPC). The dual signals required for target discrimination are provided by a prompt burst of photons from LXe scintillation, and ionisation electrons which induce a secondary, delayed scintillation signal after drifting to the top of the detector due to an applied voltage. The position of the initial scattering event can be determined by the location at which the secondary signal is detected and the time delay between the two signals. This

allows fiducialisation of the detector volume.

LXe TPCs are well suited to being scaled up, as with large volumes the detector mass is self-shielding: the outer regions of dense LXe shield the inner fiducial volume from backgrounds. The largest such detector to release results to-date is Xenon1T, the first DD experiment to achieve a fiducial exposure of 1 ton yr [59]. In addition to its standard nuclear scattering analysis, Xenon1T recently released an analysis of its electron scattering events, showing an apparent excess in low-energy events [60]. We will discuss this result further in Chapter 7.

The next major iteration of the LXe TPC detector will be LZ. Currently installed at the Sanford Underground Research Facility (SURF), LZ is expected to achieve an exposure of 15 ton yr over its initial 1000 live-day exposure [61]. We will use this as our benchmark for a G2 xenon TPC detector.

- **DARWIN**

  The DARWIN experiment has been proposed as a successor to G2 LXe experiments [62]. Considered a next-to-next generation (G3) experiment, DARWIN would utilise a 200 ton year exposure to provide a 10-fold improvement in sensitivity over previous LXe TPCs. Although the project is still in the early planning stages, we will use it as a guide to the possible future of large liquid xenon detectors in the latter part of this decade.

- **DarkSide-20k**

  The DarkSide collaboration aims to detect DM interactions within a liquid argon (LAr) TPC. The scale of LXe experiments will soon be limited by the annual global production of xenon, but as argon is vastly more abundant, an LAr TPC could make the dream of a kiloton-scale DD experiment a reality [63]. The detection method is similar to that of the LXe experiments, with the two signals required for electron recoil rejection provided by prompt scintillation and delayed ionisation emissions. LAr allows for superior discrimination of

nuclear vs electron recoils compared with LXe, and the upcoming DarkSide-20k detector aims to achieve extremely low rates of background. However, this level of background rejection can only be achieved at recoil energies $\gtrsim 30$ keV, so the the detector will have a relatively high energy threshold.

DarkSide-20k aims to achieve a fiducial mass of 20 tons [64]. As the detector is not yet installed and running, we will consider DarkSide-20k as a G3 argon-based dark matter detector.

2.3 An effective theory for dark matter interactions

The simplified SI model of WIMP-nucleus scattering is the most commonly used in DD analyses. Sometimes a second, spin-dependent (SD) component is considered [65]. However, the general effective Lagrangian describing DM interactions with nuclei in the non-relativistic limit can be much more diverse [66], featuring up to 18 different operators, some of which display a non-trivial dependence on the DM velocity and momentum exchange [66–68]. The resulting effective field theory (EFT) is then described in terms of a Lagrangian that contains four-field operators of elastic scattering between a dark matter particle and a target nucleon,

$$\mathcal{L}_{\text{int}} = \sum_{\tau} \sum_{i} c_i^{\tau} \mathcal{O}_i \overline{\chi} \chi \overline{\tau} \tau. \tag{2.3.1}$$

In this expression, τ can denote either proton and neutron interactions, or isoscalar and isovector interactions. In this work we will use the isospin basis, so $\tau \in \{0, 1\}$, with $c_i^0 = c_i^p + c_i^n$ the isoscalar couplings and $c_i^1 = c_i^p - c_i^n$ the isovector couplings. In a non-relativistic EFT, the number of effective operators is limited by the requirement that they must be invariant under Galilean transformations, and so the momentum- and velocity-dependent terms can only depend on the momentum transfer and the relative incoming velocities. Still, at least 14 non-relativistic operators can appear in

tree level when describing a WIMP-nucleus interaction mediated by a particle with spin ≤ 1 [67]. The total DM-nucleus cross section can be calculated by summing coherently over the contributions from different operators, giving

$$\frac{d\sigma_{\chi T}}{dE_R} = \frac{m_A}{2\pi m_v^4}\frac{1}{v}\sum_{ij}\sum_{\tau,\tau'=0,1} c_i^\tau c_j^{\tau'} \mathcal{F}_{i,j}^{\tau,\tau'}(v^2,q^2) \, , \qquad (2.3.2)$$

where $m_v = 264$ GeV is the Higgs vacuum expectation value, and $\mathcal{F}_{i,j}^{\tau,\tau'}(v^2,q^2)$ are nuclear response functions whose expressions can be found in, e.g., Refs [67,69]. Non-zero interference terms will occur between certain pairs of EFT operators, and between the two isospin components within each operator. When proton and neutron couplings differ, destructive interference can cause a suppression in the cross section with particular target isotopes.

In the event that a positive DM signature were detected, the spectral shape could in principle be used to reconstruct the contributions from the various effective operators [70]. This reconstruction is limited by several factors, including statistics [71], the various astrophysical uncertainties discussed in Section 2.1.1 [72], and uncertainties on the nuclear response functions [73]. Additionally, in the up-to-15 dimensional parameter space we are probing, many degeneracies are likely to exist between different combinations of operators. It has been shown that multiple results from different experimental targets will be important for disentangling these degeneracies and correctly identifying the DM parameters [74–77]. The inclusion of data from indirect searches and colliders such as the LHC can also provide valuable complementary information with which the DM properties can be better determined (see e.g., Refs. [78–86]).

Another challenge that presents itself when exploring a multidimensional parameter space is the computation time required. To constrain the WIMP parameter space we construct a binned likelihood function,

$$\mathcal{L}(\Theta) = \prod_a \mathcal{L}^a(\Theta) = \prod_a \prod_k \frac{N_k^a(\Theta)^{N_k^{a,\text{obs}}} e^{N_k^a(\Theta)}}{N_k^{a,\text{obs}}!} \qquad (2.3.3)$$

where the observed number of recoil events, $N_k^{a,\text{obs}}$, in energy bin k of experiment a is compared with the prediction of the model for the point in parameter space $\boldsymbol{\Theta}$. Here we have assumed that the spectrum observed in each experiment follows an independent Poissonian distribution, so the overall likelihood function is given by the product of the likelihoods for each experiment, $\mathcal{L}^a$.

Traditionally, the likelihood evaluator would be connected to a code that computes the full expected DM spectrum for a given point in parameter space using Equation (2.1.4). As this computation requires three nested integrals, sampling over many dimensions can be extremely expensive.

To speed up the process, in Ref. [1] I contributed to the development of RAPIDD, a surrogate model that allows a fast and accurate determination of the expected DM spectrum in direct detection experiments, with D. Cerdeño, A. Cheek, and H. Schulz.

2.4 Surrogate models for direct dark matter detection

Surrogate models are a tool for approximating the behaviour of a variable, when an analytical model is either not known or is prohibitively expensive to compute, by fitting an approximate model to the available data. In our case, we have used the PROFESSOR tool [87] to parametrise the experimental response of DD experiments in terms of polynomial functions. The Python code has been released publicly as RAPIDD (Reconstruction Algorithm of Parameters In Direct Detection) [1].

In order to be useful as a tool for constraining the multidimensional parameter space in the event of a future DM detection, RAPIDD must be able to precisely and accurately reproduce the DM energy spectrum for a given point in parameter space, $\boldsymbol{\Theta}$, while providing a significant reduction in computing time. To test its effectiveness, we used MultiNest [88,89], a Bayesian inference tool, to reconstruct DM parameters

from a (simulated) DM signature detected in multiple DD experiments. We compared the results obtained when using RAPIDD with those utilising the full physics code to provide $N_k^a(\mathbf{\Theta})$ for the likelihood calculation.

Surrogate models have previously been utilised to bypass computationally expensive calculations in other areas of high-energy physics. Similar approaches to ours have been successfully applied in collider physics to optimise choices of parameters for Monte-Carlo event generators [90], and to constrain effective operators in searches for BSM physics [91, 92].

Surrogate models can take almost any form, however in general they should be able to be evaluated quickly while accurately reproducing the form of the model they are replacing. In our case, we chose to use polynomials, as they are quick to evaluate and relatively cheap to train. Initially we believed that they would provide a good fit to the binned DM event rate, as we expected the rate to vary smoothly as a function of the DM parameters. However, we found that in a few scenarios this assumption was false, and the initial polynomial fits struggled to replicate certain behaviours of the DM scattering rate, namely negative interference effects between different operators and effects from the escape velocity cut-off in the velocity distribution.

My own contribution to the work focused mainly on testing the goodness-of-fit around these regions. I will discuss this in more detail shortly, but first I will give a more detailed description of the procedure used by RAPIDD.

RAPIDD aims to produce a combination of polynomials in the DM parameters, $\mathcal{P}_k^a(\mathbf{\Theta})$, that reproduces the number of signal events found in each energy bin of a given experiment, $N_k^a(\mathbf{\Theta})$. Before attempting a fit, we must decide on an appropriate order $\mathcal{O}$ for our polynomials. The optimal choice of $\mathcal{O}$ depends on the particular physics model, as we found that some models of DM interaction required higher order polynomials than others to achieve the same level of precision. Once the order has been fixed, we determine the N_{coeffs} coefficients, $d_{k,l}^a$, such that

$$N_k^a(\mathbf{\Theta}) \approx \mathcal{P}_k^a(\mathbf{\Theta}) = \sum_{l=1}^{N_{\text{coeffs}}} d_{k,l}^a \, \tilde{\Theta}_l \equiv \mathbf{d_k^a} \cdot \tilde{\mathbf{\Theta}} \,, \tag{2.4.1}$$

where $\tilde{\Theta}_l$ are all the suitable combinations of the parameters, $\boldsymbol{\Theta}$, up to order $\mathcal{O}$. For example, for a second order polynomial in a 2D parameter space $\boldsymbol{\Theta} = (m_\chi, c_1) = (x, y)$, these would take on the form $\mathbf{d_k^a} = (\alpha, \beta_x, \beta_y, \gamma_{xx}, \gamma_{xy}, \gamma_{yy})$, and $\tilde{\boldsymbol{\Theta}} = (1, x, y, x^2, xy, y^2)..$

To determine the coefficients, we must compute a sample of at least N_{coeffs} energy spectra using our full physics code. The coefficients for the polynomial representing bin k of experiment a can then be determined by solving the matrix equation

$$\vec{N}_k^a = M_{\tilde{\boldsymbol{\Theta}}} \cdot \mathbf{d_k^a}, \qquad (2.4.2)$$

where $\vec{N}_k^a$ is a vector of computed event numbers, and the rows of matrix $M_{\tilde{\boldsymbol{\Theta}}}$ are the corresponding values of $\tilde{\boldsymbol{\Theta}}$ for each sampled point. PROFESSOR solves this equation by using singular value decomposition to determine the pseudo-inverse of the matrix $M_{\tilde{\boldsymbol{\Theta}}}$.

The minimum number of sample points, N_{coeffs}, for a polynomial of given order and dimension is given in Ref. [87]. We found it useful to oversample by at least a factor of two, to provide validation of the parametrisation.

Computing these sample points using the full physics code was often the most time-consuming part of our calculation. However, the number of spectra required to train the polynomials is vastly smaller than the number required by MultiNest to constrain a parameter space to a reasonable degree of precision. After the initial training phase we interface RAPIDD with MultiNest, choosing a number of livepoints and a tolerance to determine the precision of our fits. A comparison of the runtime required when interfacing MultiNest with RAPIDD, and with the full physics code, is shown in Figure 2.2. In this example case, with only a small number of parameters, we observe a consistent speed improvement of approximately two orders of magnitude.

My main contribution to the project was in testing the goodness-of-fit of the surrogate models. To do this, we generated spectra using the full physics code and compared with the corresponding predictions from RAPIDD. We identified a few behaviours
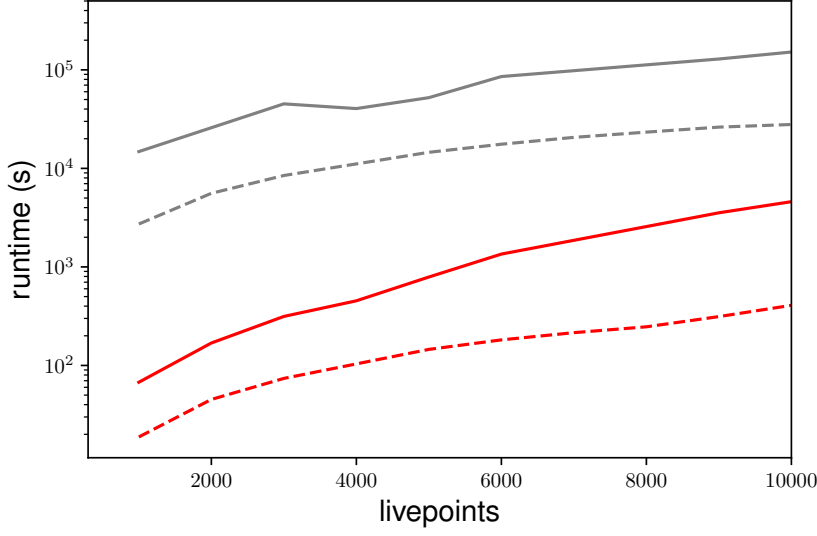
Figure 2.2: Execution time of the surrogate model RAPIDD (red
lines) and full physics code (grey lines) as a function of
the number livepoints used in MultiNest runs. The solid
(dashed) lines correspond to the case with (without)
astrophysical uncertainties. Taken from Ref. [1].

that our surrogate model struggled to reproduce, and adjusted our methods to ensure

a high level of precision across the whole parameter space.

- **Cancellations between effective operators**

  Interference terms exist between several combinations of operators in our ef-

  fective theory. These interference terms can in principle be negative, leading

  to cancellations between operators for specific combinations of couplings, c_i.

  Initially, our plan was to produce a single polynomial for each energy bin,

  with terms for every combination of couplings up to order $\mathcal{O}$. However, we

  found that this method produced a poor fit in regions of the parameter space

  where cancellations occurred. From Equation (2.3.2) we know that the overall

  cross section can be constructed as the coherent sum of the contributions from

  different operators. Since individual components of the cross section are ex-

  pected to vary more smoothly, we can better capture the subtleties of operator

  cancellation by producing a separate polynomial for the contribution of each

  effective operator (and for each non-zero interference term) and summing over

them, so

$$N_k^a(\boldsymbol{\Theta}) \approx \sum_{ij} \sum_{\tau,\tau'=0,1} \mathcal{P}_k^{a,i,j,\tau,\tau'}(\boldsymbol{\Theta})\,. \tag{2.4.3}$$

This formulation also reduces the training time required, as it requires a smaller set of sample points, and solving Equation (2.4.2) for multiple smaller matrices is much faster than inverting a single, much larger matrix.

- **Low-mass DM**

  The DM energy spectrum in general varies smoothly with the mass of the DM candidate. However, in our formulation of the velocity distribution in Equation (2.1.6) we included a Heaviside function at the Galactic escape velocity, u_{esc}. For a particle with velocity v in the lab reference frame, there will be a maximum to the energy which can be transferred during a scattering event,

  $$E_R^{max} = 2\frac{\mu_{\chi A}^2}{m_A}v^2\,. \tag{2.4.4}$$

  For a given mass, there will therefore be a maximum to the recoil energy that can be induced in a DD experiment. For sufficiently high-mass WIMPs, this maximum will be beyond the sensitivity range of DD experiments. For lighter WIMPs, however, there will exist some bins that are energetically inaccessible, and will thus have a count rate of zero. We found that our polynomials struggled to capture the behaviour of the event rate within in bins as m_χ crossed this threshold, leading to a poor reconstruction for low DM masses. To improve the fit, we explicitly incorporated a Heaviside function in our surrogate model to satisfy the condition in Equation (2.4.4). The improvement can be seen in Figure 2.3, where we plot the root-mean-squared (RMS) deviation across all bins between spectra generated using RAPIDD, and those simulated with the full physics code, before and after factoring out the Heaviside function.
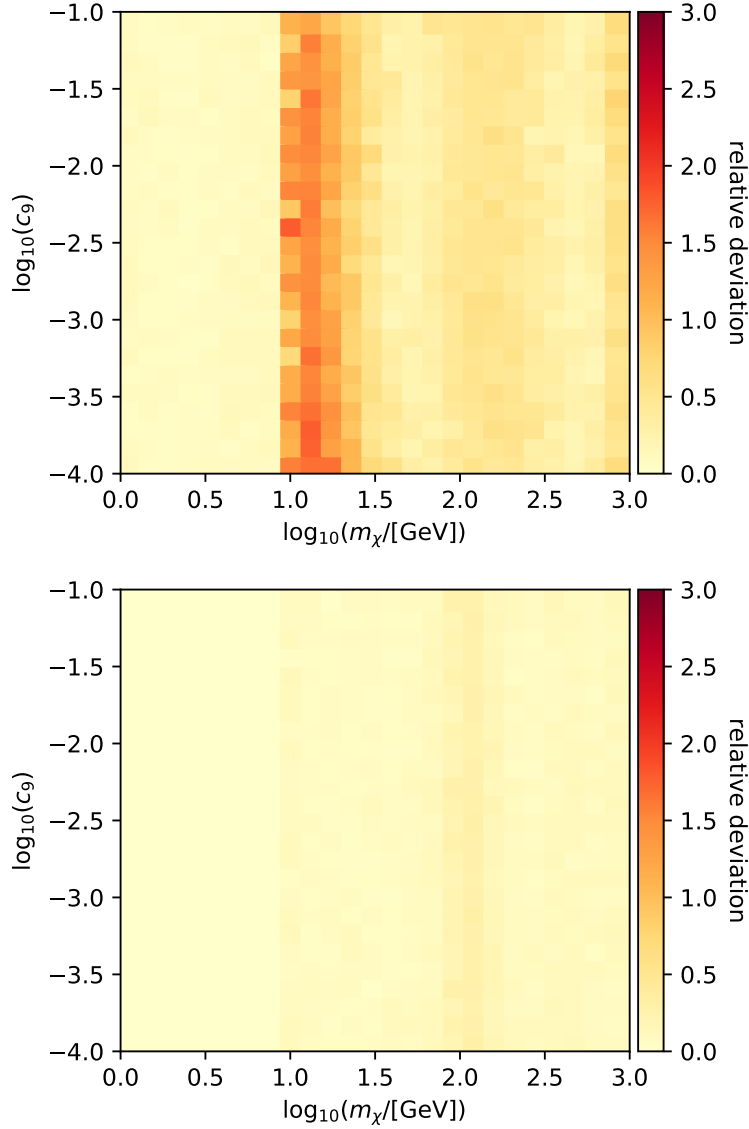
Figure 2.3: RMS deviation, across all energy bins, of the spectra generated by RAPIDD from those generated using the full physics code. *Top:* In which we naïvely attempt to fit the event rate in each bin with a single $\mathcal{O}(3)$ polynomial. For $m_\chi \lesssim 10$ GeV, no events are expected in any of the energy bins of this experiment. *Bottom:* In which we have explicitly included the Heaviside function in the DM mass as a factor in our polynomial, easing the tension in the fit around $m_\chi \sim 10 - 30$ GeV. An artefact is still visible around $m_\chi \approx 100$ GeV, which can be eased by using a higher-order polynomial.

- **Order of the polynomials**

  In the lower plot of Figure 2.3, an artefact is visible around $m_\chi = 100$ GeV. This type of precision loss is a common sign that the polynomial being used is not of a high enough order to correctly capture the behaviour of $N_k^a(\boldsymbol{\Theta})$. Since higher order polynomials take longer to train and evaluate, we wish to use the lowest order that provides the desired level of precision across the whole parameter space. In all our example cases in Ref. [1] we were able to reproduce the DM energy spectrum with agreement within 1%. In most cases this required $\mathcal{O}(4)$ polynomials, though in one of our examples a fifth-order polynomial was required.

  We also found that our models lost precision near the boundaries of the parameter space on which they were trained. This was likely due to random nature of our sampling of the space, where the very edges our nominal interpolation regions could in fact require our models to extrapolate beyond their training data. The issue is trivially solved by ensuring that the region sampled for training data is larger than the region in which the surrogate model is subsequently used.

With these changes implemented, we found that RAPIDD was able to provide an good fit to the DM scattering rate for all the models that were tested, with deviations of less than 1% provided the correct order of polynomials was selected. We also demonstrated that RAPIDD could indeed be interfaced with MultiNest to accurately reconstruct the DM parameters from a given set of experimental signatures, and even showed that the parameter space could be expanded to incorporate generalised models for the DM halo.

Further discussion of RAPIDD and non-relativistic EFTs in the context of simplified models of DM scattering can be found in Ref. [1]. However, we have now discussed my main areas of contribution to the project, and as these additional examples and validation procedures are not relevant to the rest of this thesis, we will not discuss

them here. Instead, we will now turn our attention away from DM itself, and begin to consider other potential areas of new physics that may soon be accessible to DD experiments. The first step towards this task will be to properly introduce the particle that will be central to the rest of this work: the neutrino.

Chapter 3

A brief history of neutrino physics

The history of the study of neutrinos is one of the great successes of modern particle physics. Neutrinos are by their very nature difficult to observe, and any experiment hoping to study them must overcome many challenges similar to those discussed in Chapter 2. Despite this, over the past 90 years we have taken the neutrino from its initial place as a near-complete mystery, to a well defined ingredient of the Standard Model, and then to one of our clearest signs of the need for physics beyond the Standard Model. In this chapter, we will briefly review the history of neutrino physics, beginning with early efforts to detect them experimentally. Refs. [93, 94] were extremely useful when researching this topic. We will end with a discussion of one of the most interesting phenomena associate with neutrinos: their oscillations, and the resulting requirement that neutrinos have mass.

This review cannot claim to limit itself to Standard Model physics, since the observed properties of neutrinos require the inclusion of some physics beyond the SM. However, where possible we will be focusing on only the most minimal extensions required to account for current observations. In Chapter 4 we will introduce the specific models of new physics that will be important for the remainder of this thesis.
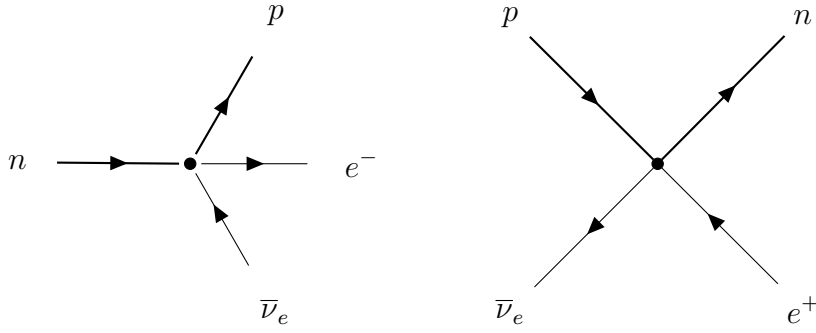
Figure 3.1: *Left:* Feynman diagram for the beta decay of a neutron
in Fermi's theory, producing a proton, electron, and
antineutrino. *Right:* Equivalent Feynman diagram for
inverse beta decay, where a proton and antineutrino
scatter to produce a neutron and a positron.

3.1   Detecting neutrinos

The existence of neutrinos was first postulated by Pauli in 1930, to explain the con-
tinuous energy distribution of electrons emitted via beta decay [95]. Pauli suggested
that the "wrong" statistics observed in beta decay spectra could be explained by the
existence of a new, light particle with zero charge, which would be emitted along with
the electron and carry a portion of the momentum away undetected. The particle,
which we now know as the (anti)neutrino, formed an integral part of Fermi's theory
of beta decay, but it was initially believed that the particle would be impossible to
directly detect. Fermi's theory suggested one channel for detection: if neutrinos were
emitted through beta decay, they could interact with protons to induce inverse beta
decay, as shown in Figure 3.1. At first it was thought that the tiny cross section of
the process ($\sigma \leq 10^{-44}$) was too small to be measured experimentally [96], but in
1946, Pontecorvo calculated that a ton-scale detector placed within a few metres of
a typical nuclear reactor should produce a few scattering events per day [97].

In 1956, Cowan and Reines put Pontecorvo's idea into practice. Utilising a target
mass of 200 kg of water, they aimed to detect the signal of inverse beta decay
induced by neutrinos from the Savannah River Plant nuclear reactor [98]. To obtain
a distinctive signal that could be distinguished from backgrounds, the experiment

was designed to detect both the positron and neutron produced during the scattering. This was possible in the case of neutrinos scattering with hydrogen nuclei within the water molecules. After scattering, the emitted positron would quickly annihilate with an atomic electron, producing two gamma photons. The neutron, having no other nucleons to bind to, would travel through the detector volume as a free neutron. The water was doped with cadmium, an efficient absorber of free neutrons which releases a characteristic de-excitation gamma photon shortly after a neutron is captured. The three photons, two emitted promptly and one with a small delay, were detected by the "detector tanks" filled with liquid scintillator which surrounded the water tanks, with the resulting photon burst measured using photomultiplier tubes (PMTs).

The experiment achieved its aim and produced the first confirmed detection of neutrino scattering [99]. Aside from the obvious significance of a first detection, the experiment confirmed several hypotheses regarding the nature of neutrinos. Firstly, the inferred scattering cross section was in good agreement with that predicted by Fermi theory. Secondly, the observed reaction, along with previous negative results in searches for what we would now call lepton-number-violating (LNV) processes, confirmed that the particles being emitted during nuclear fission were in fact antineutrinos, and that they were in some way distinct from their antiparticles, neutrinos. The design of the Cowan-Reines experiment also remains relevant as it informed the designs of many subsequent neutrino detectors.

The next major leap in understanding came with the discovery of neutrino flavour. By the late 1950s, it was understood that neutrinos were also being emitted during the decay of pions to muons,

$$\pi^- \rightarrow \mu^- + \overline{\nu}. \tag{3.1.1}$$

Searches for the hypothetical decay $\mu^- \rightarrow e^- \gamma$ had already provided some indication that the neutrinos associated with electronic and muonic processes were distinct [100, 101]. To test this hypothesis, a new experiment was constructed at the Brookhaven National Laboratory which featured the world's first accelerated neutrino beam [102]. The neutrinos would be produced by pions decaying according to Equation (3.1.1).

If approximately equal numbers of muons and electrons were produced within the detector, this would indicate that a single type of neutrino was involved in both pion decay and inverse beta decay. In fact, significantly more muon events were observed, giving definitive evidence that different flavours of neutrino were associated with the two types of process: ν_e and ν_μ.

We will not spend time discussing the particular methods of detecting and distinguishing high-energy muons from electrons here. However, the method by which the neutrino beam was generated is still being used today, so we will briefly review it [103]. The first step towards producing a muon neutrino beam is to accelerate protons to high energy, usually $E \gtrsim 10$ GeV. At Brookhaven, this was achieved using the then 15 GeV Brookhaven Alternating Gradient Synchrotron (AGS) particle accelerator [102]. These protons are collided with a solid target, usually beryllium or graphite, to produce pions. The charged pions can be focused using magnetic fields, before decaying through various channels including the one in Equation (3.1.1). A thick shield of steel, concrete, or aluminium absorbs all the other decay products, leaving only the beam of high-energy neutrinos to propagate to the detector beyond. While most of the beam will consist of ν_μ or $\overline{\nu}_\mu$, some of the muons produced will decay to generate a small population of electron neutrinos and antineutrinos. The ability to generate a beam of high-energy neutrinos, mostly in the the ν_μ flavour eigenstate, is essential to modern neutrino physics.

These early experiments focused on detecting neutrinos from man-made sources: either nuclear reactors or particle accelerators. A very large flux of neutrinos could be obtained by placing the detectors quite close to the neutrino source, and the analyses could benefit from the ability to turn the sources on and off, which aided greatly in background discrimination. However, by this time it was understood that large fluxes of neutrinos should also be produced during nuclear fusion processes in the Sun, and in the late 1960s Davis and Bahcall led the development of the Homestake neutrino detector to search for them. The experiment would search for

evidence of neutrino capture by chlorine,

$$^{37}\text{Cl} + \nu_e \rightarrow \,^{37}\text{Ar} + e^- \,. \tag{3.1.2}$$

This reaction has a threshold energy of $E_\nu = 0.814$ MeV [104], but a "superallowed" transition to the ^{37}Ar ground state can occur with a neutrino energy of 5.15 MeV, leading to a large enhancement of the cross section [105]. The detector contained large quantities of pure ^{37}Cl, with any ^{37}Ar produced being collected and measured. The experiment would therefore be sensitive to the flux of neutrinos with energies above the threshold, with greatest sensitivity to neutrinos with $E_\nu \approx 5.15$ MeV [106].

3.1.1 Neutrinos from the Sun

Most of the Sun's energy is produced through a fusion process called the proton-proton (pp) chain. The pp chain consists of a web of nuclear reactions with different branching ratios that ultimately fuse ionised hydrogen (protons) into helium-4, as can be seen in Figure 3.2. The 26.7 MeV binding energy of ^{4}He is mostly released in photons, but in five of the processes within the pp chain neutrinos are produced, carrying away a small fraction of the released energy. We denote the resulting five populations of neutrinos according to the processes that generate them: pp, pep, hep, ^{7}Be, and ^{8}B.

Although the pp chain accounts for $> 98\%$ of the energy produced in the Sun [107], there is another process by which stars can fuse hydrogen into helium: the carbon-nitrogen-oxygen (CNO) cycle. In this process, shown in Figure 3.3, the fusion of hydrogen into helium is catalysed by the presence of heavier elements: carbon, nitrogen, and oxygen. A second branch of the CNO cycle, CNO-II, occurs with a small branching ratio of around 0.04%. In fact additional branches exist: CNO-III and CNO-IV, but their branching ratios are temperature dependant and they do not occur at significant rates in the Sun [109]. Neutrinos are produced during three reactions within the first two CNO cycles: the ^{13}N, ^{15}O, and ^{17}F neutrinos.
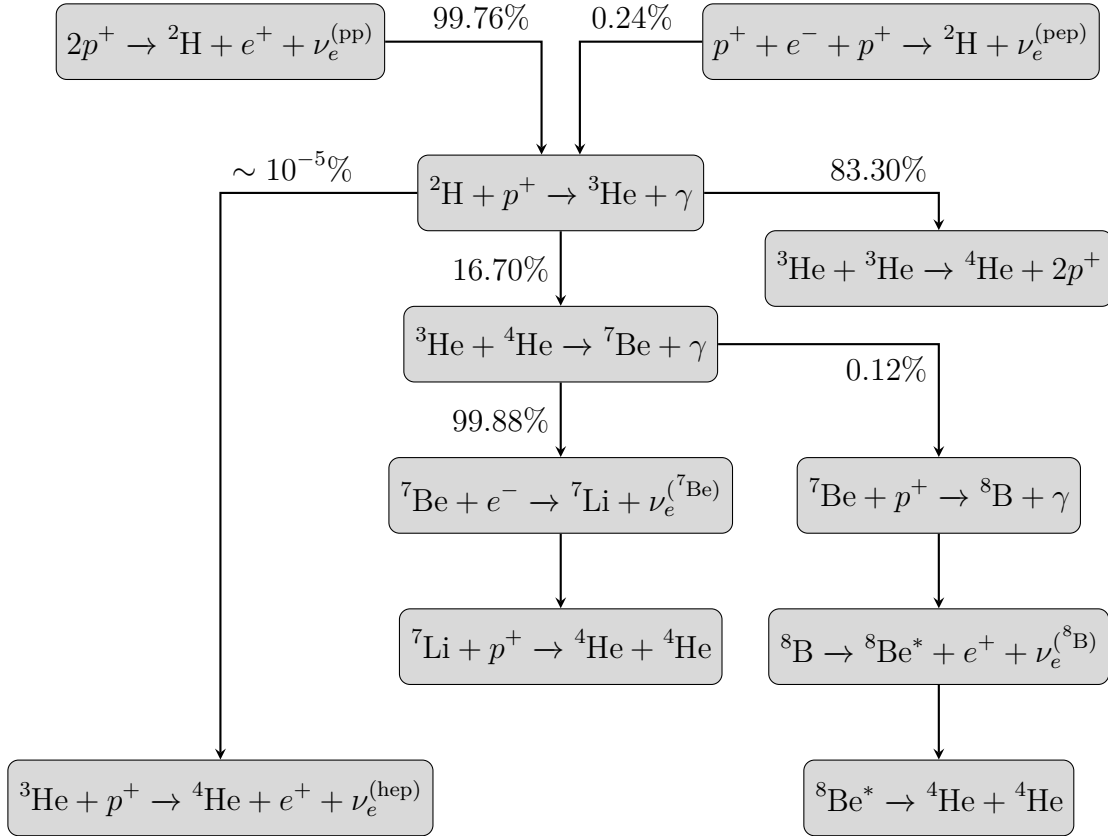
Figure 3.2: The various processes which make up the proton-proton (pp) chain of fusion in the Sun [107]. Neutrinos are produced during five of these reactions, leading to five neutrino flux populations each with their own energy distribution: pp, pep, hep, ^{7}Be and ^{8}B neutrinos.
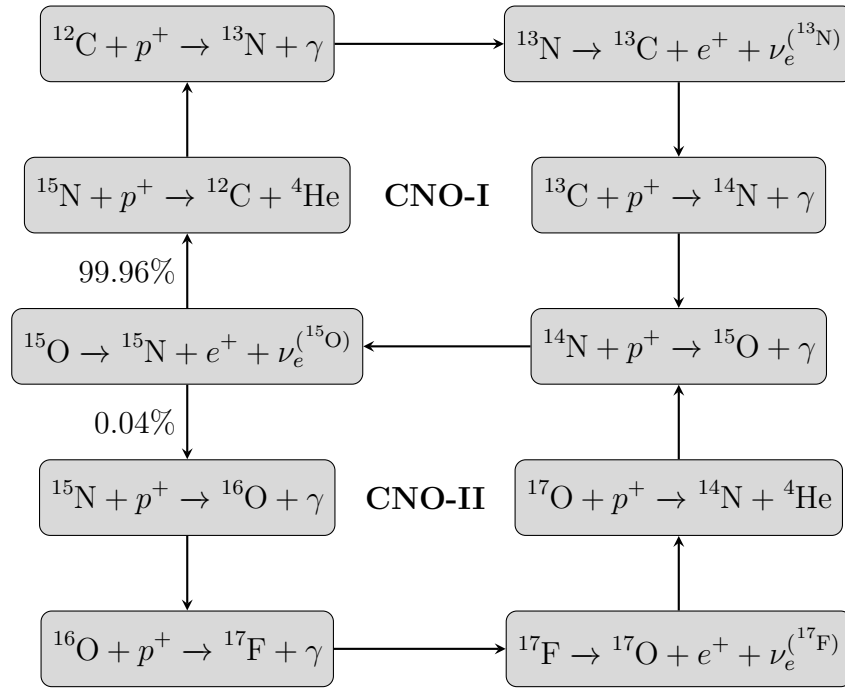
Figure 3.3: The CNO cycle is another stellar fusion process [108]. In the Sun it is subdominant compared with the pp-chain, but in hotter stars it is the main source of energy [107]. In these hotter stars a larger proportion of reactions follow the CNO-II branch, and some extend to further branches: CNO-III and CNO-IV, though these do not occur at a significant rate in the Sun, and so only the first two branches are shown here.

The rate of CNO-cycle fusion is highly dependent on temperature, with the rate of energy production $\epsilon_{\mathrm{CNO}} \propto T^{18}$, compared with $\epsilon_{pp} \propto T^4$ for the pp chain [107]. While the CNO cycle is the dominant source of energy in much larger and hotter main-sequence stars, in the Sun it is subdominant to the pp chain, and so the flux of solar "CNO" neutrinos is smaller than that produced in the main branch of the pp chain.

The exact rate of solar CNO reactions is unknown, as it depends on the abundance of catalyst elements: carbon, nitrogen, and oxygen, in the Sun. These quantities are currently unknown, with a longstanding disagreement between values that agree with helioseismology [110] and those found using modern hydrodynamical modelling of the Sun's photosphere [111]. In astrophysics, any element heavier than helium is generically referred to as a metal, so the discrepancy is known as the solar metallicity problem [112–114]. A precise measurement of the CNO neutrino fluxes would indicate the rate of these reactions, and help to solve the solar metallicity problem. However, for reasons we will discuss more in Chapter 7, such a measurement has proven challenging.

The flux spectra of the various solar neutrino populations are shown in Figure 3.4. The most abundant neutrinos are produced with energies below 1 MeV, but ^{8}B neutrinos can reach energies greater than 10 MeV. ^{8}B neutrinos can therefore benefit from the 5.15 MeV superallowed ^{37}Cl transition, and it was this neutrino flux to which the Homestake experiment was most sensitive.

The Homestake experiment published its first results in 1968 [106]. It had successfully made the first measurement of the solar neutrino capture rate, with an average of 3×10^{-36} events per atom per second. However, this value was lower than the prediction made by Bahcall et al. in the same year, of $7.5 \pm 3.3 \times 10^{-36}$ events per atom per second [116]. The initial discrepancy could have been explained by a statistical fluctuation, but as Homestake continued to gather data and Bahcall continued to refine his prediction, a clear deviation emerged [117]. The disagreement became known as the "solar neutrino problem", and it would take over three decades
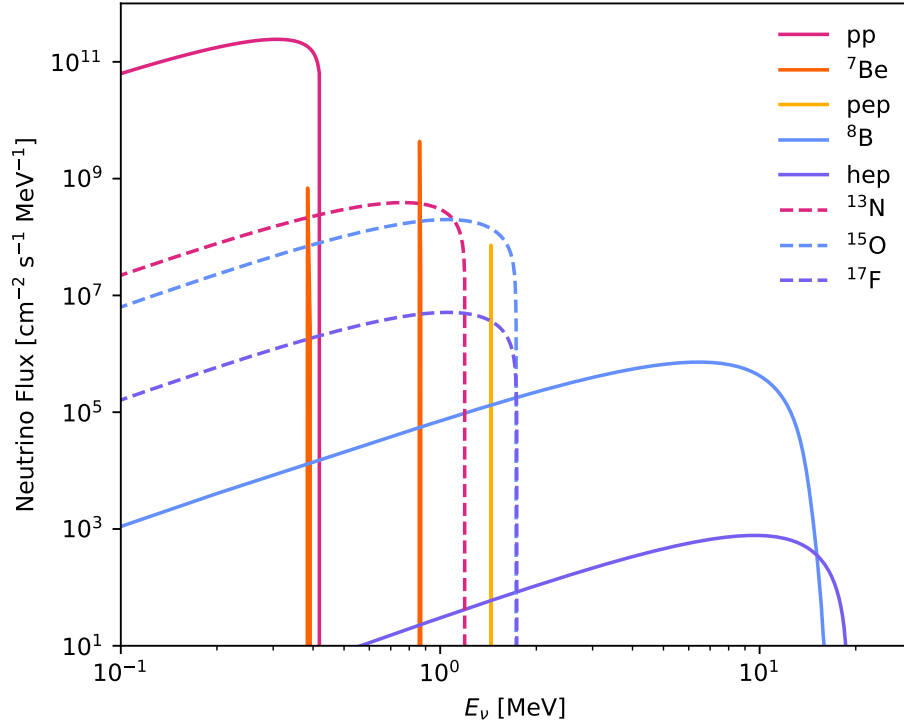
Figure 3.4: Flux spectra of the various populations of solar neutrinos [115]. Neutrinos produced in the pp chain are plotted as solid lines; those produced in the CNO cycle are dashed.

to resolve.

Bahcall's prediction of the solar ^{8}B neutrino scattering rate rested on two major pieces of theory: the Standard Model of particle physics, and the Standard Solar Model (SSM). The disagreement with Homestake's observed results indicated a problem with at least one of these models.

Many early attempts to resolve the solar neutrino problem focused on modifying the SSM. A key motivation for measuring the solar neutrino flux had been to validate our models of solar fusion, and the deficit detected by Homestake could be explained by relatively straightforward adjustments to solar parameters. The ^{8}B flux is the most dependant on the Sun's core temperature of all the pp-chain neutrinos [118], so a cooler solar core could seemingly resolve the issue. However, in the 1980s new experiments began to probe solar neutrino interactions through different detection

channels, and their results further deepened the mystery of the solar neutrino flux. In Japan, the Kamioka Nuclear Decay Experiment was repurposed into Kamiokande-II, a water Cherenkov detector which allowed real-time detection of neutrino-electron scattering events [119], as opposed to the month-on-month isotope measurements of Homestake. In the USSR, the Soviet-American gallium experiment (SAGE) made the first measurement of low energy pp neutrinos, by studying inverse beta decay in ^{71}Ga [120], and two years later another gallium-based detector, GALLEX, began taking data in Gran Sasso [121]. The additional data from these experiments ruled out many of the simple explanations involving modifications to the SSM [122]. Furthermore, by this time new helioseismology measurements had been shown to give good agreement with Bahcall's predictions [123], lending support to the validity of the SSM.

Incidentally, the influx of new experiments studying solar neutrinos provided a new avenue for studying other astrophysical phenomena. In 1987, a supernova, dubbed SN 1987A, was detected around 50 kiloparsecs from Earth in the Large Magellanic Cloud. A few hours earlier, a burst of neutrino events had been detected at three particle physics experiments around the world: Kamiokande-II [124], the Irvine-Michigan-Brookhaven detector (IMB) [125], and the Baksan Underground Scintillation Telescope (BUST) [126]. This was the first time that the hypothesised supernova neutrino burst had been detected. Measurements of the flux, energy, and duration of the 1987 burst are still some of the best information we have about the nature of supernova neutrino emission, and we will discuss this event in greater detail in Section 5.3.

Modifications to the SSM were increasingly disfavoured by experiments, but perhaps the solution could lie in particle physics. All the experiments which had measured solar neutrinos had been sensitive to electron neutrinos: the state in which all solar neutrinos are produced. Physicists over the previous few decades had been developing the theory of a phenomenon that went beyond the nascent Standard Model of particle physics, and could potentially explain the deficit in the observed

ν_e flux: neutrino oscillations.

3.2 Neutrino Oscillations

As mentioned above, solar neutrinos are generated in interactions involving electrons, and so they are produced in the electron neutrino state: a so-called flavour eigenstate corresponding to the mass eigenstate of the charged electron. If, however, neutrinos had non-zero masses, they would have their own mass eigenstates, which need not align with the flavour eigenstates. The flavour eigenstates, ν_α, would instead be superpositions of the mass eigenstates, ν_i, so that

$$\nu_\alpha = \sum_i U_{\alpha i} \nu_i, \tag{3.2.1}$$

with U a unitary mixing matrix analogous to the CKM matrix in the quark sector. What follows will be a brief review of the resulting phenomenology of neutrino oscillations. Many more complete reviews exist. Of particular help when preparing this thesis were Refs. [127–129].

In principle, neutrino oscillations could occur with any number of neutrino species, however, we will take as an initial example the case with only two, as it is both the simplest case and the one which was most studied in the early days of the solar neutrino problem. Later, we will introduce the third generation of neutrinos. We will also briefly introduce the different methods of neutrino mass generation, but we will not delve too deeply into this, as it is not the subject of this thesis. We will instead focus on the phenomenological results of the theory, as these are more relevant to this work.

The simplest type of neutrino oscillations, from a phenomenological standpoint, are vacuum oscillations. Neutrinos are produced via particle interactions in a flavour eigenstate, a particular coherent superposition of the mass eigenstates. In the two-neutrino paradigm $\alpha \in \{e, \mu\}$ and $i \in \{1, 2\}$, and a single parameter, or mixing angle, θ, describes the transformation between the flavour and mass eigenstates. Ignoring

complex phases, the mixing matrix in Equation (3.2.1) is given by

$$U = \begin{pmatrix} \cos\theta & -\sin\theta \\ \sin\theta & \cos\theta \end{pmatrix}, \tag{3.2.2}$$

in the neutrino mass basis.

As they propagate, however, the ν_1 and ν_2 components acquire a relative phase due to their different masses, so that after propagating a certain distance the mixture of mass eigenstates will not necessarily be the same as the initial neutrino state. Rather than being a perfect flavour eigenstate, the neutrino will now be a mixture of ν_e and ν_μ, with the probability of measuring it in one or the other osciallating over a length scale governed by the mass separation between the $\nu_{1,2}$ eigenstates. The probability of finding a neutrino generated in state ν_α in the state ν_β after propagating a distance L is given by

$$P(\nu_\alpha \to \nu_\beta) = \left| \sum_i U_{\alpha i} U_{\beta i}^* e^{-i\frac{\Delta m_{i1}^2}{2E}L} \right|^2, \tag{3.2.3}$$

where E is the neutrino energy and $\Delta m_{i1}^2 = m_i^2 - m_1^2$ (a nice derivation can be found in Ref. [130]).

The idea of neutrino oscillations was first hinted at by Pontecorvo in 1957, when he drew parallels with the mixing of K_0 and $\tilde{K}_0$ mesons [131, 132]. In 1967 he provided a more detailed description of neutrino oscillations, and even suggested that they could affect astronomical neutrino observations [133]. The concept of neutrino mass mixing was first discussed by Maki, Nakagawa, and Sakata in their 1962 work [134], though at the time they did not discuss the resulting oscillation phenomenology.

By the end of the 1970s, Bilenky and Pontecorvo had determined the conditions under which vacuum neutrino oscillations could provide the solution to the solar neutrino problem [135]. Specifically, they determined that the mixing must be large, with a mixing angle close to $\pi/4$ (the angle under which mixing is maximal), and the oscillation length must be smaller than the distance from the Sun to the Earth (1 AU).

The length scale over which the transition probability oscillates is determined by the mass splitting (in the two-neutrino paradigm, Δm_{21}^2) and the neutrino energy,

$$l_v = \frac{4\pi E}{\Delta m_{21}^2}. \tag{3.2.4}$$

In order for oscillations to occur between the Sun and the Earth, Bilenky and Pontecorvo determined that $\Delta m_{21}^2 \gtrsim 10^{-11}\,\text{eV}^2$ [135]. If the mass splitting is much larger than this, ^{8}B neutrinos will undergo many oscillations during their journey to Earth, and the Homestake experiment would be sensitive to the electron-neutrino survival probability averaged across a full oscillation,

$$P(\nu_e \to \nu_e) = 1 - \frac{1}{2}\sin^2 2\theta. \tag{3.2.5}$$

In the case of near-maximal mixing, this would result in a $\sim 50\%$ reduction in the observed neutrino flux, easing the tension between theory and experiment considerably.

However, just as the new experimental results of the late 1980s disfavoured solar physics solutions to the problem, they also seemed incompatible with vacuum neutrino oscillations. Additional data from the Homestake experiment indicated that the observed scattering rate was less than 50% of the SSM prediction [136], while the results from Kamiokande-II and the low-energy gallium experiments were consistent with suppression around 50%. This was difficult, though not impossible, to reconcile with a vacuum oscillation solution. The "just-so" solution suggested that for a specific range of Δm_{21}^2 between 5 and $13 \times 10^{-11}\,\text{eV}^2$, the position of Earth relative to the Sun would be such that the ^{8}B neutrinos to which Homestake was sensitive would lie near an oscillation maximum [137]. The probability of measuring them in the ν_e eigenstate could then be less than a half, while the other experiments, being sensitive to lower energy neutrinos, would see the oscillation average, 50%. Clearly, however, this model requires significant fine-tuning, and by this point an alternative mechanism had been proposed: the Mikheyev-Smirnov-Wolfenstein (MSW) effect.
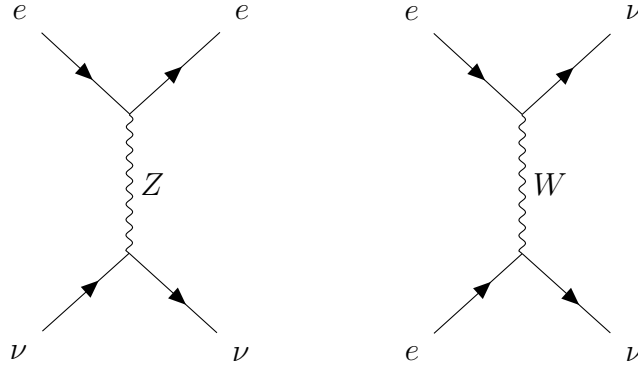
Figure 3.5: *Left:* Feynman diagram for the neutral-current (NC) scattering of a neutrino with an electron via exchange of a Z boson. *Right:* Equivalent Feynman diagram for the charged-current (CC) scattering of a neutrino with an electron via exchange of a W boson. This process only occurs for electron neutrinos.

3.2.1   The MSW effect

We have seen how neutrino oscillations can occur in vacuum as a result of differences in the time dependence of the complex phases in neutrino eigenstates of different masses. In a 1978 paper, Wolfenstein pointed out that neutrinos would also acquire a complex phase as they propagated through a medium, due to forward scattering with the medium particles [138]. Flavour-neutral interactions would only contribute an overall phase to a neutrino state, leading to no observable effects. However, a non-flavour-neutral coupling, for example the charged-current interaction between the ν_e state and atomic electrons shown in fig. 3.5, would induce an additional relative phase between different flavour eigenstates.

As a neutrino propagates through a medium, it acquires a matter-induced complex phase given by

$$\phi_m = V_\alpha t \,, \tag{3.2.6}$$

where V_α is the matter-induced potential experienced by a neutrino flavour eigenstate ν_α. The CC interaction leads to a relative phase between electron-neutrinos and

other flavour eigenstates of

$$\Delta\phi_m = (V_e - V_a)t\,. \tag{3.2.7}$$

In the SM, the difference in the potentials experienced by ν_e and any other flavour state, ν_a, is the charged-current potential, $V_{CC} = \sqrt{2}G_F N_e$, where G_F is the Fermi coupling constant and N_e is the local density of electrons. This matter-induced phase oscillates over a length scale l_0, where in the SM

$$l_0 = \frac{2\pi}{V_e - V_a} = \frac{\sqrt{2}\pi}{G_F N_e}. \tag{3.2.8}$$

This length scale is called the "refraction length", as the matter potential can be equivalently considered in terms of an index of refraction.

The presence of this potential modifies the Hamiltonian of the system, so that $H = H_0 + V$, with H_0 the Hamiltonian in vacuum. The eigenstates of this Hamiltonian are not the same as the neutrino mass eigenstates in vacuum, ν_i, but are effective mass eigenstates, ν_{im}. These effective mass eigenstates can be related to the flavour eigenstates in the same way as the vacuum case, but with different mixing angles. Continuing with our example of two-neutrino mixing, the mixing matrix has the same form as the one in Equation (3.2.2), but with a new mixing angle, θ_m. The mixing angle in matter is related to the vacuum mixing angle and the ratio between the vacuum oscillation length, l_v, and the refraction length, l_0, by

$$\tan 2\theta_m = \tan 2\theta \left(1 - \frac{l_v}{l_0}\sec 2\theta\right)^{-1}, \tag{3.2.9}$$

with the oscillation length in matter given by

$$l_m = l_v \left[1 + \left(\frac{l_v}{l_0}\right)^2 - 2\cos 2\theta \left(\frac{l_v}{l_0}\right)\right]^{-1/2}. \tag{3.2.10}$$

Wolfenstein [138] identified three regions of interest for the ratio l_v/l_0:

- $l_v \ll l_0$: The effects of the matter potential on neutrino oscillations are small. The effective mass eigenstates are close to the neutrino mass eigenstates in-
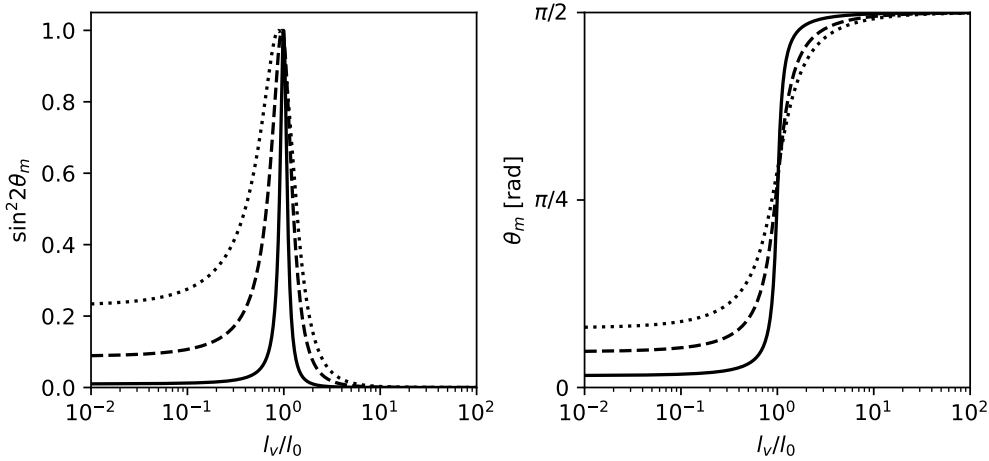
Figure 3.6: *Left*: The MSW resonance in $\sin^2 2\theta_m$, as a function of l_v/l_0 for three small values of the vacuum mixing angle: $\theta = 0.05$ (solid line), $\theta = 0.15$ (dashed), and $\theta = 0.25$ (dotted). *Right*: The dependence of the matter mixing angle, θ_m, on l_v/l_0 for the same values of θ.

vacuum, and the mixing is similar to the vacuum case ($\theta_m \approx \theta$, $l_m \approx l_v$).

- $l_v \gg l_0$: Matter effects dominate. The effective mass eigenstates are close to the flavour eigenstates, so mixing is minimal ($\sin 2\theta_m \approx 0$).

- $l_v \approx l_0$: In the intermediate case, Wolfenstein showed that θ_m could be significantly different from the vacuum mixing angle. Indeed, Equation (3.2.9) implies the presence of a resonance in $\tan 2\theta_m$ when $l_v = l_0 \cos 2\theta$, with oscillation length $l_m = l_v/|\sin 2\theta|$. However, it was not until 1985 that Mikheyev and Smirnov performed a more comprehensive study of the physical effects of this resonance on neutrino oscillations [139]. Their work would provide a final answer to the solar neutrino problem, and the resonance is now commonly known as the Mikheyev-Smirnov-Wolfenstein resonance.

Mikheyev and Smirnov were interested in the resonant behaviour of the mixing angle when $l_v \approx l_0 \cos 2\theta$. Plotting $\sin^2 2\theta_m$ as a function of l_v/l_0 for various small values of the vacuum mixing angle, as in Figure 3.6, they found that the behaviour was indeed consistent with a physical resonance [140]. Next, they considered the effect of

a neutrino propagating through a medium of smoothly decreasing density, as is the case (at least approximately) for neutrinos produced in the Sun. For neutrinos of sufficient energy ($E_\nu \gtrsim 3$ MeV), the conditions within the solar core satisfy $l_v > l_0$. As they exit the Sun, the neutrinos must pass through a layer of material in which the resonance condition is met, before reaching the lower density region where vacuum mixing is restored.

What are the effects of crossing the resonance? The answer depends on the thickness of the resonant layer, R_{res}. If the density varies slowly enough, so that $R_{\text{res}} > l_m$, the neutrino undergoes deep oscillations and propagates adiabatically through the resonance, with no conversion between the ν_{1m} and ν_{2m} effective mass eigenstates. The survival probability will only depend on the mixing parameters at the endpoints of the neutrino's path. It may seem that this scenario would lead to a higher ν_e survival probability for neutrinos crossing the resonance, since there is very little mixing in the high-density limit. However, while the effective mass eigenstates do align closely with the flavour eigenstates in the high density limit, there is a significant phase difference between the values of θ_m on either side of the resonance when θ is small, as can be seen in the right-hand plot of Figure 3.6. When $l_v \gg l_0$, $\nu_e \approx \nu_{2m}$, and after propagating adiabatically out of the solar core, these neutrinos emerge in an almost pure ν_2 state. When they arrive on Earth, the average survival probability is not that found in Equation (3.2.5), but rather

$$P(\nu_e \rightarrow \nu_e) = \sin^2 \theta. \tag{3.2.11}$$

This dramatic conversion between neutrino flavour eigenstates due to adiabatic propagation across the MSW resonance is known as the MSW effect. It provided an explanation for the various experimental measurements of solar neutrino fluxes. For low energy pp-neutrinos, the conditions in the solar core are such that $l_v < l_0$, and their oscillations are not greatly affected by matter effects. The ^{8}B neutrinos detected by Homestake, however, are produced in mostly the ν_{2m} eigenstate. They experience the MSW effect, and the resulting survival probability is given by Equation (3.2.11).

For neutrinos with much higher energies, the condition $R_{\mathrm{res}} > l_m$ would not be satisfied for the Sun's density profile, and the MSW effect would not be observed. The neutrinos would not cross the resonance adiabatically, and transitions $\nu_{1m} \leftrightarrow \nu_{2m}$ would occur. In reality, however, neutrinos of these energies are not produced in the Sun.

Although the MSW effect provided a solution to the solar neutrino problem, further evidence would be required to confirm the presence of neutrino oscillations. In 1998 the successor to Kamiokande-II, Super-Kamiokande, measured the solar neutrino flux at unprecedented precision and performed the first measurement of the spectral shape of the flux above 5 MeV [141]. It also employed a directional detection technique, demonstrating that the observed neutrino flux indeed originated from the direction of the Sun.

Then, in 2002, the SNO experiment provided a further vital piece of evidence. Previous solar neutrino experiments had all relied on detection channels involving the charged-current interaction, so they were only sensitive to the ν_e flux. SNO employed two separate detection methods: one was sensitive to electron neutrinos via the charged-current interaction, the other was sensitive to the flavour-blind neutral-current interaction. This allowed them to measure both the ν_e rate and the total neutrino scattering rate. The results were consistent with the ν_e flux accounting for only $\sim 34\%$ of the total flux of solar neutrinos at energies > 5 MeV, confirming the presence of neutrino flavour transformations [142].

3.2.2   Three-neutrino mixing

The observations of flavour transformations in solar neutrinos could be explained in a model with only two neutrino species. However, by the late 1970s the tau lepton had been discovered, and it seemed probable that a third neutrino flavour state, ν_τ, also existed [143]. A third, linearly independent neutrino flavour state would imply the presence of three neutrino mass eigenstates, and oscillations could occur between

all three flavours. The tau neutrino would eventually be detected by the DONUT collaboration in 2000 [144].

The theoretical framework for three-neutrino mixing is very similar to that of two-neutrino mixing. However, as oscillations can now occur between all three flavour eigenstates, more parameters are required to describe the mixing. The 3×3 unitary mixing matrix required for Equation (3.2.1) is called the Pontecorvo-Maki-Nakagawa-Sakata (PMNS) matrix. We will not discuss it in great detail here, but a good review can be found in Ref. [145]. The PMNS matrix contains three independent mixing angles: θ_{12}, θ_{13}, and θ_{23}, and at least one CP-violating phase, δ_{CP}. These parameters, along with the mass splittings Δm_{21} and Δm_{31}, allow a full description of oscillations between three neutrino flavours.

Over the past 20 years, the neutrino oscillation parameters have been studied through a wide range of dedicated experiments. Reactor experiments allow study of oscillations over short-to-medium distances [146–148], while accelerator-based neutrino beams can be studied over extremely long baselines [149–151]. Atmospheric neutrinos, produced from cosmic ray collisions in the upper atmosphere, are studied to understand the oscillations of high-energy neutrinos [152, 153], and solar neutrino experiments continue to play an important role. In particular, Super-Kamiokande continues to gather data [154], and the Borexino experiment has measured the solar neutrino spectrum at low energies, providing precise measurements of the monochromatic ^{7}Be lines which will be of particular importance later in this thesis [155]. The results of these various experiments are combined to perform global fit analyses, and most of the oscillations parameters are now known to a precision of a few percent [156].

Despite these great successes, several properties of neutrinos are still unknown. While the mass splittings have been inferred from neutrino oscillation lengths, neither the absolute masses, nor the mass-ordering of the ν_i eigenstates are currently known. Also, although only one CP-violating phase is required in the PMNS matrix, two others may also be present. These additional phases would not affect oscillations,

but are linked to perhaps the most significant remaining unknown in the theory of neutrino physics: the nature of the neutrino mass.

3.3   The neutrino mass

Neutrinos in the SM are massless fermions that interact only via the weak interaction, a chiral gauge interaction that couples only to the left- and right-handed fermion and antifermion fields, respectively. As a result, neutrinos in the SM transform as a two-component Weyl fermion describing the left-handed neutrino and right-handed antineutrino. However, the presence of neutrino oscillations means that neutrinos possess a small, non-zero rest mass. Any neutrino mass term must couple a left-handed field to a right-handed field. The question is therefore: what is the nature of the neutrino mass, and specifically, what is the nature of the right-handed field in said term?

3.3.1   The Dirac mass

All the SM fermions, besides neutrinos, have mass terms that couple a left- and a right-handed component of their fields:

$$\mathcal{L}_m = -m\overline{\psi}\psi = -m(\overline{\psi}_L \psi_R + \overline{\psi}_R \psi_L). \tag{3.3.1}$$

Here ψ_L and ψ_R are understood as two separate fields, with only the ψ_L field carrying a charge under the $SU(2)_L$ group.

The two-component Weyl spinors of each chirality are therefore combined into a four-component Dirac spinor, representing the left- and right-chirality states of a particle and its antiparticle. Such a term cannot be written directly into the SM Lagrangian without violating gauge invarience, as the left- and right-handed fields transform differently under the electroweak symmetry. Instead, fermions acquire their masses via a Yukawa coupling with the Higgs field, and the spontaneous

breaking of the electroweak symmetry. The Feynman diagram for this interaction is shown in Figure 3.7, and the resulting mass term takes the form

$$\mathcal{L}_m^{ij} = -\frac{v}{\sqrt{2}} y_{ij} \overline{\psi}_L^i \psi_R^j + \text{h.c.} \,, \tag{3.3.2}$$

with y_{ij} the Yukawa coupling of the fermion to the Higgs field and v the Higgs vev [5].

A neutrino mass could be generated in the same way, with a few important consequences. Firstly, it would require the addition of a new field: the right-handed neutrino, which would transform as a singlet under all SM symmetries. Since the right-handed neutrino would not interact via any SM forces, it has been suggested that it could form a portion of the dark matter in the universe [157]. Secondly, it would introduce a coupling to the Higgs field, with a Yukawa matrix connecting the different neutrino fields. Since neutrino masses are constrained to be $\lesssim 0.2$ eV [158], the Yukawa couplings would have to be $< 10^{-12}$, more than six orders of magnitude smaller than the next smallest Yukawa coupling. This requires a large degree of fine-tuning, and a more natural way of generating a very small neutrino mass would seem preferable.

3.3.2   The Majorana mass

An alternative mass term can be constructed without introducing any new fermion fields, by noting that the charge-conjugate of a left-handed field acts as a right-handed field:

$$\{\psi_L\}^c = C\overline{\psi}_L^T = \{\psi^c\}_R, \tag{3.3.3}$$

with C the charge-conjugation matrix. A Majorana fermion satisfies the Majorana condition,

$$\psi = \psi^c, \tag{3.3.4}$$

so that the right-handed component of the fermion field is simply the charge-conjugate of the left-handed field, $\psi_R = \{\psi_L\}^c$. It can be shown (see e.g. Ref. [159])
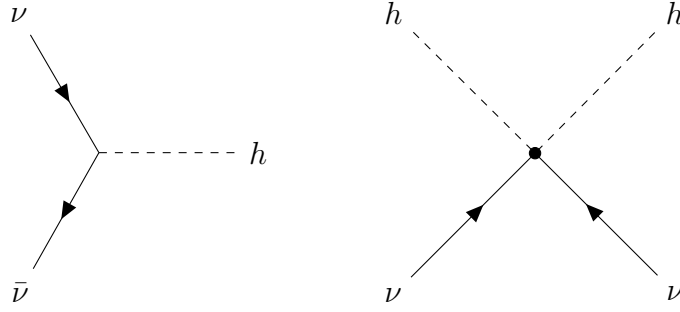
Figure 3.7: *Left:* Feynman diagram showing the neutrino Yukawa
interaction. After electroweak symmetry breaking the
Higgs acquires a vev and this operator leads to a Dirac
mass term for the neutrino. *Right:* Equivalent Feynman
diagram for the dimension-5 Weinberg operator. After
symmetry breaking this leads to a Majorana mass term
for the neutrino.

that such a field satisfies the Dirac equation for a massive fermion, without the need
for an additional right-handed Weyl spinor.

If neutrinos are Majorana fermions, their mass term in the Lagrangian will take the
form

$$\mathcal{L}_m = -\frac{m}{2}\overline{\nu_L^c}\nu_L + \text{h.c.}. \tag{3.3.5}$$

However, much like the Dirac mass term in Equation (3.3.1), this term violates
gauge invariance in the SM. The lowest-dimension gauge-invariant operator that can
generate this term is the Weinberg operator,

$$\mathcal{L}_W = \frac{\lambda_{ij}}{2\Lambda}L^i H L^j H, \tag{3.3.6}$$

with L^i a lepton field, H the Higgs field, and Λ a higher energy scale required to
make the operator renormalisable. This dimension-5 operator couples two incoming
neutrino fields to two Higgs fields, as shown in Figure 3.7. As this is a dimension-5
operator, it violates unitarity at high energy, and so can only exist as the low-energy
realisation of some higher-energy physics. This new, high-energy physics can provide
a natural way of generating a small neutrino mass, for example through one of the

see-saw models, which suppress the light neutrino masses by a factor related to the scale of the new physics[1]. For a review of these models see e.g. Refs [160, 161].

Besides providing a natural way of generating small neutrino masses, Majorana neutrino models have several important phenomenological consequences. The first and most important is that they lead to lepton number violation. In models with Majorana neutrinos, the particles we identify as antineutrinos are simply the right-handed components of the neutrino field, and they are coupled to the left-handed component by the Majorana mass term. The most definitive signature of Majorana neutrinos would therefore be the observation of LNV processes. The most famous of these is neutrinoless double beta decay ($0\nu\beta\beta$), and many experiments have searched for signatures of this process [162].

The nature of the neutrino mass also has consequences for the PMNS matrix. As mentioned in Section 3.2.2, the PMNS matrix contains at least one CP-violating phase, δ_{CP}. However, since Majorana neutrinos have two fewer independent field components than Dirac neutrinos, two additional complex phases would remain in the PMNS matrix which could not be absorbed by a redefinition of the fields. However, these additional complex phases would not affect neutrino oscillations, and only play a role in LNV processes [163].

Neutrino oscillations are now well understood, but there are still some neutrino scattering processes that have not been measured to high precision. There is therefore room for new physics beyond the SM that could affect neutrino scattering cross sections, especially at low energies (at or below a few keV). In the next chapter, we will explore some of these models of new physics, and see how dark matter direct detection experiments will soon become ideal laboratories in which to study low-energy physics in the neutrino sector.

---

[1]Many such models actually employ a combination of Dirac and Majorana mass terms, but they still lead to the consequences described below.

Chapter 4

New physics in the neutrino sector

Although neutrino masses and oscillations require some element of physics beyond the SM, we have so far discussed only the most minimal extensions to SM physics that are required to explain observed phenomena. In this chapter, we will be discussing models of physics that go explicitly beyond the SM by introducing new fields and interactions that may or may not be realised in nature. The remainder of the work will examine the implications of these models for the future of DD experiments.

These models of new physics are motivated to varying degrees either by their ability to resolve tensions in existing observations, their presence within a particular theoretical model of higher-energy physics, or simply by their ability to generate observable signatures that have not yet been ruled out by experiment. We will discuss these specific motivations when we introduce the individual models of new physics. The common feature they share is that each model introduces a new light particle that can mediate interactions between neutrinos and other SM particles, thereby changing the cross sections of these interactions. We are particularly interested in light mediators, as the changes they induce in scattering rates are more pronounced at low energies, where low-threshold DD experiments have an advantage over many larger neutrino detectors.

Before introducing the new physics models themselves, we will first consider the processes through which neutrinos can interact within DD experiments.

4.1   Neutrino scattering in DD experiments

DD experiments measure the signals of particles scattering with the components of atomic matter: electrons and nuclei. In Chapter 2, we considered WIMPs scattering coherently with entire nuclei at low recoil energies, and accounted for the loss of coherence at higher energies with a nuclear form factor, $F_{SI}(E_R)$. The same argument can be applied to neutrinos scattering with these recoil energies, since the nuclear response depends only on the momentum transferred during the collision, and not the species of particle that induced the scattering event.

Coherent elastic neutrino-nucleus scattering (CEνNS) proceeds in the SM via the exchange of a neutral vector boson, the Z. Since the energy transfer, E_R, is much smaller than the Z mass, we can calculate the CEνNS cross section using Fermi's effective theory, where

$$\frac{d\sigma_{\nu A}^{\rm SM}}{dE_R} = \frac{G_F^2}{4\pi} Q_w^2 m_A \left(1 - \frac{m_A E_R}{2E_\nu^2}\right) F^2(E_R), \qquad (4.1.1)$$

with E_ν the neutrino energy, G_F Fermi's coupling constant, and $Q_w = N - (1 - 4\sin^2\theta_w)Z$ the weak nuclear hypercharge. The inclusion of spin-dependent terms in the CEνNS cross section reveals an asymmetry between the cross sections for neutrino and antineutrino scattering. However, when averaged over all nucleons in heavy nuclei and those with no overall nuclear spin, the resulting cross sections are nearly identical, and we obtain the result in eq. (4.1.1) [164].

CEνNS was first predicted over 40 years ago [165], but the low energies at which it occurs made it extremely challenging to observe. The first direct observation was made in 2017 by the COHERENT experiment [166]. The experiment detected neutrinos generated by the Spallation Neutron Source (SNS), which, in addition to its high-intensity neutron beam, generates significant numbers of ν_e, ν_μ, and $\overline{\nu}_\mu$ neutrinos, with energies averaging a few tens of MeV. The measurements made by COHERENT place constraints on new physics contributions to the CEνNS cross section. However, we will see in Chapter 5 that DD experiments have the potential

to probe CEνNS at lower energies, and may therefore be able to explore models of new physics to which COHERENT is less sensitive.

Neutrinos can also scatter within DD experiments with atomic electrons. As was discussed in Section 2.2, electron scattering events are often rejected by DD experiments as they usually comprise the majority of background events. For some experiments, however, this is not the case, and understanding the neutrino-electron scattering rate will be important.

Unlike CEνNS, the cross section for neutrino-electron scattering depends on the flavour of the incoming neutrino. For ν_μ and ν_τ states, the scattering proceeds only through exchange of a Z boson, the so-called neutral current. For ν_e scattering, however, an additional channel exists: the charged current, mediated by the charged W boson. The resulting SM cross section can be written as

$$\frac{d\sigma_{\nu e}^{\text{SM}}}{dE_R} = \frac{2\,G_F^2\,m_e}{\pi}\left[g_1^{\alpha 2} + g_2^{\alpha 2}\left(1 - \frac{E_R}{E_\nu}\right)^2 - g_1^\alpha\,g_2^\alpha\,\frac{m_e\,E_R}{E_\nu^2}\right],$$

where g_1^α and g_2^α are couplings describing the weak interaction. The additional channel for ν_e scattering is encoded as a difference in these couplings, so

$$g_1^e = \sin^2\theta_w + \frac{1}{2};\ \ g_2^e = \sin^2\theta_w;$$

$$g_1^{\mu,\tau} = \sin^2\theta_w - \frac{1}{2};\ \ g_2^{\mu,\tau} = \sin^2\theta_w. \tag{4.1.2}$$

Various experiments have utilised neutrino-electron scattering as an avenue to study neutrinos. However, most of these have studied the process at energies far greater than those probed at DD experiments. Borexino, which has performed the lowest-energy measurements of neutrino-electron scattering to-date, had a lower analysis threshold of 190 keV [155]. Any neutrino-electron scattering in DD experiments would therefore occur at energies which have not yet been directly probed.

We have introduced the scattering processes by which neutrinos may produce signals within DD experiments, and seen their cross sections in the SM. In Chapter 5, we will discuss the consequences of this scattering for the DD experiments themselves.

Before that, though, we will introduce our models of new physics and consider their effects on the neutrino scattering cross sections discussed above.

4.2 Simplified models of new physics

When considering the effects of new physics on a process, there are a few different approaches one can take. One can adopt a top-down approach, and consider a theoretically motivated extension to the fundamental physics of the SM, for example a modification to the underlying gauge structure. If the effects of such a modification on low-energy phenomena are well-enough understood, measurements of these phenomena can be used to place constraints on the model. However, these effects can be very complex and many new fields may be introduced, often requiring us to constrain many free parameters. Furthermore, any constraints placed on such a model will be specific to that model, and may be circumvented by a modification to the underlying theory.

At the other extreme, one can attempt to adopt a completely model-agnostic approach. In this strategy, one attempts to parametrise any possible modification to a physical observable which could result from some unknown model of new physics. By placing limits on these parameters directly, one obtains constraints that should be model-independent, and they can be translated into constraints on specific models by identifying how these models would generate such a change in the observable. However, these approaches still require some assumptions about the new physics they are intended to represent.

Many searches for new physics are focused on the high-energy frontier, in which additional fields have masses beyond the reach of current particle accelerators. When considering the effects of this type of physics on present observations, an effective field theory (EFT) approach can be adopted. Examples of this type of approach include the non-relativistic EFT we introduced in Chapter 2, and other EFTs such as the Standard Model effective field theory (SMEFT) [167] and neutrino non-standard

interactions (NSIs) [168]. However, these EFTs are only valid up to some cut-off in energy related to the scale of the underlying new physics.

In recent years there has been increased interest in new light physics, which could exist at an energy far below the electroweak scale. Particles at these masses could exist undetected if their couplings to SM particles are sufficiently small. These models are motivated partly by their ability to connect the SM to an otherwise secluded sector, and partly by the observation of discrepancies in certain low-energy observables, which we will discuss further in Chapter 7. Alternatively, their study may be motivated simply by the fact that they represent a parameter space to which upcoming detectors will be increasingly sensitive.

As some of the measurements we will be using to constrain these models have been made at energies comparable to the scale of the new physics, we cannot adopt an EFT approach to study them. Instead, we will consider a collection of simplified models, in which we introduce only a single new field with a mass in the MeV-GeV range. We will examine the effects of such a field, which acts as a mediator for interactions between SM particles, under various assumptions about its nature. In each case, the additional mediator will provide an additional channel through which the scattering processes described in Section 4.1 can occur. The cross sections for these processes will gain additional new physics (NP) terms, so in general

$$\frac{d\sigma_{\nu A}}{dE_R} = \frac{d\sigma_{\nu A}^{\text{SM}}}{dE_R} + \frac{d\sigma_{\nu A}^{\text{NP}}}{dE_R} \qquad (4.2.1)$$

We will consider two main classes of light mediators, divided based on their spin: a spin-1 vector mediator, and a spin-0 scalar. We will consider a few different simplified models that introduce one of these mediators alongside the other fields of the SM, and examine the resulting new physics contribution to the neutrino scattering processes discussed in Section 4.1.

4.2.1   Light vector mediators

In general, a simplified model need not be based on any specific theory of physics beyond the SM. However, it can still be useful to consider some of the underlying physics that can lead to the presence of a particular mediator, and use this as a guide to ensure the model obeys certain laws, such as Lorentz invariance, and that the resulting work is relevant to the wider physics community. With that in mind, for our vector mediated models we considered various vector gauge bosons that can result from the introduction of a new $U(1)$ gauge symmetry to the SM.

In the SM there exist a number of accidental global symmetries, specifically baryon number and lepton number. In the SM the individual components of lepton number: L_e, L_μ, and L_τ are also conserved, though it is known that this conservation is not respected by neutrino oscillations. A new $U(1)$ gauge symmetry could be included by gauging one of these global symmetries: $U(1)_B$, $U(1)_{L_e}$, $U(1)_{L_\mu}$, or $U(1)_{L_\tau}$, but doing so leads to high-energy anomalies that ultimately break gauge invariance.

However, certain combinations of these symmetries can be gauged so that the resulting anomalies exactly cancel: $U(1)_{L_e-L_\mu}$, $U(1)_{L_\mu-L_\tau}$, or $U(1)_{L_e-L_\tau}$. The $U(1)_{B-L}$ gauge symmetry can also be made anomaly-free if right-handed neutrinos are included. Right-handed neutrinos should also be included into the $U(1)_{L_e-L_\mu}$, $U(1)_{L_\mu-L_\tau}$, or $U(1)_{L_e-L_\tau}$ in order to produce a lepton mixing matrix that agrees with observations [169].

The introduction of a new $U(1)$ gauge symmetry results in the presence of a new vector gauge boson, that we denote X_α. If the $U(1)$ symmetry is broken, we must perform a rotation to the mass basis and redefine our fields, yielding a Z' boson whose mass is in principle unrelated to the electroweak scale. For masses below ~ 1 MeV, couplings are strongly constrained by measurements of the CMB and other data from cosmology and astrophysics [170, 171], while above a few GeV constraints from colliders dominate over the types of experiment we are interested in [172]. We will therefore focus on the parameter space within the approximate range from 1

MeV to 1 GeV.

When we rotate to the mass basis, the Z' can acquire a kinetic mixing with the SM neutral gauge currents, leading to terms in the Lagrangian of the form

$$L \supset \left(\frac{g}{c_W} \epsilon' J_Z^\alpha + e\epsilon J_{\text{em}}^\alpha \right) Z'_\alpha \, , \tag{4.2.2}$$

with J_Z^α and J_{em}^α the weak neutral current and the electromagnetic current. Here we have expanded to first order in the mixing parameters ϵ and ϵ', which parametrise the mixing of the Z' with the photon and the Z boson, respectively, assuming the mixing parameters are small.

In principle these terms can arise at tree level, with mixing parameters unrelated to the couplings of the Z' to SM fermions. However, such terms are forbidden in many UV models from which additional $U(1)$ symmetries emerge [3, 169], and so we will set ϵ and ϵ' equal to zero at tree level. If, however, the Z' couples to any SM fermions that also couple to the Z and the photon, kinetic mixing terms will be generated at loop level, as seen in Figure 4.1. The Z' can then couple to all SM fermions via this kinetic mixing, even if it only couples to a subset of SM fermions at tree level. This loop-induced coupling will naturally be suppressed relative to the tree-level couplings, so we will only consider its effects on scattering processes which are not mediated by the Z' at tree level in a given model.

We will consider two of these gauge symmetries in more detail: the $U(1)_{B-L}$ and the $U(1)_{L_\mu-L_\tau}$. We choose these models in particular as they lend themselves to study via CEνNS.

The $U(1)_{B-L}$ model

In the $U(1)_{B-L}$ model, SM baryons have a charge of $+1$ under the new symmetry, while leptons have a have of -1. The coupling to all SM fermions is therefore fixed by a single coupling constant, g_{B-L}, and both CEνNS and neutrino-electron scattering can occur at tree level via the exchange of a Z', in a manner analogous to the weak
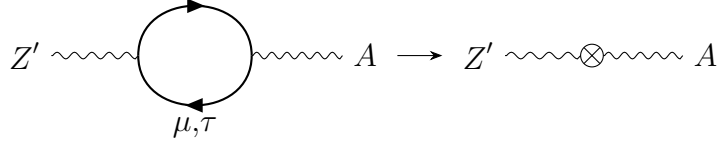
Figure 4.1: The loop diagram through which the Z' couples to electrons and nucleons in the $U(1)_{L_\mu - L_\tau}$ can be understood as an effective coupling with the electromagnetic current through kinetic mixing between the Z' and the photon.

neutral current interaction.

As the single coupling g_{B-L} parametrises the couplings to all SM fermions, constraints on the $U(1)_{B-L}$ can be obtained from many sources. Within our mass range of interest, leading constraints arise from sources as diverse as fixed target beam dump experiments [173, 174], dedicated neutrino experiments [175, 176], LHC constraints [172], and arguments from cosmology [170]. A full landscape of constraints is shown in Figure 4.2. The various constraints are discussed in detail in Ref. [177].

The resulting new physics contribution to the CEνNS cross section can be written as

$$\frac{d\sigma_{\nu A}^{\mathrm{NP}}}{dE_R} = \left(1 - \frac{m_A E_R}{2E_\nu^2}\right)$$
$$\left[-\frac{G_F g_{B-L}^2 Q_w Q'_{\nu A} m_A}{\sqrt{2}\pi \left(2E_R m_A + m_{Z'}^2\right)} + \frac{g_{B-L}^4 Q'^2_{\nu A} m_A}{2\pi \left(2E_R m_A + m_{Z'}^2\right)^2}\right] F^2(E_R), \quad (4.2.3)$$

where $Q'_{\nu A} = -A$ is the coherence factor, given by the product of the charges of the neutrino and nucleus under the $U(1)_{B-L}$ symmetry. The second term in Equation (4.2.3) is the "pure" BSM contribution to the cross section, containing the square of the matrix element for scattering via the exchange of a Z'. The first term emerges from the interference between the SM and BSM channels. Note that the overall minus sign on the interference term and the negative charge of the neutrino under the $U(1)_{B-L}$ symmetry lead to a positive interference term for all kinematically allowed combinations of E_R and E_ν.
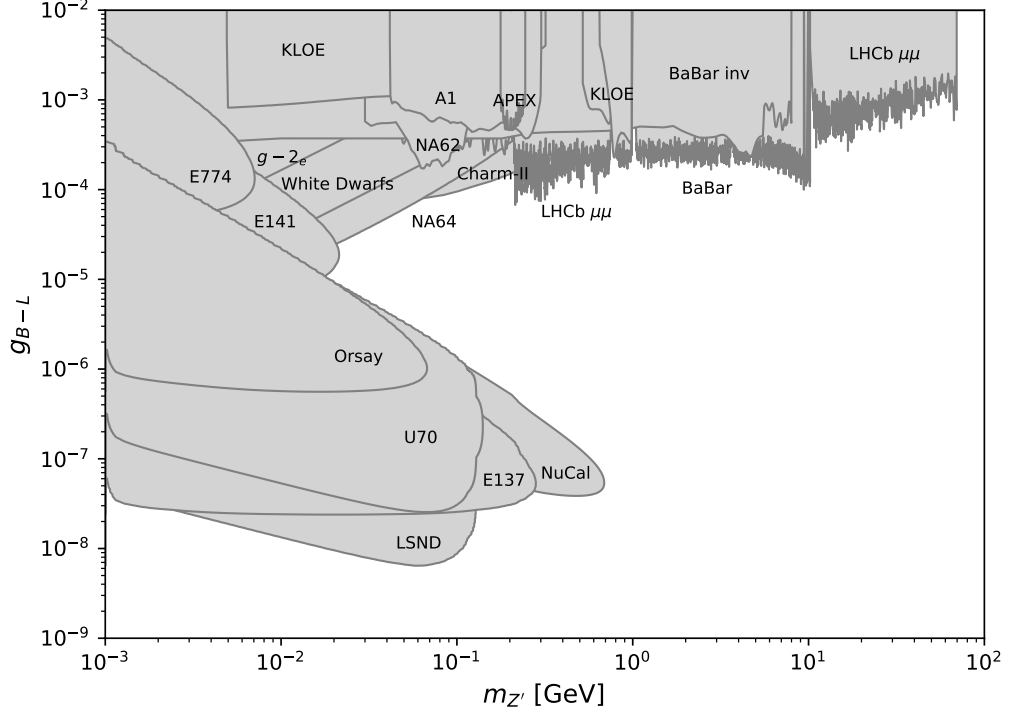
Figure 4.2: Constraints on the parameter space of a new $U(1)_{B-L}$
gauge symmetry, as they appeared in July 2018. An
explanation of the sources of these constraints can be
found in Ref. [177].

The new physics contribution to the neutrino-electron scattering cross section is

$$\frac{d\sigma_{\nu_\alpha e}^{\text{NP}}}{dE_R} = \frac{2\,G_F^2\,m_e}{\pi} \left\{ \frac{g_{B-L}^2}{\sqrt{2}\,G_F(2m_e E_R + m_{Z'}^2)} \left[g_1^\alpha + g_2^\alpha \left(1 - \frac{E_R}{E_\nu}\right)^2 - (g_1^\alpha + g_2^\alpha)\frac{m_e E_R}{2E_\nu^2} \right] \right.$$
$$\left. + \frac{g_{B-L}^4}{8\,G_F^2(2m_e E_R + m_{Z'}^2)^2} \left[1 + \left(1 - \frac{E_R}{E_\nu}\right)^2 - \frac{m_e E_R}{E_\nu^2} \right] \right\}, \quad (4.2.4)$$

where $g_{1,2}^\alpha$ are those defined in Equation (4.1.2).

The $U(1)_{L_\mu - L_\tau}$ model

As with the $U(1)_{B-L}$, there is a single coupling constant, $g_{\mu\tau}$, that describes the
strength of the coupling to SM fermions. Unlike the $U(1)_{B-L}$, however, under the
$U(1)_{L_\mu - L_\tau}$ only leptons in the muon and tau families carry a charge: μ and ν_μ have
charge $+1$, τ and ν_τ have charge -1. At tree level, the new field will only mediate

f	e	ν_e	μ, ν_μ	τ, ν_τ	q_d	q_u
c_f	$\epsilon_{\mu\tau} e$	0	$g_{\mu\tau}$	$-g_{\mu\tau}$	$\frac{1}{3}\epsilon_{\mu\tau} e$	$-\frac{2}{3}\epsilon_{\mu\tau} e$

Table 4.1: Coupling coefficients c_f for the interaction of the massive vector boson Z' to the fermionic vector current $\bar{f}\gamma^\alpha f$ of SM particles at leading order in the mixing parameter $\epsilon_{\mu\tau}$. The couplings to q_u and q_d are also valid for equivalently charged second- and third-generation quarks.

interactions between these four fermions, so any scattering with atomic matter will have to occur through the loop-induced kinetic mixing seen in Figure 4.1.

This kinetic mixing can be expressed as a redefinition of the couplings between the Z' and SM fermions, with terms in an effective Lagrangian of the form

$$\mathcal{L}_{fA'} = -c_f \, \bar{f}\gamma^\alpha f \, Z'_\alpha. \tag{4.2.5}$$

Since the coupling induced by kinetic mixing will be suppressed compared with $g_{\mu\tau}$, we neglect the kinetic mixing contributions to the couplings with second- and third-generation leptons. We further neglect couplings generated via mixing with the SM Z boson, due to the comparative size of the weak and electromagnetic coupling constants. Note that this means we have no coupling to neutral particles, such as the ν_e or the neutron. This is a valid approximation because the contribution to the cross section from other neutrino flavours and from protons in the nucleus will be dominant. The effective couplings with all SM fermions are given in Table 4.1. For a full derivation see Ref. [177].

The loop-induced kinetic mixing parameter is given by

$$\epsilon_{\mu\tau}(q^2) = \frac{e \, g_{\mu\tau}}{2\pi^2} \int_0^1 dx \, x(1-x) \left[\log \left(\frac{m_\mu^2 - x(1-x)q^2}{m_\tau^2 - x(1-x)q^2} \right) \right], \tag{4.2.6}$$

where e is the electromagnetic coupling constant and q is the momentum transferred in the scattering event. In the limit when $q^2 << m_\mu^2$, which is valid for all the

processes discussed in this work, the mixing is approximately constant,

$$\epsilon_{\mu\tau}(q^2 \ll m_\mu^2) \approx \frac{e\, g_{\mu\tau}}{6\pi^2} \log\left(\frac{m_\mu}{m_\tau}\right) \sim -\frac{g_{\mu\tau}}{70}\,, \tag{4.2.7}$$

and the coupling via kinetic mixing is indeed suppressed compared with $g_{\mu\tau}$.

Any new physics contribution to the CEνNS or neutrino-electron scattering cross section will involve at least one particle that only couples to our mediator via kinetic mixing. It may therefore seem that any new physics contribution will be heavily suppressed compared with the contribution in the $U(1)_{B-L}$ model. However, the constraints from most other experiments will be similarly affected. In fact, any constraint based on scattering with only first-generation fermions will be at a greater disadvantage, as neutrino-scattering probes can benefit from the direct coupling of ν_μ and ν_τ to the new mediator.

The landscape of constraints prior to our work is shown in Figure 4.3. In Chapter 7 we will update some of these constraints based on more recent data, and see how future experiments, including DD experiments, will allow us to probe further regions of the parameter space.

The new physics contribution to the CEνNS cross section from the $U(1)_{L_\mu - L_\tau}$ mediator is given by

$$\frac{d\sigma_{\nu_\alpha A}^{\mathrm{NP}}}{dE_R} = \left(1 - \frac{m_A E_R}{2E_\nu^2}\right)$$
$$\times \left[\frac{G_F\, e\, \epsilon_{\mu\tau}\, g_{\mu\tau}\, m_A\, Q'_{\nu_\alpha A}\, Q_{\nu N}}{\sqrt{2}\pi(2m_A E_R + m_{Z'}^2)} + \frac{e^2\, \epsilon_{\mu\tau}^2\, g_{\mu\tau}^2\, m_A\, Q'^2_{\nu_\alpha A}}{2\pi(2m_A E_R + m_{Z'}^2)^2}\right] F^2(E_R)\,. \tag{4.2.8}$$

Here the coherence factor, $Q'_{\nu_\alpha A} = Z Q'_{\nu_\alpha}$, here depends on the number of protons in the nucleus, Z, since the dominant coupling is via mixing with the photon. Also, the sign of the first term, which arises from interference between the SM and new physics diagrams, crucially depends on the neutrino flavour, due to the different charges under the $U(1)_{L_\mu - L_\tau}$ symmetry: $Q'_{\nu_\mu} = +1$; $Q'_{\nu_\tau} = -1$. The scattering cross section with muon neutrinos can therefore be suppressed compared with the SM cross section in certain regions of the parameter space.
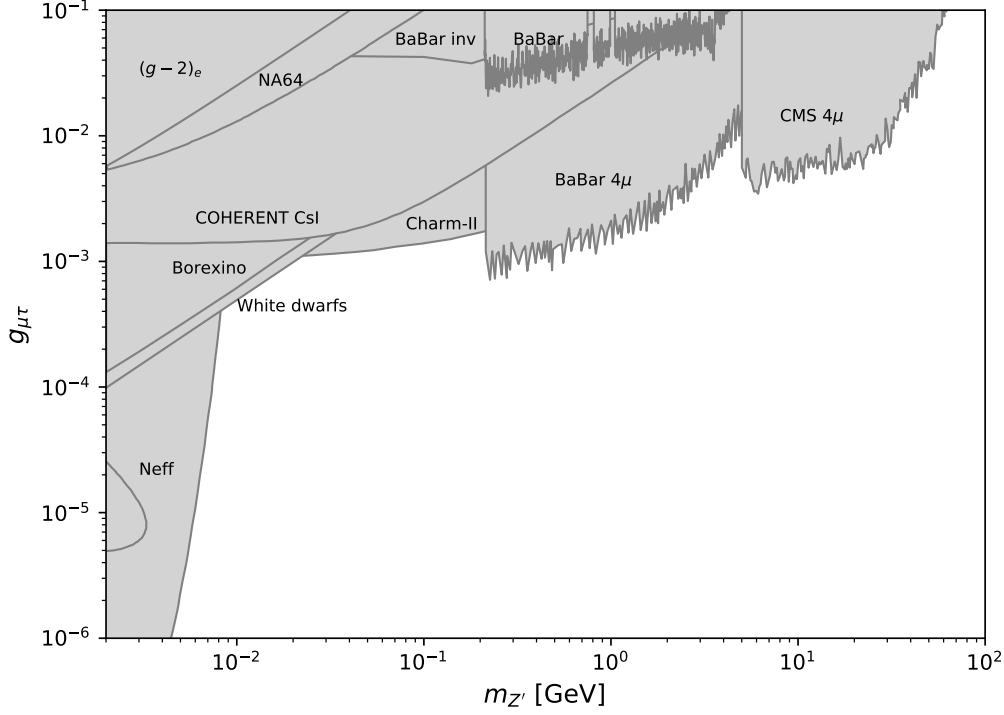
Figure 4.3: Constraints on the parameter space of a new $U(1)_{L_\mu - L_\tau}$ gauge symmetry, excluding any updates made as part of my work described in Chapter 7. An explanation of the sources of these constraints can be found in Refs. [3,177].

The new physics contribution to the cross section for neutrino-electron scattering also depends on the flavour of the neutrino. As with the CEνNS cross section, this flavour dependence is captured by the neutrino charge under the new symmetry, Q'_{ν_α}, so

$$
\frac{d\sigma_{\nu_\alpha e}^{\mathrm{NP}}}{dE_R} = \frac{2\,G_F^2\,m_e}{\pi}
$$

$$
\times \left\{ \frac{g_{\mu\tau}\,e\,\epsilon_{\mu\tau}\,Q'_{\nu_\alpha}}{\sqrt{2}\,G_F(2E_R\,m_e + m_{Z'}^2)} \left[(g_1^\alpha + g_2^\alpha)\left(1 - \frac{m_e E_R}{2E_\nu^2}\right) - g_2^\alpha \frac{E_R}{E_\nu}\left(2 - \frac{E_R}{E_\nu}\right) \right] \right.
$$

$$
\left. + \frac{g_{\mu\tau}^2\,e^2\,\epsilon_{\mu\tau}^2\,Q_{\nu_\alpha}^{'2}}{4\,G_F^2(2E_R\,m_e + m_{Z'}^2)^2} \left[1 - \frac{E_R}{E_\nu}\left(1 - \frac{E_R - m_e}{2\,E_\nu}\right)\right] \right\}. \qquad (4.2.9)
$$

The sign on the first term again depends on the neutrino flavour. Due to the negative electric charge on the electron, however, here the interference term can

lead to destructive interference in the tau neutrino cross section, while for muon neutrinos the new physics contribution is always positive.

4.2.2 Light scalar mediators

In addition to these vector models, we also considered the effects of a new scalar boson that couples to SM particles. Here, though, we did not find any models that were both suitable for study through neutrino scattering in DD experiments, and sufficiently better motivated than other models to justify their study above all others.

The introduction of new scalars is a feature of many models of new physics. Sometimes they form part of a secluded dark sector [178], and may form part or all of the universe's dark matter [179]. If such a scalar couples to SM particles, it can form a portal to the dark sector it inhabits. One intuitive way in which a dark scalar could interact with SM fermions would be through a mixing with the Higgs, as occurs in so-called Higgs portal models [180].

In a scenario in which the new scalar only couples to the SM sector via mixing with the Higgs, its effective couplings to SM fermions will be proportional to their Yukawa couplings to the SM Higgs, and therefore to their masses. However, the small masses of the neutrinos mean that if they couple to the SM Higgs at all, their Yukawa couplings are much smaller than the Yukawas of other fermions. Neutrino scattering would therefore be a poor channel through which to search for such a scalar.

A new scalar that couples directly to neutrinos can be motivated by attempts to more naturally generate a light neutrino mass. The phenomenology of such a model crucially depends on the nature of the neutrino mass. If the neutrino is a Dirac particle, it may acquire its mass term through interaction with a second Higgs field, with a vev much smaller than that of the SM Higgs [181]. This would allow the neutrino to have a larger, more natural Yukawa coupling to this light Higgs, which could then couple to other SM fermions either through mixing with the SM Higgs

or through an entirely independent set of Yukawa couplings.

If, conversely, the neutrino is a Majorana particle, new fields must exist in order to generate the required lepton number violating interactions. For example, the type-II seesaw model introduces a new scalar triplet field, leading to terms in the Lagrangian of the form

$$\mathcal{L} \supset (y_\nu)_{ab} \overline{\nu}_a^c \nu_b \Delta^0, \tag{4.2.10}$$

where Δ^0 is the neutral component of the scalar triplet [182]. While the fields required for this seesaw mechanism usually have masses much larger than those to which DD experiments are particularly sensitive, an additional light scalar field could mix with the scalar Δ to acquire a coupling of this form, while mixing with the SM Higgs field to acquire couplings to other SM fermions.

So, while it is possible that a new scalar field could exist which couples to SM fermions, including neutrinos, there is no model which fits our requirements quite as well as the gauged $U(1)$ models discussed in Section 4.2.1, for which only a single coupling constant parametrises the coupling strength to all SM fermions. In the absence of such a model, we wish to ensure our results are as applicable as possible to the wide range of potential new physics which may be of interest. We will therefore make as few assumptions as possible about the relative couplings between the new scalar and SM fermions, instead constraining directly the combination of couplings to which a given experiment is sensitive.

Our new scalar, ϕ, couples to neutrinos in a manner that either conserves lepton number (LNC), or violates it (LNV). In the former case, the neutrino-coupling term in the Lagrangian has the form

$$\mathcal{L}_{\text{LNC}} \supset (y_\nu)_{\alpha\beta} \phi \overline{\nu}_{\alpha,R} \nu_{\beta,L}, \tag{4.2.11}$$

while in the latter case it has the form

$$\mathcal{L}_{\text{LNV}} \supset \frac{(y_\nu)_{\alpha\beta}}{2} \phi \overline{\nu}_{\alpha,L}^c \nu_{\beta,L}. \tag{4.2.12}$$

If the light scalar plays an important role in the neutrino mass generation, a suitable mixing matrix $(y_\nu)_{\alpha\beta}$ must be chosen to correctly reproduce the observed neutrino mixing behaviour [183]. For simplicity, however, in the remainder of the work we will assume flavour-universal, diagonal couplings, so $(y_\nu)_{\alpha\beta} = y_\nu \delta_{\alpha\beta}$. Although this may not be well motivated physically, it greatly simplifies our parameter space, and it is likely that the constraints we place under this assumption could be rescaled to give equivalent constraints on a more complex matrix of Yukawa couplings.

Within specific models of neutrino mass generation, known features of the neutrino mass matrix can be used to constrain the properties of the additional fields which arise. For example, bounds on the sum and splittings of the neutrino masses can often be used to constrain the relationship between the masses, couplings, and vacuum expectation values of new scalar fields involved in neutrino mass generation [182, 184, 185]. However, these relationships are specific to the particular model being considered, and it is challenging to derive an overall constraint in the model-agnostic approach we have taken to the origin of our LNC and LNV scalars. The picture is further complicated by the possibility that the couplings of our scalar to some or all SM fermions are generated through mixing with other scalars, either the SM Higgs or other scalar fields which may be introduced in neutrino mass models. Some previous works have performed model agnostic analyses under additional constraining assumptions, for example the assumption that the additional scalar forms the majority of the DM in the universe [186, 187]. In Ref. [186], the requirement that a scalar DM candidate be stable was satisfied by enforcing the condition $m_\phi < m_{\nu_R}$. Under that choice, and using the requirements that both the DM relic density and neutrino mass properties agreed with current limits, stringent bounds were acquired on the properties of the scalar DM. While these specific assumptions make the bounds acquired incompatible with our parameter space, the work demonstrates that constraints from neutrino properties can be important when investigating a new, light scalar interacting with neutrinos. In this thesis, we do not attempt to derive such a constraint on our simplified models, but leave such an analysis to

future works.

In both the LNC and LNV case, the scalar can also couple to other SM fermions, with terms in the Lagrangian of the form

$$\mathcal{L}_{f\phi} = y_f \, \bar{f} f \, \phi \, . \tag{4.2.13}$$

In each case the final state particles differ from those in the SM. The LNC scalar couples left- and right-handed neutrino fields, so the outgoing neutrino field is a right-handed neutrino. In the LNV case, the right-handed component of the neutrino field is an antineutrino, so the outgoing particle is an antineutrino. In the case of an LNC scalar, then, the mass of the right-handed neutrino will have important consequences. We identify three possible scenarios:

- **Small m_{ν_R}:** If the mass of the right-handed neutrino is much smaller than the energies at which our scattering occurs ($\lesssim$ eV), our results will not be sensitive to its exact value, and the outgoing phase space of our scattering will not be significantly different from the SM case, where we have an outgoing ν_L.

- **Large m_{ν_R}:** If the right-handed neutrino mass is much larger than the scales at which we are scattering ($\gtrsim$ GeV), the scattering of neutrinos via the LNC scalar will be kinematically forbidden, and we will not obtain any constraints on y_ν using the arguments described below.

- **Intermediate m_{ν_R}:** If the right-handed neutrino mass falls somewhere between these two extreme cases, scattering via the LNC scalar may be forbidden for some of our lower-energy scattering processes, but allowed for our higher-energy events. If the mass fell within the range of energies probed by one of our DD experiments ($m_{\nu_R} \sim$ keV), we may observe some interesting signals in the neutrino scattering spectrum which could even be used to reconstruct the right-handed neutrino mass.

The latter case displays some interesting phenomenology, and may warrant future study. However, such an investigation is beyond the scope of this work. Instead, we

will assume the first case, in which the right-handed neutrino mass is too small to produce observable signatures in any of our experiments. This is the assumption that was implicitly made in Ref. [188], from which we took our initial constraints on these scalar models. In this case, the new physics contributions to our neutrino-scattering cross sections are the same for an LNC and LNV scalar with equal mass and couplings, although some of the constraints we consider are specific to one class of scalar or the other.

As we cannot observe the outgoing (anti-)neutrino, for our purposes the new physics scattering processes are indistinguishable from the equivalent SM process. However, due to this difference in the outgoing particles there is no interference term in the cross section of the kind we saw in the cross sections in Section 4.2.1.

The new physics contribution to the CEνNS cross section is

$$\frac{d\sigma_{\nu A}}{dE_R} = \frac{m_A^2 E_R y_\nu^2 Y_A^2}{4\pi E_\nu^2 (2m_A E_R + m_\phi^2)^2} F^2(E_R),$$
(4.2.14)

where $Y_A = ZY_p + NY_n$ is the coupling of the scalar to the nucleus at zero momentum transfer. The loss of coherence at higher momentum transfer is again encoded using a Helm form factor.

The effective couplings of the scalar to protons and neutrons can be computed from its fundamental couplings to quarks, by

$$Y_N = m_N \sum_q \left[y_q \frac{f_q^N}{m_q} \right] ; \; N \in \{n, p\},$$
(4.2.15)

with f_q^N the hadronic matrix elements for each quark flavour q in nucleon N [189–191]. The f_q^N can be found in Ref. [188]. Interestingly, in the absence of any extreme fine-tuning (for example near-perfect cancellation of the y_u and y_d terms), the overall couplings to protons and neutrons differ by at most $\mathcal{O}(10\%)$. We will therefore take the approximation that they are equal, $Y_n = Y_p = Y_N$, and define our constraints on Y_N, so our constraints will be mostly independent of the relative couplings to different quark flavours. The relevant combination of couplings for CEνNS is therefore $y_\nu Y_N$.

The new scalar mediator also contributes to the cross section for neutrino-electron scattering. The new physics contribution is

$$\frac{d\sigma_{\nu e}}{dE_R} = \frac{m_e^2 E_R y_\nu^2 y_e^2}{4\pi E_\nu^2 (2m_e E_R + m_\phi^2)^2} \,. \tag{4.2.16}$$

As with CEνNS, there is no interference between the SM and new physics channels, due to the difference in the chirality of the outgoing particles. Here the relevant combination of couplings is $y_\nu y_e$, so constraints from CEνNS do not necessarily equate to constraints on neutrino-electron scattering, or visa-versa, depending on the relative couplings y_e and Y_N.

As CEνNS will be the more important scattering process in most DD experiments, we will focus on constraints on the combination of couplings $Y = \sqrt{y_\nu Y_N}$. A collection of these constraints was found in Ref. [188]. Some of these constraints we have since reevaluated, but here I will introduce them as they stood prior to our work, which we discuss in the following chapters.

The constraints, as they appeared in 2018, are shown for both the LNC and LNV cases in Figure 4.4. They are derived from a wide range of measurements:

- **COHERENT:** The first measurement of CEνNS was made by the COHERENT collaboration using a 14.6 kg sodium-doped CsI detector and an intense source of neutrinos generated from pion decay at rest. The measured rate of CEνNS was consistent with the SM at the 1σ level [166], and this result has been used to place constraints on the combined coupling $Y = \sqrt{y_\nu Y_N}$.

- **Neutron-nucleus scattering:** Measurements of the scattering of neutrons with atomic nuclei at low energy can be used to constrain any new mediators that couple to nucleons [192–194]. This allows us to place constraints on Y_N, which can be combined with constraints on y_ν to calculate a constraint on Y.

- **Meson decay:** If a new mediator couples to neutrinos, it opens up new final states for meson decays due to emission from a final-state neutrino, for example
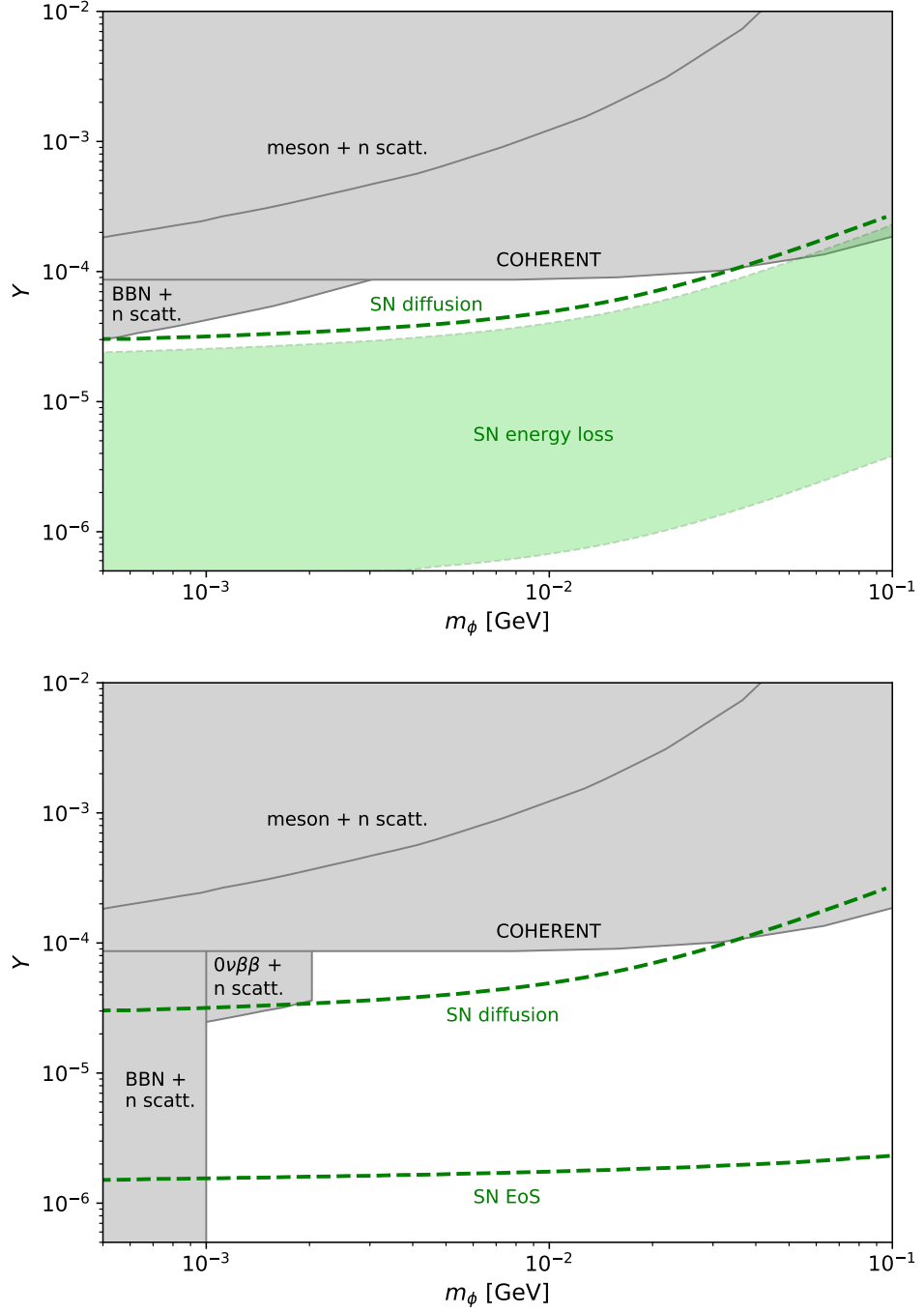
Figure 4.4: *Top:* Constraints on the combination of couplings $Y = \sqrt{y_\nu Y_N}$ for a lepton number conserving (LNC) scalar. The dashed green lines indicate constraints derived from supernova physics. They are subject to additional uncertainties, which are discussed further in Section 5.3. *Bottom:* Equivalent constraints on a lepton number violating (LNV) scalar.

$\pi^+ \to l^+ \nu \phi$. Measurements of branching ratios in meson decay experiments can therefore be used to constrain y_ν [195].

- **Neutrinoless double-beta decay:** If the new scalar violates lepton number, it can mediate neutrinoless double-beta decay ($0\nu\beta\beta$). Rather than emitting two antineutrinos, only a single scalar ϕ would be emitted, leading to measurable effects on the beta decay spectrum [196]. This allows us to place constraints on $(y_\nu)_{ee}$ below a certain mass.

- **BBN constraints:** The number of effective degrees of freedom (N_{eff}) at the time of Big Bang nucleosynthesis (BBN) cannot deviate too far from the SM value without upsetting the agreement between our understanding of BBN and observed abundances of light elements in the universe. In the case of an LNV scalar, ϕ can be produced in large numbers via the process $\nu\nu \to \phi$. If $m_\phi \gtrsim 1$ MeV, most of the scalars will decay between neutrino decoupling and BBN, leading to no change in N_{eff} at that time. If, however, $m_\phi \lesssim 1$ MeV, N_{eff} will be affected, leading to a strong constraint on the coupling y_ν. The constraint from BBN on the LNV scalar therefore appears as a vertical line in Figure 4.4. While this argument is quite approximate, the authors of Ref. [188] note that this result agrees with other works in which the full Boltzmann equation is solved [170].

  In the case of an LNC scalar, production of ϕ is suppressed, and no constraint can be obtained from N_{eff} due to production of the new scalar. However, the presence of the scalar allows production of right-handed neutrinos, through processes such as $\nu_L \bar{\nu}_L \to \nu_R \bar{\nu}_R$. As we are assuming that our right-handed neutrinos are very light, they would contribute to N_{eff}, leading to a constraint on y_ν for an LNC scalar

- **Supernova bounds:** The final class of constraints considered in Ref. [188] are those from supernovae. In the extreme environments found within supernovae, even very weakly-coupled forces can have important effects, and there are

several channels through which such interactions can be constrained. However, the processes that power supernovae are complex, and in some cases are still not fully understood. We must therefore be aware that many constraints obtained from supernovae will be dependant on the particular models of supernova physics being used. In Section 5.3, we will discuss this in more detail as we attempt to refine some of the constraints presented in Ref. [188], but here we will simply introduce the constraints as they appear in that reference.

As was discussed in Chapter 3, in 1987 a sudden burst of neutrinos was detected in three particle physics experiments around the world, coinciding with the appearance of supernova SN1987A in the sky [124]. From these measurements, both the duration of the neutrino burst ($t \approx 10$ s) and its approximate luminosity were inferred. While these values are not known to great precision, they are in agreement with current models of supernova and particle physics. Constraints can therefore be placed on any processes that would cause the properties of the neutrino burst to deviate from those measured.

Constraints can, for example, be placed on the luminosity of any "exotic", beyond-standard-model particle that would be emitted from a supernova. The so-called Raffelt criterion [197] places an upper limit on this luminosity, above which so much energy would be lost from the nascent supernova that the observed luminosity of neutrinos could not be produced. A new field will violate this Raffelt criterion if it has a sufficiently large production cross section, but sufficiently small scattering cross sections that it can free-stream out of the supernova, carrying away energy without becoming trapped in the dense interior. Luminosity constraints therefore exclude a region of the parameter space between a lower and upper bound.

This argument has been used to place constraints on many new light particles, including new scalars [198], but the resulting excluded regions lie at couplings well below those we are sensitive to. In the case of an LNC scalar, however,

neutrinos can scatter with neutrons, changing chirality in the process. This leads to the production of right-handed neutrinos, which cannot then interact with the surrounding medium via the weak interaction. In Ref. [188], a constraint was obtained on regions of the LNC parameter space which would lead to a large production of these chirality states, and for which the cross section for scattering via the scalar mediator is too small to effectively trap the right-handed neutrinos. This is the origin of the "SN energy loss" constraints in Figure 4.4.

Whether the new scalar is LNC or LNV, the additional contribution to the neutrino-neutron scattering cross section will reduce the mean free path of neutrinos within the supernova. This will therefore lead to a change in the diffusion time, the time taken for a neutrino to escape the interior of the supernova, and ultimately, the observed duration of the neutrino burst measured on Earth. In Ref [188], the "SN diffusion" limit is placed when the contribution to the cross section from new physics is equal to that from the SM weak interaction, as this will cause the diffusion time to be "significantly affected". However, this is clearly a very approximate method for deriving a constraint. In Section 5.3 I will discuss our efforts to improve and refine this constraint from the neutrino diffusion time in supernovae.

Finally, if neutrino-neutron scattering is mediated by an LNV scalar, the incoming neutrino will be converted into an antineutrino. If the cross section for this interaction is sufficiently large, a significant fraction of the ν_e produced from electron capture in the supernova core will be converted into $\overline{\nu}_e$. The resulting deleptonisation of the proto-neutron star can lead to a conflict with traditional models of supernova dynamics, which require a certain density of leptons to strengthen the stellar core and prevent total collapse [199]. This limit is labelled "SN EoS" in Ref. [188], as the change in particle populations would affect the equation of state of the stellar core. However, it should be noted that these models of supernova dynamics struggle to reproduce the

observed properties of supernovae [200], so a disagreement with these models should not necessarily be taken as a true constraint on the particle physics model. Modern supernova models are generally less sensitive to changes in the core lepton fraction than early models were [201]. We will discuss the physical implications of this $\nu \to \bar{\nu}$ conversion further in Section 5.3.

The constraints from Ref. [188] are displayed in Figure 4.4. Clearly, the question of the reliability of the supernova constraints is important, as they have the potential to constrain the parameter space of new scalars at couplings well below the sensitivity of previous particle physics experiments. We will discuss this question further in the next chapter, as we begin to explore the effects of neutrino scattering at DD experiments, both as an exciting opportunity to place constraints on new physics, and as a formidable barrier to the future of dark matter direct detection.

Chapter 5

Neutrino physics in the dark matter parameter space

We have introduced the channels through which neutrinos can scatter with atomic matter, both in the SM and in various simplified models of new physics. In this chapter, we will consider the implications of neutrino scattering for future searches for dark matter at direct detection experiments.

As we discussed in Chapter 2, any search for the signals of DM (specifically WIMPs) scattering in DD experiments will in principle be subject to backgrounds from other particles scattering within the detector. The simplified DM detector we introduced in that chapter was assumed to be background-free, an assumption we made to avoid having to consider backgrounds specific to individual experiments. However, for some real-world detectors the approximation of zero background is indeed a valid one. They are able to reduce the rate of background events in their analyses to $\ll 1$ count across the full exposure, allowing a genuine "background free" search in which any events can reasonably be interpreted as a potential signal of physics beyond the SM [202].

Even in experiments that do not attempt such radical background elimination, backgrounds are mitigated through a variety of techniques, based on the known properties of SM backgrounds. Most SM backgrounds have much larger scattering

cross sections with atomic matter than DM. Those originating outside the detector can be attenuated with shielding, while radioactive elements that could emit radiation within the detector can be reduced through rigorous purification of construction materials. Any background events that do occur within the detector can be reduced through analysis cuts, for example by rejecting scattering events close to the surface of the detector, effectively turning the outer layers of the detector into further shielding for the inner fiducial volume. Finally, any surviving backgrounds are in general much more likely to be due to scattering with atomic electrons than with nuclei, so multiple detection channels are employed to discriminate between electronic and nuclear scattering events.

However, none of these strategies for background rejection are effective at reducing backgrounds from CEνNS. Neutrinos with energies in the $1 - 100$ MeV range are quite abundant, cannot be shielded against, and can induce keV scale nuclear recoils which would be very difficult to distinguish from those caused by DM particles. For WIMP candidates with very small couplings, then, any DD experiment with sufficient sensitivity to search for them will also be sensitive to a significant, irreducible background due to CEνNS[1]. This ultimately leads to a lower "discovery limit" on WIMP couplings, below which neutrino scattering will severely hinder their study at DD experiments, known as the neutrino floor [38].

The idea of projecting the effects of neutrino scattering onto a DM parameter space motivated Ref. [2], the work upon which the first part of this chapter is based. In that work, I collaborated with C. Boehm, D. Cerdeño, P. Machado, A. Olivares-del-Campo, and E. Perdomo to study the effects of the simplified models of new physics introduced in Chapter 4 on future searches for DM at DD experiments. At that time we referred to the neutrino scattering lines we ultimately derived as a type of "neutrino floor", but we have since decided to change our nomenclature, to avoid confusion with the original neutrino floor derived in Ref. [38]. Instead, "neutrino

---

[1]In reality this background is not entirely irreducible, but significantly reducing it will require radical changes to the design of DD experiments, for example the incorporation of directional detection.

contour" will be used to generically refer to our projections of neutrino physics onto the DM parameter space.

In Section 5.3, I present my work with D. Cerdeño, M. Cermeño, and M.A. Pérez García from Ref. [4], in which we recompute some of the constraints on scalar mediators introduced in Section 4.2.2. As we will see, these constraints have important consequences for our projections of new physics onto the canonical WIMP parameter space.

5.1   The CEνNS background in the SM

The rate of CEνNS in a DD experiment can be calculated using a master formula equivalent to that used for WIMP scattering in Equation (2.1.1),

$$\frac{dR_{\nu A}}{dE_R} = \frac{1}{m_A} \int_{E_\nu^{\min}} dE_\nu \frac{d\phi_\nu}{dE_\nu} \frac{d\sigma_{\nu A}}{dE_R}, \qquad (5.1.1)$$

where the cross section for CEνNS in the SM is given in Equation (4.1.1) and $d\phi_\nu/dE_\nu$ is the flux spectrum of neutrinos incident on the detector. As the neutrinos are relativistic, the velocity integral from Equation (2.1.1) is replaced with an integral over the neutrino energy, where $E_\nu^{\min} = \sqrt{m_A E_R/2}$ is the minimum neutrino energy required to generate a recoil energy E_R.

The dominant sources of neutrinos incident on DD experiments within the required energy range will be solar neutrinos, which we discussed in Chapter 3, and atmospheric neutrinos, which are generated from cosmic ray collisions in the upper atmosphere. An additional population exists as a result of the combined neutrino emission of past supernovae, the diffuse supernova neutrino background (DSNB), though its contribution to the CEνNS rate is subdominant compared with solar and atmospheric neutrinos. The associated flux spectra are shown in Figure 5.1. As an aside, there are statistical and systematic uncertainties of between 1 and 10% on these fluxes. These are important to the definition of the original neutrino floor, but
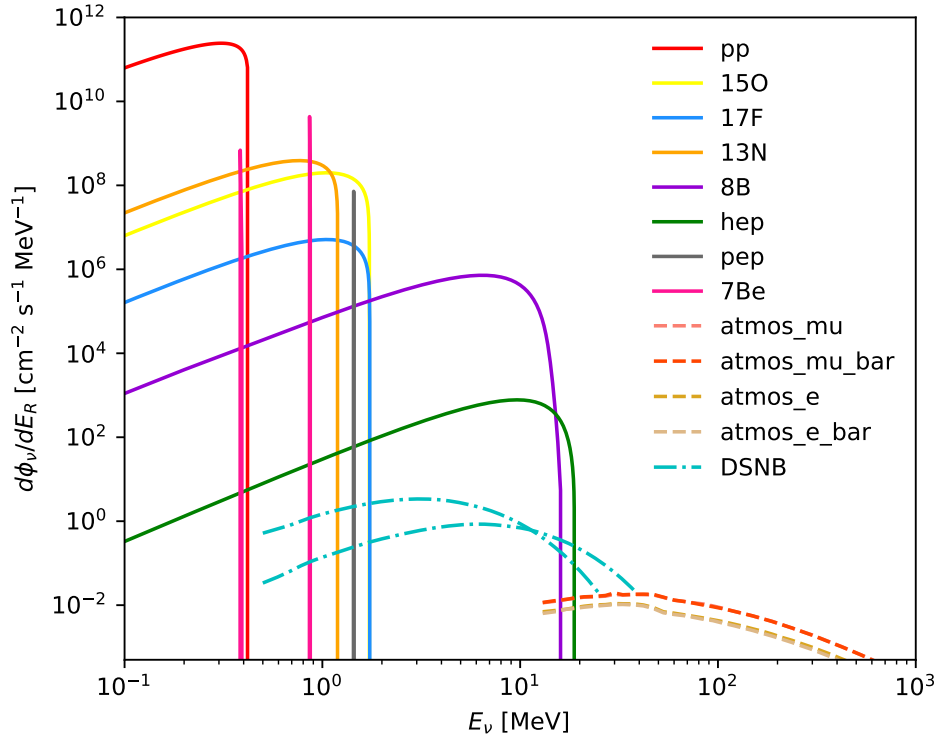
Figure 5.1: Average fluxes of solar and atmospheric neutrinos incident on a terrestrial detector. Solid lines indicate solar neutrinos, dashed lines are atmospheric neutrinos, and dot-dashed lines are the diffuse supernova neutrino background. Here we are assuming a high-metallicity Sun.

in our own work we will neglect them [115]. As we will show below, the effect of new physics can be much larger than such uncertainties.

In this work, we have neglected the effects of reactor neutrinos interacting within DD experiments. Every location on Earth is now subject to an overall flux of neutrinos produced in nuclear reactors around the world. However, the total magnitude of this flux can vary considerably with location [203]. In general, DD experiments are sited in laboratories where the reactor neutrino flux is smaller than the ^{8}B neutrino flux by at least an order of magnitude. Additionally, the maximum energy reached by reactor neutrinos is less than that of ^{8}B neutrinos, so the contribution to the CEνNS rate will be subdominant to that of solar neutrinos across all recoil energies [204].

From Figure 5.1, we see that the largest flux of neutrinos is that of the so-called pp

neutrinos, those that are produced in the first stage of the solar pp chain. However, the energy of these neutrinos is too small to produce detectable recoils via CEνNS in current DD experiments. Instead, the two most important fluxes for our purposes are the ^{8}B and atmospheric neutrinos. The spectrum of CEνNS induced by each flux population is shown in Figure 5.2. From this figure, we see that detectors with energy thresholds below ~ 10 keV will be sensitive to recoils from ^{8}B solar neutrinos, while for detectors with higher thresholds only atmospheric neutrinos will be detectable, with a much lower scattering rate.

In order to project the influence of CEνNS onto the canonical WIMP parameter space, we begin by following the process of Ref. [38], in which the floor was first introduced. Consider our simplified model of a DD experiment, introduced in Chapter 2. We noted that three parameters were required to define our simplified experiments: a target nucleus, a lower energy threshold, and an exposure. Choosing some target and energy threshold for the detector, we can calculate the total rate of CEνNS events per unit of exposure. We then fix the exposure so that 1 event of CEνNS is expected over the lifetime of the experiment.

In Ref. [2], we then calculated the minimum spin-independent WIMP-nucleon elastic cross section, $\sigma_{\chi N}^{SI}$, that could be excluded by an experiment with this energy threshold and exposure at the 90% confidence level (CL) for each value of the DM particle mass, m_χ. This is a good metric for comparing sensitivities between DD experiments, as it is typically among the first analyses performed for an experimental result showing no clear signal of DM. Performing a background free analysis and assuming that no events are seen in the detector, a 90% confidence limit can be placed on the WIMP parameter space along the isovalue contour where 2.3 events of DM scattering are expected. The contour could then be used to identify when a DD experiment should expect to see > 1 count of CEνNS, based on its sensitivity at the 90% CL. Here we used the cross sections and DM parameters introduced in Chapter 2.

However, since the publication of the above work we have reexamined this definition,
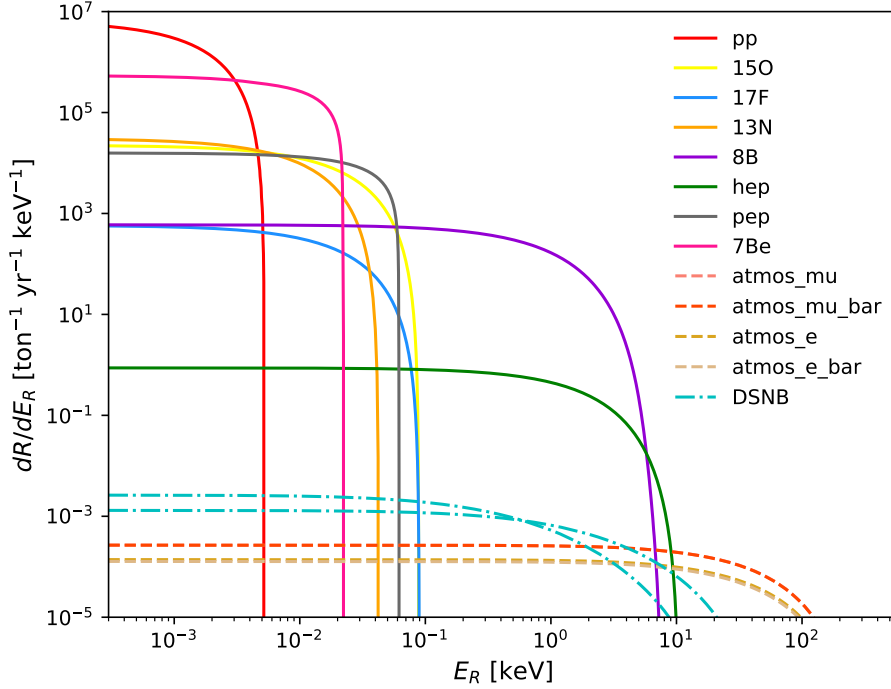
Figure 5.2: Differential rate of CEνNS induced by each flux population of neutrinos from Figure 5.1 scattering with germanium nuclei.

and decided to make a modification. Rather than computing a 2.3 isovalue contour on the WIMP parameter space, we will instead calculate the contour along which 1 event of coherent WIMP-nucleus scattering is expected. This new isovalue contour therefore represents the region of the WIMP parameter space where equal numbers of events are expected from both WIMP-nucleus scattering and CEνNS. The benefits of this updated definition will arise when considering the effects of new physics in Section 5.2. The updated contour can be obtained trivially from the lines presented in Ref. [2], by rescaling $\sigma_{\chi N}^{SI}$ by a factor $1/2.3$.

We perform this computation for a range of simplified DD experiments, varying the energy threshold across a wide range of values. We define our neutrino contour as the lower envelope of the resulting isovalue contours, as shown in Figure 5.3. In principle, an equivalent object can be defined for a generalised WIMP parameter space, like the one we discussed in Section 2.3 [205]. However, in this work we focus
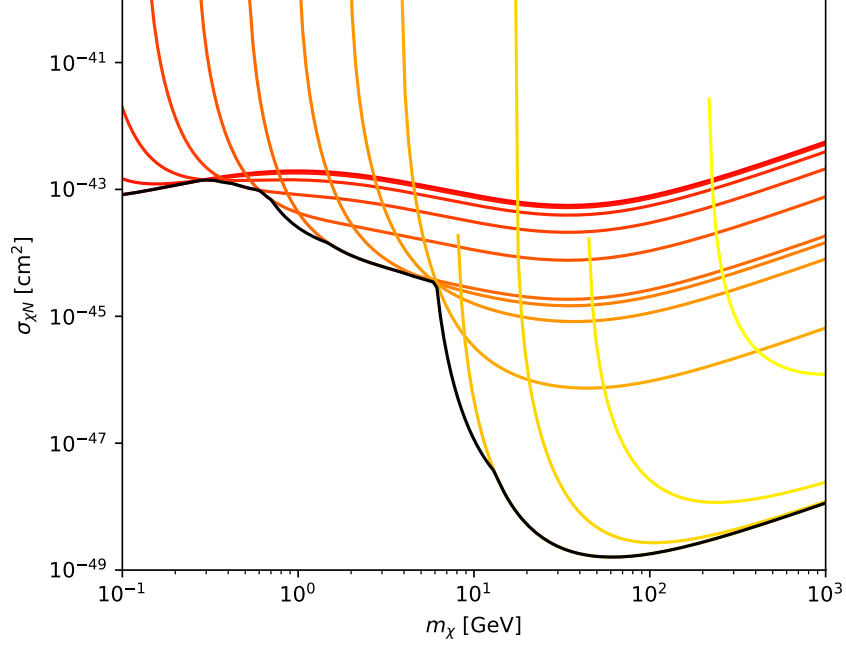
Figure 5.3: The neutrino contour (black) is constructed from the lower envelope of the isovalue contours along which an equal number of events are expected from WIMP-nucleus scattering and CEνNS, for a set of simplified DD experiments with varying energy thresholds.

on the simplest spin-independent parameter space.

In Figure 5.4 our neutrino contour is plotted for three targets: helium, germanium, and xenon, along with constraints and projected sensitivities from relevant DD experiments. Germanium and xenon were selected due to their prevalence in DD experiments, while helium was included to demonstrate the radical difference in the form of the contour for light target nuclei. The reasons for this difference, and for the shape of the neutrino contour in general, can be understood intuitively. The spectra for both DM scattering and CEνNS have an approximately exponential energy dependence, with the slope of the CEνNS spectrum approximately matching that of a 6 GeV WIMP for ^{8}B neutrinos, and a 100 GeV WIMP for atmospheric neutrinos. As we saw in Figure 2.1, WIMPs with higher masses will in general be able to induce higher-energy recoils than lighter WIMPs. For WIMPs with mass $m_\chi \gg 6$ GeV, a sufficiently high energy threshold will exclude the more abundant

solar neutrinos, leaving only the higher energy WIMP events and the much less abundant amospheric neutrino events. Lower mass WIMPs will not produce recoils with higher energies than those from ^{8}B neutrino scattering, and so will always be subject to this larger source of background. The neutrino contour is therefore lower for high-mass WIMPs than for low-masses, for the majority of target nuclei.

Helium, however, has a nuclear mass of only 3.7 GeV. The spectral shape for CEνNS and WIMP scattering with helium is therefore quite different from the xenon and germanium cases. Low mass WIMPs, and CEνNS scattering with ^{8}B neutrinos, can induce recoils with quite high energies, and the spectrum does not vary as dramatically with higher WIMP masses. A high energy threshold is therefore less effective for distinguishing high-mass WIMPs from ^{8}B neutrinos, and there is no characteristic drop-off in the neutrino contour above $m_\chi = 6$ GeV.

This neutrino contour is a useful tool for quickly identifying the importance of CEνNS in a given search for DM. Any DD experiment that wishes to search for WIMPs in the parameter space below this line will have to contend with an expected rate of background events from CEνNS at least equal to the number of signal events from DM, either in the resulting analysis or by utilising some additional technology such as directional detection.

In Ref. [38], these isovalue contours were used as the first step towards the derivation of the neutrino floor. As detectors begin to explore below the isovalue contour we defined, the ratio of potential DM signal events to background events from CEνNS will decrease linearly with $\sigma_{\chi N}$. In that work, the behaviour of the discovery potential (the minimum value of $\sigma_{\chi N}$ for which an experiment has a 90% probability of achieving a 3σ discovery) was explored as a function of experimental exposure. When backgrounds are negligible and a background-free analysis is possible, the discovery potential scales as $1/MT$. Below our neutrino contour, when the number of CEνNS events is greater than the number of WIMP events, the discovery potential instead scales as $1/\sqrt{MT}$. The marginal benefit of increasing the exposure of an experiment is therefore reduced. Finally, when the neutrino background is much
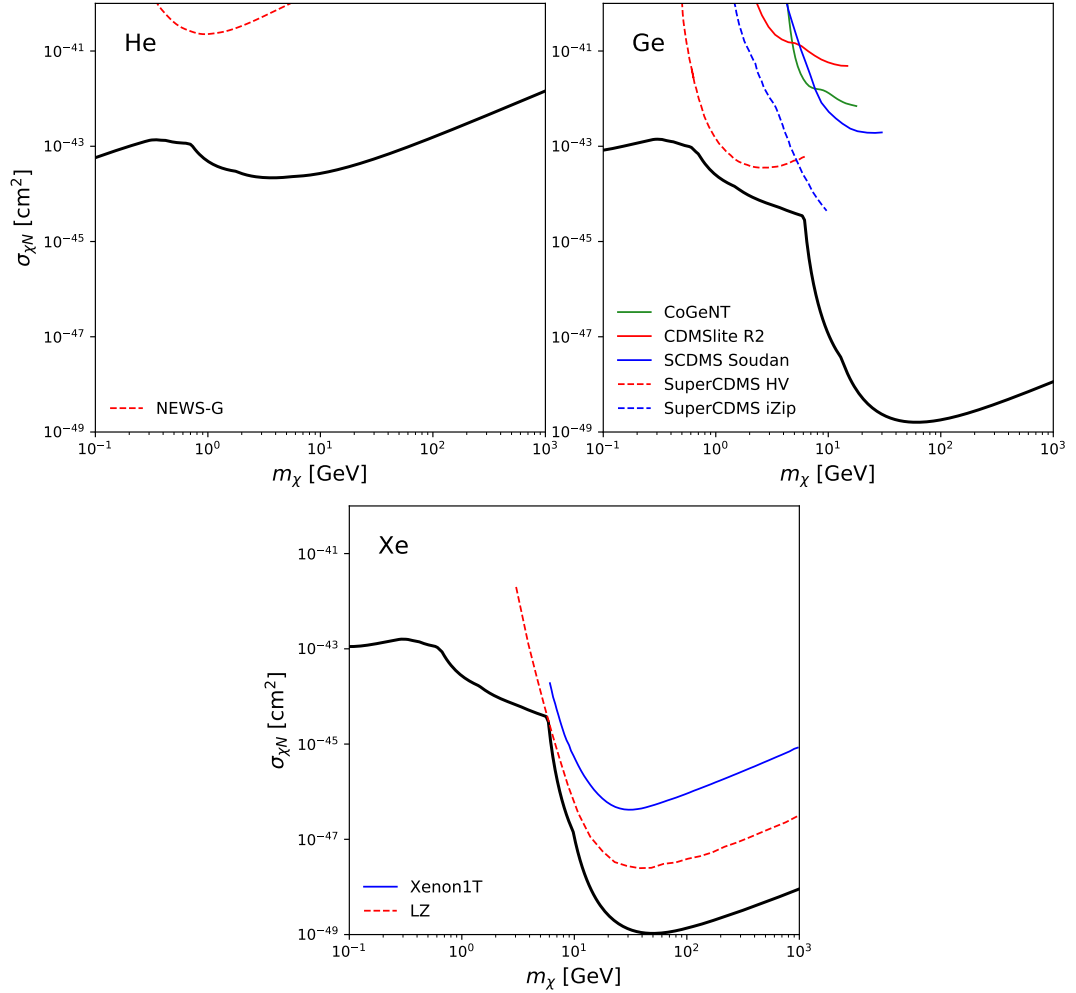
Figure 5.4: The neutrino contour (black) for three different target nuclei assuming SM neutrino physics: helium, germanium, and xenon. Along this contour, at least as many CEνNS events are expected to occur in a DD experiment as DM scattering events. Constraints and projected sensitivities of some relevant past (solid) and future (dashed) DD experiments are shown for comparison.

larger than the WIMP signal, the discovery potential scales even more slowly with exposure. The uncertainty on the neutrino flux makes perfect subtraction of the CEνNS background impossible, and WIMPs with sufficiently small cross sections are ultimately almost indistinguishable from the neutrino background. The neutrino floor is defined as the lower limit of the WIMP discovery potential for simplified DD experiments with very large exposures.

There are, however, a few strategies that can be employed to search for WIMPs below the discovery limit calculated in Ref. [38]. Firstly, spectral information can be used to distinguish the neutrino background from WIMPs of certain masses. Indeed, in the above reference a binned likelihood analysis is employed, so the discovery limit plotted is not a strict lower bound on cross sections that could be probed. There is, however, a "saturation region" of the parameter space for which an increase in exposure, even of an order of magnitude, provides very little improvement in the discovery potential of an experiment [206]. Additional methods have been considered to improve detector performance below the apparent discovery limit. For most conventional DD experiments, timing information can be utilised to improve the discovery potential at high exposures, as WIMPs and neutrinos each exhibit a different annual modulation effect [207]. Ultimately, directional DD experiments could provide a way to distinguish the two signals, using the expected spatial distributions of both WIMPs and neutrinos to largely negate the effects of the CEνNS background on WIMP searches [208].

The neutrino floor is frequently shown on plots comparing the sensitivities and bounds from different DD experiments [209, 210], indicating how much unconstrained parameter space remains before CEνNS becomes a hindrance to further searches. However, as the neutrino floor is effectively a way of projecting the physics of neutrino scattering onto the parameter space of dark matter, care should be taken when interpreting it. As with our neutrino contour, the neutrino floor is specific to the target nucleus for which it was derived. The most commonly used line is taken from Ref. [38], where the floor is plotted for a xenon target, but for experiments

utilising light targets the discovery limit can be quite different.

We were initially interested in studying the effects of new neutrino physics on the neutrino floor. However, until a specific model of new physics is confirmed and its properties well understood, we do not believe the neutrino floor to be the most useful tool for our purposes. The level of the neutrino floor is determined by the sizes of the uncertainties on the neutrino scattering rate. In the presence of one of our simplified models of new physics, the neutrino flux uncertainty is insignificant compared with the uncertainty on the mass, couplings, and even existence of additional particles which affect the CEνNS scattering rate. However, the concept of using a line on the WIMP parameter space as a tool for visualising the effects of neutrino physics is a powerful one.

In the next section, we will examine the effects of new physics on the neutrino contours shown in Figure 5.4, and show how this projection of neutrino physics onto the WIMP parameter space can be used to make predictions for future DD experiments.

5.2 Enhancing the CEνNS rate with new physics

The neutrino contours shown in Figure 5.4 have been derived under the assumption of SM neutrino interactions. In the presence of one of the new mediators discussed in Chapter 4, the CEνNS cross section is modified, and the neutrino isovalue contours will move. In this section, we will explore the largest possible increase to the level of the neutrino contour in each of our models of new physics, and discuss the significance of the resulting object. The section is based predominantly on my own contribution to Ref. [2], though I have included some additional and updated results, for example the computation of the neutrino contour for a $U(1)_{L_\mu - L_\tau}$ model and the LNC scalar, as they are relevant to the remainder of this work.

In order to calculate the maximum possible increase to the neutrino contour allowed in each of our models across the full range of m_χ, we consider a selection of points

in each parameter space across a range of masses, taking the maximum couplings allowed by the constraints discussed in Section 4.2. We then compute the CEνNS cross section and resulting neutrino contour with a mediator described by each of these points in a given parameter space, for each of the target nuclei in Figure 5.4. The raised neutrino contour is the maximum level of the contour allowed by each model, found by taking the upper envelope of the lines computed for each allowed point in the parameter space of the simplified model.

So, what is the physical significance of this object? It is not simply that it represents the point where equal numbers of CEνNS and DM events are expected under a particular model of new physics: if the presence of one of these mediators were confirmed, that contour could indeed be raised, but the object we are examining is the upper envelope across all possible modifications that could be induced under a given simplified model. The raised neutrino contour represents the maximum DM coupling at each mass m_χ for which an equal rate of CEνNS *could* be induced in a given model, based on current experimental constraints. An apparent signal of DM, consistent with a WIMP within the region between the SM neutrino contour and the raised neutrino contour, can therefore not be immediately assumed to be the result of DM scattering. Instead, the possibility must be considered that the additional events seen in the detector are the result of CEνNS, its cross section enhanced by the presence of new physics.

The contour also offers a way of quickly estimating the prospects of a DD experiment placing competitive limits on a given model of new physics in the neutrino sector, simply from its sensitivity to a canonical WIMP parameter space. A given WIMP candidate can only be constrained by a DD experiment if a sufficiently large DM event rate is expected, and not observed. If that candidate lies below the raised neutrino contour for a given model of new physics, then some unconstrained region of the parameter space for that model would produce a larger expected rate of CEνNS than that of the DM candidate being constrained. A DD experiment with the ability to constrain the WIMP parameter space below the raised neutrino contour therefore

has a reasonable possibility of placing an equivalent constraint on the corresponding model of new physics in the neutrino sector[1].

These claims cease to be valid as the level of the raised neutrino contour approaches that of the SM neutrino contour. Clearly, as the CEνNS rate becomes highly constrained, the vast majority of events from CEνNS will be due to scattering through the SM weak force, and large amounts of statistics will be necessary to further constrain these models. However, all of the models we consider still allow potential enhancements of the CEνNS rate of up to a factor ~ 2, so a sensitivity below the raised neutrino contour is still a reasonable motivation for performing a more detailed analysis of the model in question at that experiment.

The raised neutrino contours obtained in our two vector models are shown in Figure 5.5, along with the SM line for comparison. We see that in the presence of a $U(1)_{B-L}$ mediator, the level of the neutrino contour can be raised by up to a factor of 2, while a $U(1)_{L_\mu-L_\tau}$ mediator can lead to an increase of up to a factor of 3 in some cases. Of the DD experiments we are considering, only LZ will be sensitive to any parameter space below the raised neutrino contour for the $U(1)_{B-L}$ and $U(1)_{L_\mu-L_\tau}$ models. We will see in Chapter 7 that this supports our interpretation of the neutrino contour, as LZ is expected to set new limits on the $U(1)_{L_\mu-L_\tau}$ parameter space, while SuperCDMS SNOLAB is not.

In Figure 5.6, the raised contours are shown for the LNV and LNC scalars introduced in Section 4.2.2. However, the supernova constraints taken from Ref. [188] were either quite approximate, or dependent on the chosen model of supernova dynamics. At the time of writing Ref. [2], when we only considered an LNV scalar, we computed three separate lines. In the first (dotted lines in the LNV plots of Figure 5.6), we assumed that all the supernova constraints were valid and constraining. In this case, very little change to the neutrino scattering rate was allowed. In the second case

---

[1]Under the definition we used in Ref. [2], this is not true. There, a DD experiment setting constraints on the WIMP parameter space below the raised neutrino contour should expect to see > 1 event from CEνNS, but this is not necessarily sufficient to allow a constraint to be placed on the model of new neutrino physics being considered.
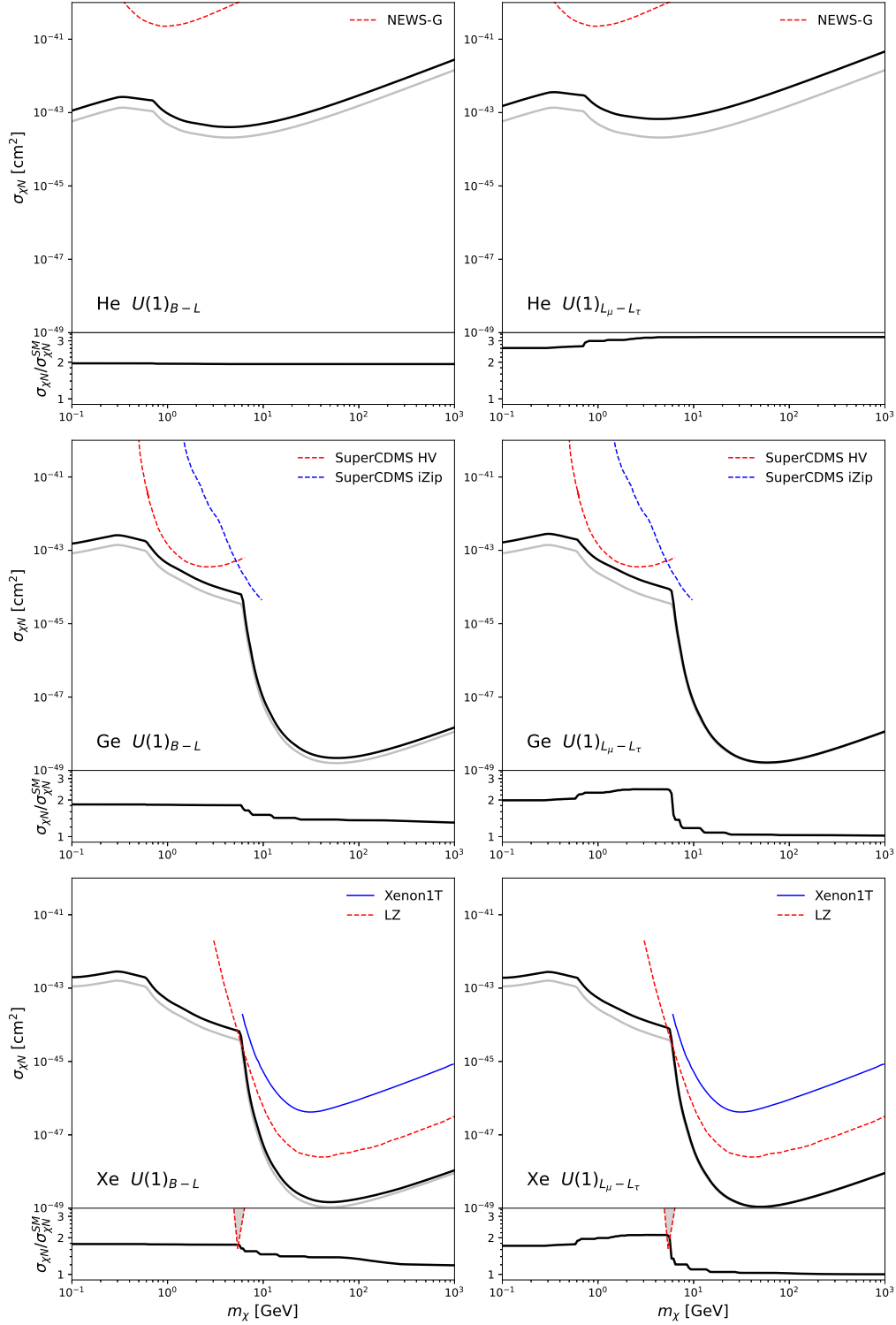
Figure 5.5: The raised neutrino contour: the maximum possible increase to the level of neutrino contour for each mass m_χ, under a $U(1)_{B-L}$ model (*left*) and a $U(1)_{L_\mu-L_\tau}$ model (*right*), for the three target nuclei used in Figure 5.4. In each case the solid black line represents the raised neutrino contour, and the grey line represents the SM neutrino contour. The relative increase compared with the SM result is shown in each case below the main plot.
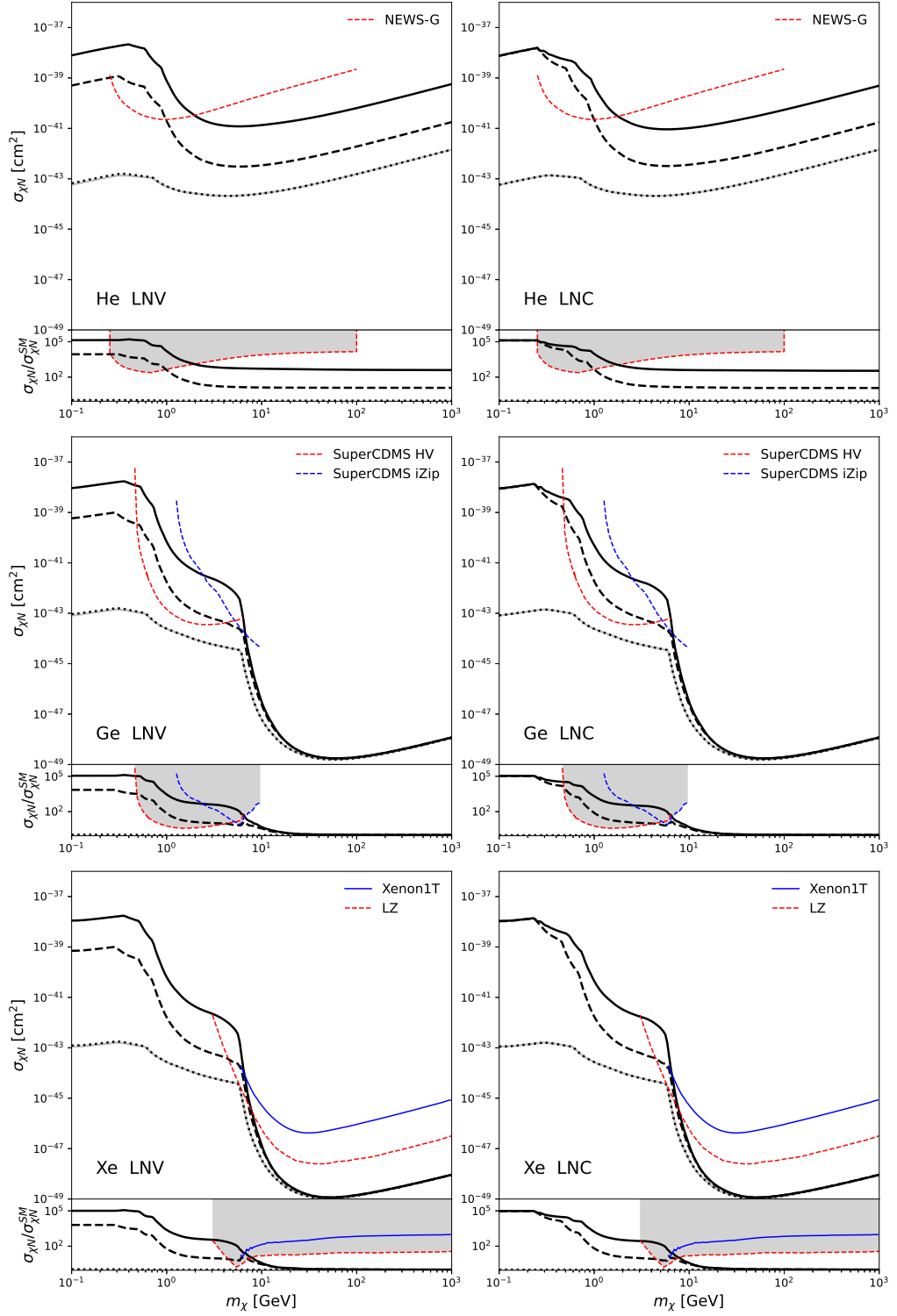
Figure 5.6: As in Figure 5.5, but for our two scalar models. Three scenarios are considered for each model, using different combinations of the possible constraints on the models. These different scenarios are discussed in detail in the main text.

(dashed lines), the model dependent constraints based on the supernova equation of state were disregarded, but the constraint from the neutrino diffusion time was included. In the final case (solid lines), all constraints from supernova physics were ignored. In this last case, we found that the allowed increase in the level of the neutrino contour was very large, with increases of several orders of magnitude for WIMPs with low masses.

For this work, I have also computed the neutrino contour for an LNC scalar. Again, three scenarios are considered. In the first case (solid lines), as for the LNV scalar, all supernova constraints are neglected. In the second (dashed lines), all supernova constraints are included, with the leading contributions to the raised neutrino contour coming from the narrow band of allowed parameter space between the neutrino diffusion constraint and the region excluded by the ν_R cooling constraint. Since all the supernova constraints have been calculated quite approximately, it is conceivable that in a more careful calculation this narrow band could be excluded, so we also consider the case where that band is ignored, and constraints are taken from the bottom of the region excluded by cooling constraints (dotted line). In this case we find very little deviation from the SM line.

The large increases allowed in the level of the neutrino contour in these scalar models are not entirely unexpected. In these models, we considered only constraints on the coupling $Y = \sqrt{y_\nu Y_N}$, since other constraints will only translate to bounds on CEνNS in a model-dependent way. This means that far fewer constraints exist on these models than on the $U(1)_{B-L}$ and $U(1)_{L_\mu - L_\tau}$ mediators we considered, where the relative couplings to all SM fermions are fixed. In particular, in the absence of constraints from electron scattering, the parameter space is not heavily constrained at low masses around 10 MeV. These mediators can generate huge increases to the CEνNS cross section at low energies, with very little effect at the higher energies to which COHERENT is sensitive. There is therefore a large region of the parameter space between the SM and raised neutrino contours to which experiments like SuperCDMS SNOLAB will be sensitive, indicating the potential

for them to set competitive limits on the presence of new light scalars.

However, this large increase to the neutrino contour is entirely dependent on our interpretation of the supernova constraints derived in Ref. [188]. Understanding these constraints is crucial in order to know whether the allowed increase to the neutrino contour is several orders of magnitude, or almost zero. In the next section, I will discuss my recent work [4] with D. Cerdeño, M. Cermeño, and M.A. Pérez García to determine the validity of these constraints, and ultimately recalculate them including some important effects which were not considered in earlier works.

5.3 Supernova constraints on light scalar mediators

When a star reaches the end of its life, its slowing rate of fusion can no longer exert sufficient radiation pressure to counteract its self-gravity, and the star begins to contract. As the temperature and pressure of the stellar core increase, heavier nuclei are formed and the binding energy released from their fusion briefly slows the collapse. The cycle of fusing heavier and heavier elements is a process of diminishing returns, and eventually the stellar core collapses into a white dwarf, a stellar remnant supported by electron degeneracy pressure. For stars with masses similar to our Sun, this is where the collapse will cease, leaving a white dwarf that gradually cools over billions of years. If the progenitor star has a mass $M > 8M_\odot$, however, the continued accretion of stellar material onto the nascent white dwarf pushes its mass towards the Chandrasekhar limit, beyond which electron degeneracy pressure cannot support the gravity of the core. In this case, the white dwarf collapses into an object of even greater density: a proto-neutron star. This final stage of collapse precipitates one of the most energetic phenomena in astrophysics: a Type-II supernova [197].

As we discussed in Chapter 4, neutrinos play a crucial role in the the dynamics of supernovae. Most of the gravitational binding energy of the star, approximately

3×10^{46} J, is radiated out of the core in the form of neutrinos. In the early stages, as the proto-neutron star begins to form, protons undergo electron capture, releasing large numbers of electron neutrinos in the process. The first neutrinos free-stream out of the core, carrying away a portion of the total lepton number of the star. As the core continues to contract, however, its density increases and the inner core becomes opaque to the outflowing neutrinos, trapping them.

The trapped neutrinos quickly become degenerate as the phase space volume available to them is filled. This leads to a significant neutrino chemical potential, μ_ν, slowing the rate of processes that generate more electron neutrinos. In addition to electron capture, trapped neutrinos scatter with neutrons, converting them back into electrons and protons. As a result, the fraction of electrons within the core tends towards an equilibrium due to the forward and backward reactions,

$$p + e^- \rightarrow n + \nu_e \,,$$

$$n + \nu_e \rightarrow p + e^- \,. \tag{5.3.1}$$

This slows the conversion of the proto-neutron star into pure neutron-degenerate matter and most current models predict that a significant fraction of the electrons are present in the core during the next, crucial stage of the supernova [211, 212].

Until this point, the progress of the supernova has been characterised by contraction and collapse, as the immense forces of gravity compress the core of the star into increasingly dense states of matter. However, supernovae are best known not for this collapse, but for the immense and violent explosion which follows it. The explosion is understood to be the result of a shockwave generated within the inner layers of the collapsing star which propagates outwards, halting the collapse and expelling the outer layers into the cosmos. The exact mechanism for producing the shockwave is not known [213].

Early models of supernovae explained the shock as the result of a "bounce". In this scenario, the bounce occurs when the in-falling stellar core encounters the extreme counteracting force of neutron degeneracy pressure. The core immediately

becomes rigid enough to halt the gravitational collapse[1], and the sudden deceleration generates a powerful shockwave within the core [216]. In this scenario, known as the prompt shock scenario, the lepton fraction is an important quantity, as the presence of electrons strengthens the core and reduces energy losses due to nuclear dissociation [199]. This is the origin of the "SN equation of state" constraint in Ref. [188], as the presence of LNV interactions could lead to the deleptonisation of the core. However, as we stated in Section 4.2.2, simulations utilising this mechanism result in failed supernovae, as the shockwave stalls within the first few hundred kilometres of its propagation and the star collapses inwards without exploding [200]. This outcome has been shown to have little sensitivity to variations in the lepton fraction of the core [217].

In order to revive the stalled explosion, additional energy must be imparted into it from the supernova core. As neutrinos are known to carry a large fraction of the supernova energy, they were quickly identified as a mechanism for transporting the energy required to restart the explosion [218]. This is known as the delayed shock scenario, as the shockwave is allowed to stall before being reignited by the injection of additional energy from outflowing neutrinos. The delayed shock scenario is much more successful in reproducing the observed properties of supernovae, although significant uncertainties remain regarding the exact mechanism through which energy is transferred from neutrinos into the stalled shockwave [219].

Following the hypothesised bounce and subsequent shock propagation, the proto-neutron star enters a Kelvin-Helmholtz cooling phase. During this phase it radiates off much of its gravitational binding energy in the form of neutrinos and antineutrinos of all flavours. The supernova core is still dense enough to prevent radiated neutrinos free-streaming, so they diffuse out of the core over a timescale determined by their mean free path. The diffusion timescale is subject to constraints from the observation of the neutrino burst associated with SN1987A, as it must be consistent with the

---

[1]Either permanently, leading to the formation of a neutron star, or temporarily, if the remnant's mass exceeds the Tolman-Oppenheimer-Volkoff limit and a black hole is formed [214, 215].

spectrum of neutrino emission detected in Kamiokande-II [124], IMB [125], and BUST [126]. The approximate value of the diffusion time determined from that measurement is [220]

$$t_E = \frac{3R_{\mathrm{ns}}^2}{\pi^2 \lambda_0} \frac{E_{\mathrm{th}}^0}{2E_\nu^0} \sim 10\,\mathrm{s}\,, \tag{5.3.2}$$

with R_{ns} the radius of the proto-neutron star, E_{th}^0 the initial thermal energy, E_ν^0 the initial neutrino energy, and λ_0 the mean free path. The dominant scattering process at this stage in the supernova evolution is neutrino-nucleon scattering, and so it plays an important role in computing the mean free path. This is the origin of the supernova diffusion constraint discussed in Section 4.2.2.

Finally, the supernova energy loss constraints discussed in Section 4.2.2 are also derived from the SN1987A measurements. The majority of the neutrinos detected were electron antineutrinos, and from the combined neutrino energy and distance to the source (in the Large Magellanic Cloud), the total energy released in electron antineutrinos was calculated to be $E_{\bar{\nu}_e}^{\mathrm{tot}} \approx 5 \times 10^{45}$ J [221]. From this, the Raffelt criterion on the allowed luminosity of additional particle species was derived [197], leading to the constraint on an LNC scalar due to ν_R emission in Ref. [188]. However, as we will discuss in the next section, the constraint derived on ν_R production is not related to this Raffelt criterion, but rather to the apparent disappearance of the neutrino burst which would occur if a sufficiently large proportion of active neutrinos were converted to their sterile chirality states.

In Section 4.2.2, we summarised the approximate methods used in Ref. [188] to derive constraints on LNV and LNC scalar models using arguments from supernovae. All three arguments used in that work: the neutrino diffusion time, ν_R production, and the equation of state (EoS); in some way rely on the cross section for neutrinos scattering with nucleons within the supernova core. However, Ref. [188] effectively used the vacuum scattering cross section, which fails to take into account the density of the surrounding medium. As the core of a supernova is among the densest environments in the known universe, this approximation requires further study. In our ongoing work, we have attempted to recompute the supernova constraints on

the two scalar models using the full in-medium cross section required for an analysis in the supernova core.

5.3.1 Neutrino-nucleon scattering in a dense medium

When free particles scatter in a low-density environment, the outgoing phase space is generally considered to include all final states that are kinematically allowed. In an environment with finite temperature and pressure, however, the phase space can be far more restricted and we must consider the distribution of available final states when computing the cross section. The differential cross section for the scattering of (anti-)neutrinos and nucleons can be written as [222]

$$d\sigma = \frac{|\overline{\mathcal{M}}|^2}{4\sqrt{(p \cdot k)^2 - m_N^{*2} m_\nu^2}} d\Phi(p, p', k, k')(1 - f_N(E_N'))(1 - f_\nu(E_\nu')), \qquad (5.3.3)$$

where $|\overline{\mathcal{M}}|^2$ is the squared matrix element for the scattering process, and the phase space volume element is

$$d\Phi(p, p', k, k') = (2\pi)^4 \delta^{(4)}(p + k - p' - k') \frac{d^3\vec{p}'}{(2\pi)^3 2E_N'} \frac{d^3\vec{k}'}{(2\pi)^3 2E_\nu'} \ . \qquad (5.3.4)$$

Here m_N^* is the effective mass of the nucleon in the medium, and p^μ and k^μ are the incoming 4-momenta of the nucleon and the neutrino, respectively, with primed variables representing the equivalent quantity for the outgoing particles. The Fermi-Dirac distribution, $f_i(E_i') = \left(1 + e^{(E_i - \mu_i)/T}\right)^{-1}$, describes the occupancy of the available phase space for particle i, with T the temperature of the medium and μ_i the chemical potential. The factor $(1 - f_i(E_i'))$ therefore describes the distribution of available, unoccupied states.

As with the vacuum neutrino scattering cross sections in Chapter 4, the squared matrix element can be decomposed into SM and new physics (NP) contributions,

$$|\overline{\mathcal{M}}|^2 = |\overline{\mathcal{M}}|_{\text{SM}}^2 + |\overline{\mathcal{M}}|_{\text{NP}}^2. \qquad (5.3.5)$$

The squared matrix element for the SM interaction can be found in the literature,

for example in Ref. [223], and the new physics contribution is the same in our two scalar models,

$$|\overline{\mathcal{M}}|^2_{\mathrm{NP}} = \frac{-y_\nu^2 Y_N^2}{(q^2 - m_\phi^2)^2} q^2 (4m_N^{*2} - q^2),$$

(5.3.6)

with $q^\mu = (q_0, \vec{q})$ the 4-momentum transferred from the neutrino to the nucleon.

The mean free path is defined as $\lambda = V/\sigma$, with σ the cross section, and V the phase space volume of the incoming nucleons. Following the procedure of Ref. [222], we find

$$\lambda^{-1} = \frac{\sigma}{V} = \frac{1}{8(2\pi)^4} \int_{-\infty}^{E_\nu} dq_0 \int_{|q_0|}^{2E_\nu - q_0} d|\vec{q}| \int_0^{2\pi} d\phi_{13} \int_{|\vec{p}_-|}^\infty d|\vec{p}|$$

$$|\vec{p}| \frac{|\overline{\mathcal{M}}|^2}{E_\nu(E_N E_\nu - |\vec{p}| E_\nu \cos\theta_{12})} f_N(E_N)(1 - f_N(E_N'))(1 - f_\nu(E_\nu')),$$

(5.3.7)

with θ_{12} the angle between the incoming neutrino and nucleon, and ϕ_{13} the azimuthal angle between the incoming and outgoing neutrino. The lower limit on the nucleon momentum integral is $|\vec{p}_-| = \sqrt{E_{N-}^2 - m_N^{*2}}$, with $E_{N-} = \frac{-q_0}{2} + \frac{|\vec{q}|}{2}\sqrt{1 - \frac{4m_N^{*2}}{q^2}}$. Note that although the transferred energy integral has a lower limit of $-\infty$, this is weighted by the Fermi-Dirac distribution of available nucleons with energy $E_N > E_{N-}$.

The temperature, chemical potentials, and effective masses of the particles will change as the supernova contracts and as the neutrinos progress further out from the core. To account for these variations we divide the proto-neutron star into spherical shells, which we assume to have uniform temperature and density. Values for the temperature T, baryonic density n_i, and electron fraction Y_e were taken from Refs. [224, 225]. As well as spatially discretising the supernova, we consider two time snapshots, at 1 s and 5 s post-bounce. We also vary the radii of the shells in time as the core contracts and cools. In each case, the largest radius considered roughly corresponds to the edge of the neutrinosphere, which is the last scattering surface of most neutrinos before they free-stream out of the supernova [226]. Our analysis could be refined by allowing the conditions to vary smoothly in both time and space. However, such an analysis would require us to perform a full, hydrodynamic simulation of the supernova which is beyond the scope of this work.

In the presence of an LNV scalar with sufficiently large couplings, LNV interactions lead to mass conversion between neutrino and antineutrino states in the early stages of the supernova. This could prevent a degenerate density of trapped electron neutrinos from accumulating, reducing the neutrino chemical potential in the proto-neutron star core. If the conversion is efficient enough, the neutrino chemical potential will be reduced to zero. This greatly reduces the average energy of the neutrinos produced in the supernova, which for a thermalised neutrino is given by $\mu_\nu + \pi T$ [227]. In this scenario, the deleptonisation of the core is no longer impeded by the density of trapped neutrinos, and the electron fraction predicted in Refs. [224, 225] will disappear. This is the origin of the SN conditions in Table 5.2. We will discuss the requirements for this significant change in the supernova equation of state when we introduce the "supernova EoS" line in more detail, below.

The chemical potentials and effective masses were computed for an $18\,M_\odot$ progenitor using the TM1 model for the supernova equation of state [228]. I was not involved in this calculation, and so I will not go into detail on how it was performed. The resulting values are displayed in Tables 5.1 and 5.2. In those tables, the chemical potentials and effective masses of neutrons are shown, though we also computed the values for protons. When performing our calculations, we summed over the relevant contributions to the scattering rate from each species of nucleon.

Using these values, we computed the neutrino mean free path by numerically integrating Equation (5.3.7) for each radial shell and time-snapshot of the supernova. The resulting SM mean free path, λ^{SM}, is shown in Tables 5.1 and 5.2. We find that the inclusion of matter effects leads to significantly lower neutrino cross sections in the regions with a large chemical potential compared with the vacuum cross section used in both Ref. [188] and the more recent update in Ref. [229].

Lepton number conserved

$t \sim 1$ s	T (MeV)	$n(\mathrm{fm}^{-3})$	Y_e	μ_n(MeV)	μ_{ν_e}(MeV)	$m_n^\star$(MeV)	λ^{SM}(m)
$R = [0, 5]$ km	15	0.5	0.3	496.6	114.6	249.6	0.30
$R = [5, 7.5]$ km	20	0.3	0.28	530.0	102.7	384.9	0.22
$R = [7.5, 10]$ km	28	0.15	0.25	656.5	79.9	599.4	0.20
$R = [10, 15]$ km	33	0.06	0.2	779.8	29.0	786.0	0.49
$R = [15, 17.5]$ km	18	0.03	0.1	858.7	14.4	857.0	2.9
$R = [17.5, 20]$ km	7	0.008	0.05	917.2	12.5	915.9	36
$t \sim 5$ s	T (MeV)	$n(\mathrm{fm}^{-3})$	Y_e	μ_n(MeV)	μ_{ν_e}(MeV)	$m_n^\star$(MeV)	λ^{SM}(m)
$R = [0, 5]$ km	25	0.5	0.25	504.3	41.8	254.6	0.38
$R = [5, 7.5]$ km	28	0.4	0.23	509.4	36.1	309.1	0.50
$R = [7.5, 10]$ km	32	0.3	0.2	537.7	24.4	394.4	0.28
$R = [10, 12.5]$ km	25	0.15	0.13	664.8	14.2	599.1	0.63
$R = [12.5, 15]$ km	10	0.05	0.035	831.9	0	805.3	13

Table 5.1: Values of μ_n, μ_{ν_e}, $m_n^\star$, the baryon density, n, and temperature, T, of the supernova core at a range of radii and at three snapshots in time post-bounce. Also shown is the antineutrino mean free path in the SM, λ^{SM}. Temperatures, densities and lepton fraction taken from [225].

Lepton number violated

$t \sim 1$ s	T (MeV)	$n(\mathrm{fm}^{-3})$	Y_e	μ_n(MeV)	μ_{ν_e}(MeV)	$m_n^\star$(MeV)	λ^{SM}(m)
$R = [0, 5]$ km	15	0.5	—	512.3	-	253.9	3.1
$R = [5, 7.5]$ km	20	0.3	—	544.4	-	389.7	1.3
$R = [7.5, 10]$ km	28	0.15	—	538.0	-	383.0	0.51
$R = [10, 15]$ km	33	0.06	—	781.9	-	786.1	0.69
$R = [15, 17.5]$ km	18	0.03	—	859.2	-	857.0	4.1
$R = [17.5, 20]$ km	7	0.008	—	917.4	-	915.9	76
$t \sim 5$ s	T (MeV)	$n(\mathrm{fm}^{-3})$	Y_e	μ_n(MeV)	μ_{ν_e}(MeV)	$m_n^\star$(MeV)	λ^{SM}(m)
$R = [0, 5]$ km	25	0.5	—	509.9	-	256.2	0.71
$R = [5, 7.5]$ km	28	0.4	—	514.3	-	310.8	0.52
$R = [7.5, 10]$ km	32	0.3	—	541.0	-	395.4	0.36
$R = [10, 12.5]$ km	25	0.15	—	665.9	-	599.3	0.77
$R = [12.5, 15]$ km	10	0.05	—	831.9	-	805.3	4.1

Table 5.2: The same as Table 5.1 but assuming significant lepton number violation, leading to the disappearance of the electron fraction, Y_e, and the neutrino chemical potential, μ_{ν_e}.

5.3.2   Updated constraints on new physics from supernovae

In Section 4.2.2 we introduced the three arguments used to place constraints on light scalar mediators from supernova physics in Ref. [188]. We will now revisit each of these arguments in turn, and describe how we have updated them to provide a more reliable set of constraints on the relevant parameter spaces. Note that since the

majority of the events detected from SN1987A were attributed electron antineutrinos [124], we will perform all of our calculations using the electron antineutrino cross sections, which differ slightly from the electron neutrino cross sections in the dense medium of the supernova core. In reality, the observed electron antineutrino flux will depend in part on the scattering cross sections of other antineutrino flavours, due to neutrino oscillations. Here, we neglect these effects. Note that if we were to include oscillatory effects, we would not observe an MSW resonance in the $\bar{\nu}_e$ spectrum, as for antineutrinos the SM matter potential is negative [129]. Additionally, we will only consider scattering between neutrinos and nucleons. These are expected to be the most frequent scattering processes, with the possible exception of neutrino-neutrino scattering. It has been shown that neutrino-neutrino scattering does not affect the overall rate of neutrino diffusion [230], although it could affect our limits for the supernova EoS and ν_R production. If so, the effect would be to lower those limits somewhat, although the exact magnitude of the shift will be model-dependent as it depends on y_ν rather than $\sqrt{y_\nu Y_N}$.

- **Supernova EoS:** Whenever a neutrino scatters via the exchange of an LNV scalar it will be converted into an outgoing antineutrino. As we have already discussed, if these interactions occur in large numbers in the SN core, the resulting loss of lepton number has the potential to accelerate the conversion of the core into near-pure neutron degenerate matter. While such a conversion would conflict with some early models of supernova dynamics, for modern delayed shock models it is less significant [217], and so we do not consider this to be a constraint on our LNV scalar model.

  The loss of the electron fraction has important consequences for the equation of state of the supernova, however. In the absence of a degenerate density of neutrinos in the inner core, the neutrino chemical potential will vanish, and the mean free path of the neutrino can be quite different. It is therefore important for us to understand when this transition takes place.

Ultimately, we cannot know the exact extent and timing of the loss of the electron fraction and the neutrino chemical potential in a model with LNV interactions without performing a full hydrodynamic simulation, however we can make predictions in some simplified scenarios. In the case where each neutrino is expected to undergo at least one LNV interaction during its time in the neutrino trapping region, it is reasonable to believe that there will be an effect on Y_e. We therefore define an effective mean free path between new-physics interactions, λ^{NP}. This is computed in the same way as λ, using Equation (5.3.7), but without including the SM term in $|\mathcal{M}|^2$. When the distance traversed is equal to λ^{NP} we expect each neutrino to have undergone an average of one transition between a neutrino and antineutrino state.

Naturally, if only one LNV interaction is expected per neutrino over its entire path out of the supernova, the electron fraction is unlikely to drop to zero immediately after the bounce. A large density of neutrinos may therefore still accumulate. As this work is ongoing, we are still considering the best choice of condition for the SN EoS line. For now we will set the limit when $\lambda^{\mathrm{NP}} = t_E$, with t_E the time taken to escape the supernova core. Since only one new physics interaction is expected along this contour in the parameter space, the overall mean free path, and thus the diffusion time, will not be significantly altered from its SM value, so we will make the approximation $t_E \approx t_E^{\mathrm{SM}}$ when computing this line.

- **ν_R production and trapping:** A constraint on the LNC scalar is derived using a very similar method to the EoS line for an LNV scalar. Every time a neutrino scatters via the exchange of an LNC scalar, its chirality is flipped, leading to the production of a right-handed neutrino. As they do not interact via the weak force, right-handed neutrinos will free-stream out of the core unless the new LNC interactions are frequent enough to trap them. Taking the same criterion as the EoS constraint, $\lambda^{\mathrm{NP}} = t_E$, the majority of the left-handed neutrinos (and importantly, right-handed antineutrinos) will be

converted to the opposite chirality state and escape the core. Once outside the supernova, they would continue to propagate through space, the vast majority never encountering another environment of sufficient density to trigger a conversion back into left-handed neutrinos or right-handed antineutrinos. Had the neutrino burst associated with SN1987A been composed of nearly-sterile neutrinos[1] it would not have been detected, and the energy inferred to be carried by $\bar{\nu}_{L,e}$ could not have been as large as it was. We therefore place a constraint on the LNC scalar parameter space when $\lambda^{\mathrm{NP}} = t_E$. Clearly, this constraint is dependent on our earlier assumption that the right-handed neutrino is light enough to be produced in the supernova.

If, however, λ^{NP} is much shorter than the *free-streaming* distance out of the star, we can expect most of the neutrinos to be converted back into their active chirality states before escaping. In this case many interactions will occur via the exchange of an LNC scalar as the neutrinos propagate outwards, with half of the neutrinos emerging in their sterile state and half in their active state. This would reduce the active neutrino flux by half, however based on the single observation of SN1987A it does not seem that the overall neutrino luminosity can be constrained with a precision of 50%. We therefore set the upper bound on the region excluded by this ν_R condition to $\lambda^{\mathrm{NP}} < R/100$, with R the radius of the supernova.

- **Supernova neutrino diffusion:** Finally, we can obtain constraints on either an LNC or an LNV scalar using arguments from the neutrino diffusion time, t_E. As we have already discussed, the neutrino burst observed from SN1987A was consistent with a diffusion time $t_E \sim 10\,\mathrm{s}$. If new physics interactions reduce the mean free path, the neutrinos could be trapped for significantly longer than this, leading to a disagreement with the observed spectrum.

  To compute t_E we model the path of the (anti)neutrinos out of the supernova

---

[1]We call these right-handed neutrinos and left-handed antineutrinos "nearly sterile", as they clearly interact via the exchange of our new scalar, and so are not truly sterile.

using a random walk, with their direction chosen at random after every scattering event. This is not necessarily true, but properly accounting for the angular dependence of the cross section would likely require a Monte Carlo simulation, which would be very computationally intensive to perform at every point in our parameter space.

The mean squared displacement (MSD) of a particle undergoing a 3D random walk with mean free path λ after making n steps is

$$\langle r^2 \rangle = \lambda^2 n. \tag{5.3.8}$$

Since we assume that our neutrinos are travelling with speed $c = 1$, the time for them to reach an MSD R^2 from the centre of the supernova starting point is given by [231]

$$t = \frac{R^2}{\lambda}. \tag{5.3.9}$$

In fact, the MSD is not the best measure of the time taken for our neutrinos to escape the core. As neutrinos at large displacements are weighted more heavily than those at small displacements, when the MSD matches the radius of the neutrinosphere, R, a majority of the neutrinos will remain inside the diffusion region. A better measure is the hitting time, the average time taken for a neutrino to first cross the boundary of the neutrinosphere, since at this point it is expected to free-stream and escape the star. However, computing the hitting time in our system presents an even greater challenge than computing the mean squared displacement [232]. Given that we are already making many approximations, for example assuming that the neutrinos follow a random walk, such an analysis seems beyond the scope of our work.

In our example we have divided the supernova into concentric spherical shells. In each of these K shells the neutrino has a different mean free path, λ_k. The problem of calculating the mean square displacement in a random walk with a variable mean free path is a challenging one, and we have not yet settled

on a perfect solution. As an interim measure, we take the equation quoted in Ref. [229], correcting it with an additional factor of 2 so that it successfully reproduces the simplest case of a single sphere with constant λ,

$$t_E = 2 \int_0^R dr \frac{r}{\lambda(r)}. \qquad (5.3.10)$$

In our approximation, where $\lambda(r)$ is constant within each spherical shell, this integral can be replaced with a discrete sum,

$$t_E = \sum_{k=1}^K \frac{R_k^2 - R_{k-1}^2}{\lambda_k}, \qquad (5.3.11)$$

where R_k is the outer radius of the kth spherical shell and $R_0 = 0$. Comparing this with a Monte Carlo simulation in a few test scenarios, we find that the two agree within $\sim 20\%$ for most cases with six or fewer spherical shells, as we have here.

What is the value of the mean free path that we should use in each of our scalar models? For the LNC model, in the region of the parameter space where we place the diffusion constraint we expect many chirality-flipping interactions to occur as the neutrinos propagate out from the core. We therefore expect the diffusing neutrinos to spend approximately half their time in each of the chirality states. As each chirality state has a different mean free path, we take the average of the two,

$$\lambda_{\text{LNC}} = \frac{1}{2}\left(\lambda + \lambda^{\text{NP}}\right). \qquad (5.3.12)$$

In the LNV case the supernova diffusion constraint lies well above the supernova EoS line discussed above. It is therefore likely that the resulting LNV interactions will prevent the formation of a large neutrino chemical potential and deplete the electron fraction of the core. For this reason we take the values of the chemical potentials and effective masses from Table 5.2 when calculating the diffusion time constraint on an LNV scalar.

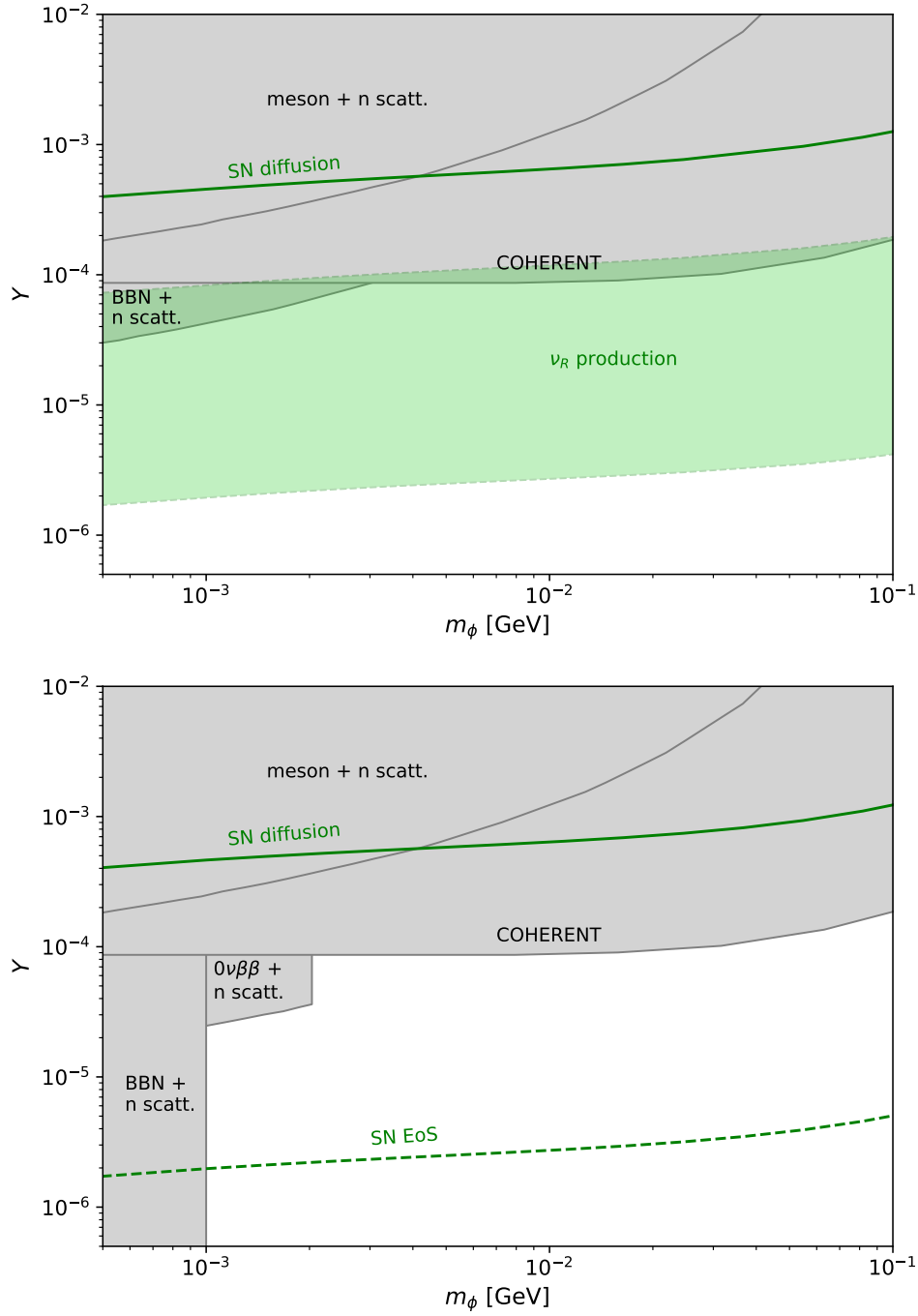Our supernova diffusion constraint will therefore be different for the two scalar

Figure 5.7: Updated constraints on the parameter space of an LNC (*top*) and LNV (*bottom*) scalar. Note that in the LNV case, the supernova EoS line should not be considered a constraint, but represents the limit above which LNV interactions could cause a significant change in the equation of state of the supernova.

mediators. This is in contrast to earlier works, where the diffusion constraint was found to be equal for both and LNC and LNV scalar, as they did not account for matter effects [188, 229].

Finally, we must decide which time-snapshot to use when computing the mean free path for each line. Unfortunately, the method we are using to compute the constraints cannot accommodate any time variation in the supernova conditions. Instead, we will attempt to choose the time value closest to half the time we expect the neutrinos to spend inside the supernova. This will provide a very approximate measure of the average conditions the neutrinos will experience, although we are severely constrained by the limited set of times for which data on the conditions were available [225]. In the case of the supernova diffusion constraints, this time is clearly 5 s, as we place our constraint when $t_E = 10$ s. For the other constraints, we expect the diffusion time to be closer to the SM diffusion time. In order to choose the most correct time snapshot possible, we performed an iterative process, computing the SM diffusion times using the $t = 5$ s values from Table 5.1, then choosing the time snapshot closest to half of that diffusion time and recomputing t_E^{SM}. This process yields a SM diffusion time of $t_E^{\mathrm{SM}} \approx 2.3$ s, so we take our values from the 1 s snapshot when computing the supernova EoS and ν_R production lines.

Our preliminary results are shown in Figure 5.7. We are still making many simplifications that are necessary when performing such an analysis without building a full numerical simulation of the supernova. However, we have made several improvements over previous analyses, most significantly by including the effects of density and temperature in our computation of the neutrino-nucleon scattering cross sections. Including these effects has led to a suppression of the cross section in the region where significant neutrino trapping is expected. The limits we obtain are therefore weaker than those derived in previous works. As such, our results represent a more conservative and reliable set of constraints on the parameter spaces of new scalars with masses in the MeV - GeV range.

As a result of our work, supernova constraints are no longer competitive with those of COHERENT in the LNV case, although there is a considerable region of the allowed parameter space in which we expect LNV interactions to affect the supernova equation of state. A more thorough investigation of these effects may be warranted, e.g. by performing a full hydrodynamic simulation to explore the impact of the loss of lepton number conservation on the evolution of the supernova.

In the LNC case, although all the constraints have been weakened, the maximum allowed coupling is considerably smaller than was previously expected. This is because the narrow band of parameter space allowed by previous constraints, above the band excluded by ν_R production but below the constraint from supernova diffusion, is now excluded by particle physics constraints. This means that whilst a very large increase to the level of the neutrino contour is allowed in the LNV case (equal to the solid black lines in Figure 5.6), in the LNC case there is very little increase allowed over the SM contour. We therefore predict that future DD will experiments have more success placing competitive constraints on the parameter space of the LNV scalar than on that of the LNC scalar.

We believe that the neutrino contour as we have defined it here can be a useful tool for estimating the ability of DD experiments to set competitive constraints on models of new physics which affect the rate of CEνNS. Ultimately, however, the only way to compute a constraint on these models is to perform a careful analysis specific to an individual DD experiment. In the remainder of this work, we will explore how constraints on simplified models of new physics can be derived from DD experiments. The results of the next two chapters will allow us to test some of the assumptions we made when deriving the neutrino contours, and ultimately examine whether the predictions we made based on Figure 5.5 are accurate.

Chapter 6

Constraining new physics with CDMSlite

In addition to generic analyses of DD experiments like those described in Chapters 2 and 5, I have worked with individual experimental collaborations, most extensively the SuperCDMS collaboration, to derive constraints on the simplified models introduced in Chapter 4. These models are currently of interest due to the large improvements in sensitivity anticipated from SuperCDMS SNOLAB, the next iteration of the long-running SuperCDMS experiment.

In Figure 5.5, SuperCDMS SNOLAB does not appear to have any sensitivity to physics below the raised neutrino contour, for either the $U(1)_{B-L}$ or $U(1)_{L_\mu - L_\tau}$ models. However, for the high voltage (HV) mode of the experiment there is a potentially important process that is not included in the neutrino contour as we defined it: neutrino-electron scattering. Many DD experiments perform analyses of electron scattering events in parallel with their standard nuclear recoil analyses, and we will discuss some of these in more detail in the next chapter. For SuperCDMS HV, however, and its predecessor CDMSlite, neutrino-electron scattering will inevitably contribute to the event rate in any analysis, as they lack the ability to discriminate between nuclear and electron recoils.

In this chapter, I will present my ongoing work with David Cerdeño and the Super-

CDMS collaboration to derive direct constraints on a $U(1)_{B-L}$ model[1], using data from Run 2 of CDMSlite. While CDMSlite is not expected to set competitive limits on the model, this analysis will act as proof-of-concept for future analyses of electron scattering at SuperCDMS SNOLAB HV.

6.1   Neutrino-electron scattering at CDMSlite

The expected neutrino-electron scattering rate in a DD experiment can be calculated in a similar way to the CEνNS rate given in Eq. 5.1.1. However, there are a few important differences which we will have to account for. Some of these are well understood and trivial to account for, but others present major challenges that are still the subject of ongoing work.

As we discussed in Chapter 2, most direct detection experiments employ multiple detection channels. The signals from these can be compared to directly discriminate between nuclear and electronic scattering events, and are also used to determine the recoil energy of the event. In CDMSlite, however, the two signals are combined, as a side effect of the high voltage applied to improve sensitivity to low-energy recoils [58]. This eliminates the ability to distinguish electron from nuclear recoils, but also adds a complication to the determination of the recoil energy of events. A nuclear and an electron recoil of a given energy will on average impart different amounts of energy into the so-called ionisation signal [233]. Indeed, it is this difference that allows the two to be distinguished in the iZIP configuration of SuperCDMS. When the ionisation and phonon signals are combined, however, we find that a given event can be reconstructed with two different energies, depending on whether it is assumed to be the result of nuclear or electron scattering.

As most of the events expected in CDMSlite are due to electron scattering, all events are treated as electron recoils for the purposes of reconstructing the recoil energy,

---

[1]The $U(1)_{L_\mu - L_\tau}$ model will be discussed in the following chapter.

which is labelled E_{ee}, or electron-equivalent energy. For a nuclear recoil, this is related to the actual recoil energy, E_{nr}, by the equation

$$E_{\text{ee}} = E_{\text{nr}} \left(\frac{1 + Y\left(E_{\text{nr}}\right) eV_b/\epsilon_\gamma}{1 + eV_b/\epsilon_\gamma} \right), \qquad (6.1.1)$$

where V_b is the voltage applied across the detector, e is the elementary electric charge, and ϵ_γ is the energy required to create one electron-hole pair in the detector material. For germanium, the material used in CDMSlite, $\epsilon_\gamma = 3$ eV. The yield, $Y\left(E_{\text{nr}}\right)$, can be approximated by the Lindhard model [234, 235]:

$$Y\left(E_{\text{nr}}\right) = \frac{k \cdot g(\varepsilon)}{1 + k \cdot g(\varepsilon)}, \qquad (6.1.2)$$

where $g(\varepsilon) = 3\varepsilon^{0.15} + 0.7\varepsilon^{0.6} + \varepsilon$, $\varepsilon = 11.5 E_{\text{nr}}(\text{keV})Z^{7/3}$ and for germanium we set $k = 0.157$ [58]. This model has been shown to give good agreement with tests performed on germanium down to energies of around 250 eV$_{\text{nr}}$ [236]. Below this energy, however, its accuracy has not yet been confirmed. Testing the behaviour of Lindhard model down to the low energies that will be probed at SuperCDMS SNOLAB remains an important physics goal for the SuperCDMS collaboration [58]. In this work, we will assume that the above Lindhard model continues to describe the relationship between E_{ee} and E_{nr} across the whole energy range of CDMSlite. The total signal expected in the experiment can therefore be computed by converting the simulated spectrum of nuclear recoil events to units of E_{ee} and adding this to the expected spectrum of electron recoils.

Now that we have defined the energy parameters we will be using, we can naïvely write down a master equation for the rate of neutrino-electron scattering, analagous to Equation (5.1.1),

$$\frac{dR_{\nu e}}{dE_{\text{ee}}} = \frac{N_e}{m_A} \int_{E_\nu^{\text{min}}} dE_\nu \frac{d\phi_\nu}{dE_\nu} \frac{d\sigma_{\nu e}}{dE_{\text{ee}}}, \qquad (6.1.3)$$

where N_e is the number of available electrons per target nucleus within the detector. The contributions to the cross section, $d\sigma_{\nu_e}/dE_{\text{ee}}$, from both the SM and the $U(1)_{B-L}$ mediator were introduced in Chapter 4, and the neutrino flux spectrum, $d\phi_\nu/dE_\nu$, is the same as for CEνNS, shown in Figure 3.4. However, as the electron is much

lighter than an atomic nucleus, the minimum neutrino energy required for a given recoil energy is much smaller,

$$E_\nu^{\min} = \frac{1}{2}\left(E_{\mathrm{ee}} + \sqrt{E_{\mathrm{ee}}(E_{\mathrm{ee}} + 2m_e)}\right). \tag{6.1.4}$$

The relevant neutrino flux populations for neutrino-electron scattering in DD experiments are therefore the more numerous low energy neutrinos, most significantly the pp neutrinos.

Additionally, the neutrino-electron scattering cross section in Equation (4.1.2) depends on the flavour of the incident neutrino, with electron neutrinos having an additional scattering channel compared with muon and tau neutrinos. We will therefore need to know the fraction of solar neutrinos arriving in the ν_e eigenstate. Since all the relevant solar neutrino populations are generated in the ν_e eigenstate, the required quantity is the electron-neutrino survival probability, $P_{ee} = P(\nu_e \to \nu_e)$. For this project, we took the values for P_{ee} from Ref. [237].

The final missing ingredient in Equation (6.1.3) is N_e, the number of electrons available for scattering per target nucleus in the detector. In the most naïve analysis we assume $N_e = Z$, as there are Z electrons per atom with atomic number Z. However, many of these electrons inhabit shells with binding energies significantly larger than the recoil energies we are sensitive to. Our initial analysis will cover the energy range between 56 eV$_{\mathrm{ee}}$ and 2 keV$_{\mathrm{ee}}$, while the binding energy of the inner 1s shell of germanium is ~ 11.1 keV [238].

Some analyses have attempted to account for this by only considering electrons whose binding energies are smaller than the recoil energy being considered [239]. This is sometimes referred to as the Z_{eff} approach, in which only electrons in the outer shells are assumed to scatter, and are treated as free particles. In this approach, N_e is an energy dependent quantity, with

$$N_e(E_{\mathrm{ee}}) = \sum_{i=1}^{Z} \Theta(E_{\mathrm{ee}} - B_i) \tag{6.1.5}$$

where B_i is the binding energy of the ith electron, and $\Theta(E_{\mathrm{ee}} - B_i)$ is a Heaviside

function [240].

However, electrons in atomic matter are not free particles. It has been shown that treating electrons in bound states, either in atomic shells or semiconductor band structures, as free particles whose initial and final states are plane waves can lead to substantial discrepancies in predicted event rates [241, 242]. Deriving accurate constraints on new physics from neutrino-electron scattering at CDMSlite and future SuperCDMS detectors will therefore require us to account for the wavefunctions of the electrons in the target volume.

6.1.1 Neutrino scattering with electrons in a semiconductor

Previous works have studied the effects of particles scattering with bound electrons in the context of DD experiments [243]. Several liquid xenon experiments have performed searches for the signals of low-mass, sub-GeV DM scattering with electrons [244, 245]. As LXe is a noble liquid, all the electrons in these experiments are bound within atomic orbitals. If the scattering rate is calculated for all the electrons in a single atom, this can then be scaled to calculate the total scattering rate within the detector.

However, for semiconductor-based experiments like CDMSlite, the calculation is more complicated. While the innermost electron orbitals remain bound to a single atom, the outer, valence, electrons share a complex band structure, as they form the covalent bonds that hold the semiconductor crystal together. A scattering event may raise an electron into the conduction bands, separated from the valence bands by a band gap (0.67 eV in germanium [246]). To calculate the neutrino-electron scattering rate within a germanium crystal[1], we will need to consider the overall structure of the crystal lattice.

---

[1]SuperCDMS SNOLAB HV will utilise both germanium and silicon targets. Here we focus on germanium as this was the target used in CDMSlite, but the calculations for silicon will be very similar.
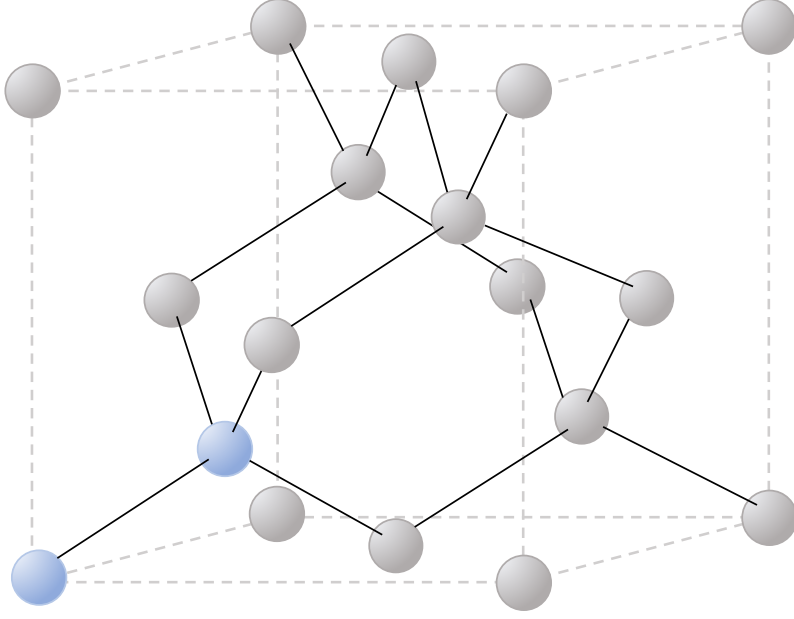
Figure 6.1: Arrangement of ions in a germanium crystal. The crystal has an fcc lattice structure, with the two-ion basis (blue) repeated at every lattice point. The structure is known as a diamond cubic structure.

The physics of a crystal is described by its lattice structure, and the basis of ions reproduced at each lattice point, known as its primitive cell. In the case of germanium, each primitive cell contains two germanium ions (for example the two highlighted in blue in Figure 6.1), and this structure is reproduced at every point in a face-centred cubic (fcc) Bravais lattice [247]. This is the same structure that is found in diamond, albeit with germanium ions in place of carbon, so it is sometimes referred to as a diamond cubic lattice. A single "conventional cell", a cubic section of the crystal structure with side-lengths equal to the lattice constant (5.65 Å for germanium), is shown in Figure 6.1.

The valence electrons in a germanium crystal experience a periodic potential from the germanium ions in the lattice. Bloch's theorem tells us if the electrons are subject to a perfectly periodic lattice potential, the wavefunctions of the valence and conduction states in a single primitive cell may be written as

$$\psi_{j,\vec{k}}(\vec{x}) = u_j(\vec{x})e^{-i\vec{k}\cdot\vec{x}}, \tag{6.1.6}$$

where $u_j(\vec{x})$ is a function with the periodic properties of the lattice and $\vec{k}$ is a
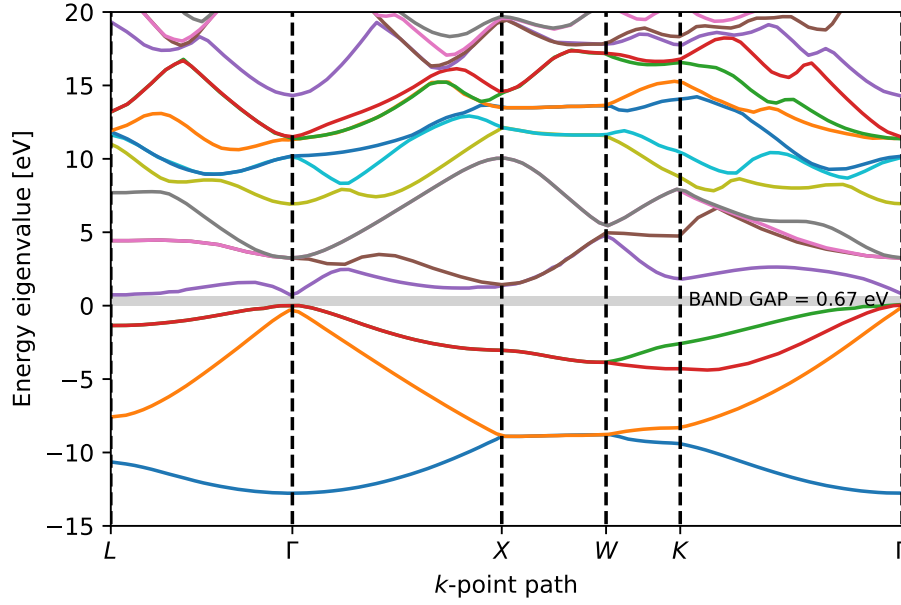
Figure 6.2: Scissor corrected band structure of a germanium crystal, showing the energy levels of the valence bands and the first 14 conduction bands. The scissor correction is employed to enforce a band gap of 0.67 eV. The indices on the x-axis denote the path through the Brillouin zone. A graphical representation of these points can be found in, for example, fig 4.20 of Ref. [248].

wavevector [247]. Furthermore, $\vec{k}$ may always be chosen from the wavevectors that lie within the first Brillouin zone: the equivalent of the primitive cell constructed within reciprocal space.

As $u_j(\vec{x})$ is a periodic function, it may be written as a Fourier series over the reciprocal lattice vectors, $\vec{G}$, so that

$$\psi_{j,\vec{k}}(\vec{x}) = \sum_{\vec{G}} c_{j,\vec{k}+\vec{G}}\, e^{-i(\vec{k}+\vec{G})\cdot\vec{x}}\,. \tag{6.1.7}$$

Both the initial and final states of an electron in the crystal can therefore be decomposed into a set of plane waves, provided the relevant coefficients $c_{j,\vec{k}+\vec{G}}$ are known.

Packages have been developed in condensed matter physics to compute these coefficients from first principles, for example CASTEP [249]. These packages take advantage of the fact that while the behaviour of atomic potentials is computationally

expensive to model, at larger radii the potential is well-described by a much simpler pseudo-potential [250]. Since the valence electrons are mostly sensitive to this outer region of the potential, beyond the inner electron orbitals, these pseudo-potentials can be utilised to reproduce the electron band structure of a given crystal. As it is the behaviour of the outer valence and conduction electrons that determines most of the electrical and thermal properties of a material, packages such as CASTEP can be used to compute these properties of a material from first principles [251]. However, care must be taken in selecting the correct class of pseudo-potentials for a given task. In Figure 6.2 we show the structure of valence and conduction bands found in germanium. The ultrasoft pseudo-potentials I used are known to underestimate the size of the semiconductor band gap, so a scissor correction was implemented to reproduce the experimentally measured band gap of germanium.

Some previous works have studied the effects of electron scattering in germanium semiconductors. In Ref. [252], Essig et. al built on their earlier work with xenon atoms to predict the scattering rate of sub-GeV DM with valence electrons in a germanium crystal. They were able to separate the effects of the electronic structure into a "crystal form factor", much like the nuclear form factors we used to calculate the rates of coherent nuclear scattering of both WIMPs and neutrinos. However, the form factor calculated in that work is not sufficient for an analysis on either CDMSlite or SuperCDMS SNOLAB. Firstly, many approximations are made based on the non-relativistic nature of DM scattering. These lead to some important qualitative differences in the phenomenology of the semiconductor response compared with relativistic neutrino scattering. For example, in DM-electron scattering the initial momentum of the bound electron can exceed the momentum of the incoming DM in the lab frame, leading to a significant enhancement of the scattering rate compared with scattering with free electrons at rest. This enhancement would be much less significant for relativistic neutrino scattering. Differences such as this limit our ability to use that work to make inferences about the magnitude of wavefunction effects on the neutrino-electron scattering rate in CDMSlite.

Secondly, in Ref. [252] only the valence electrons were assumed to interact. This is a valid assumption only if the maximum momentum transferred in a scattering event is less than the binding energy of the inner electron orbitals. The analysis in Ref. [252] was therefore limited to recoil energies $E_{ee} < 50$ eV$_{ee}$, lower than even the minimum energy threshold of CDMSlite[1].

The upper energy limit in the work of Essig et. al was enforced partly because the computation was expected to become rapidly more expensive in terms of computing time as the scattering energy, and therefore the number of electrons energetically available to scatter, increased. However, conversations with S. Clark, a member of the CASTEP Developers Group, have indicated that this problem is not insurmountable. The tightly bound inner electron orbitals of germanium have well defined energies and relatively well understood wave functions. Using the CASTEP package [249, 251], we believe that it should ultimately be possible to obtain a more accurate prediction of the semiconductor response to particle collisions across the whole energy range of CDMSlite and SuperCDMS SNOLAB HV.

An alternative method has been used to study the electromagnetic properties of neutrinos through neutrino-electron scattering in germanium crystals [240, 253, 254]. In these works, the rate of ionisation via neutrino scattering was computed using a modification of the Relativistic Random-Phase Approximation, a method tradition- ally used to study photoionisation effects in heavy atoms [255]. In these works, the effects of the semiconductor band structure were neglected, and germanium atoms were considered individually. To validate their results, in Ref. [240] the measured rate of photoionisation in a germanium crystal was compared with the prediction of their model. The authors found excellent agreement for energy transfers above 100 eV$_{ee}$, but below this there were significant discrepancies. It therefore seems likely that the effects of the electron band structure will be most relevant for energies 100 eV$_{ee}$, with the individual atom approach of Refs. [240, 253, 254] providing a good

---

[1]In fact, the 3d orbital of germanium has a binding energy of 30 eV, and so can contribute to scattering at these energies. To account for this, in Ref. [252] a modification was made to the pseudo-potentials used to model the crystal, so that the 3d orbital was treated as a valence state.

description at higher energies. They also compared the neutrino-electron scattering rate predicted using their model with the prediction of the Z_{eff} approximation defined in Equation (6.1.5), which they refer to as the free electron approximation (FEA). They found that it was a good approximation to their model above 1 keV$_{\text{ee}}$, but that below this the FEA gave an overestimate of the scattering rate, with the deviation growing to nearly a factor of 2 around $E_{\text{ee}} = 200$ eV$_{\text{ee}}$.

Ultimately, we would like to derive a crystal form factor approach to neutrino-electron scattering at energies below 2 keV$_{\text{ee}}$ in germanium. If this is achievable, in the future the effects of the electron band structure could be included in an analysis as simply another form factor, without requiring a radically different approach to the analysis. In the meantime, however, we will adopt the Z_{eff} approach, with the understanding that this may cause us to overestimate our cross section by around a factor of 2 at low energies ($E_{\text{ee}} \lesssim 200$ eV$_{\text{ee}}$). The limits presented in Figure 6.4 are therefore likely to be weakened when these effects are included.

6.2 Extracting constraints from CDMSlite Run 2 data

The data from CDMSlite Run 2 takes the form of a list of events, each with an associated recoil energy E_{ee} reconstructed under the assumption that the event involved scattering with an electron. For analysis purposes these are sorted into energy bins of size 10 eV$_{\text{ee}}$ spanning an energy range between 0.056 and 2 keV$_{\text{ee}}$. The data and efficiency curves are taken from the public data release which accompanied Ref. [58]. The data is reproduced in Figure 6.3.

To place constraints on our chosen models of new physics, we perform a Poisson-based binned likelihood analysis, similar to that outlined in Section 2.3. However, in this case we have to account for a non-zero background rate. We define the likelihood of detecting N_{det} counts given an expected background b and some new physics with
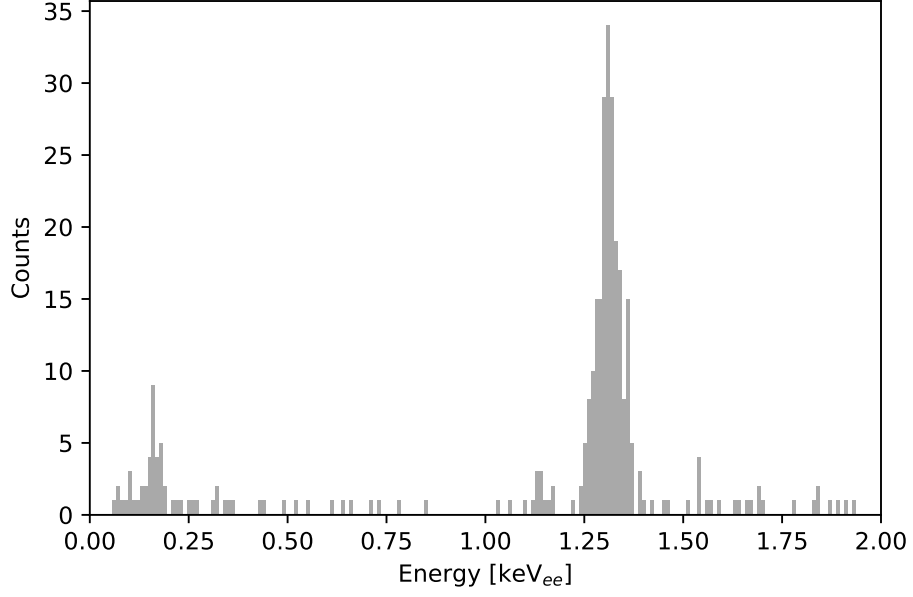
Figure 6.3: The spectrum of events observed during Run 2 of CDMS-lite, with a fiducial exposure of 70.1 kg days [58]. All energies were reconstructed assuming that the initial scattering event was with an electron, rather than an atomic nucleus.

parameters $\boldsymbol{\Theta}$ as

$$\mathcal{L}(N_{\mathrm{det}}|\boldsymbol{\Theta}, b) = \frac{(b+\mu)^{N_{\mathrm{det}}} e^{-(b+\mu)}}{N_{\mathrm{det}}!}, \tag{6.2.1}$$

with $\mu(\boldsymbol{\Theta})$ the expected signal count. We can account for the spectral shape of an experimental result by treating each bin independently and taking the product over the likelihoods calculated for each bin, so for a spectrum $\boldsymbol{\sigma}$ divided into n bins

$$\mathcal{L}(\boldsymbol{\sigma}|\boldsymbol{\Theta}, b) = \prod_{k=1}^{n} \mathcal{L}(N_{\mathrm{det_k}}|\boldsymbol{\Theta}, b). \tag{6.2.2}$$

The profile likelihood statistic for a given point, $\boldsymbol{\Theta}$, in the parameter space of a model is then defined as

$$\lambda(\boldsymbol{\sigma}|\boldsymbol{\Theta}) = \frac{\mathcal{L}(\boldsymbol{\sigma}|\boldsymbol{\Theta}, \hat{b})}{\mathcal{L}(\boldsymbol{\sigma}|\hat{\boldsymbol{\Theta}}, \hat{b})}, \tag{6.2.3}$$

where parameters with a hat over them are selected to maximise the likelihood, with unhatted variables kept constant [256].

The final ingredient required for our analysis is the background rate. As CDMSlite

does not discriminate between electron and nuclear recoils, there are a large number of background sources which cannot be distinguished from a potential signal on an event-by-event basis. These include germanium activation lines (responsible for the large peaks visible in Figure 6.3), and many other backgrounds which have roughly flat spectral shapes. This continuous background is dominated by the Compton scattering of γ-rays [58], but also includes backgrounds from tritium and other beta radiation spectra. To model these backgrounds, we used spectral functions provided by the SuperCDMS collaboration. The normalisation of each background source should then be fitted to the data wherever $\hat{b}$ appears in Equation (6.2.3). However, these normalisations must be weighted to lie within the ranges predicted through simulations, a feature that we have not yet implemented.

An approximate limit can be derived by simply fixing the normalisation of each background source at its best-fit value assuming zero signal. Using this method, we derived constraints on a $U(1)_{B-L}$ model, which are shown in Figure 6.4. These limits are likely to be weakened slightly when both the background fitting and proper handling of the electron band structure are implemented. However, they allow us to examine qualitatively the behaviour of constraints obtained from both CEνNS and neutrino-electron scattering at CDMSlite and similar experiments.

The constraints on a $U(1)_{B-L}$ model from CDMSlite Run 2, presented in Figure 6.4, were derived at the 90% confidence level by computing the coupling g_{B-L} at each new mediator mass $m_{Z'}$ for which the Poisson test statistic $\lambda(\boldsymbol{\sigma}|\boldsymbol{\Theta}) = 2.707$. Comparing the overall constraint with those derived from neutrino-electron scattering and CEνNS individually, we see that each channel allows us to better probe a different region of the parameter space. For masses $m_{Z'} \lesssim 3$ MeV, the inclusion of electron recoils in our analysis allows us to probe smaller couplings, while above this mass the dominant constraints come from CEνNS. This is a pattern that we found was repeated in other DD experiments, during the analysis described in the next chapter. However, in experiments with the ability to distinguish nuclear- and electron-recoil events, fewer backgrounds will in general be present in the nuclear-
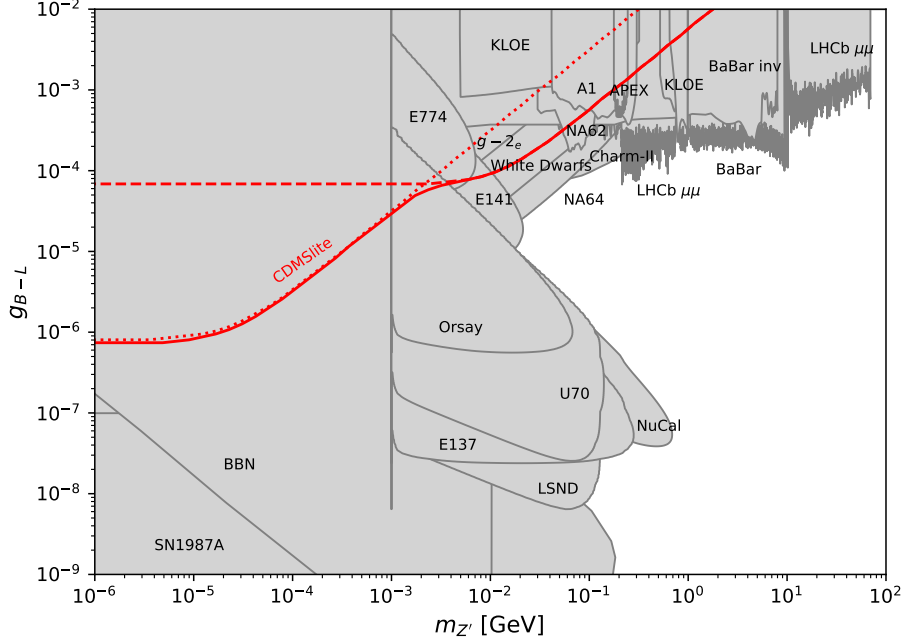
Figure 6.4: Constraint on a $U(1)_{B-L}$ model derived at the 90% confidence level using data from Run 2 of CDMSlite (red, solid line). The red dashed line is the constraint obtained by considering only CEνNS scattering, the red dotted line is obtained from neutrino-electron recoils only. Most of the constraints are the same as those in Figure 4.2, with some additional low-mass constraints taken from Ref. [257].

recoil channel, strengthening the constraints from CEνNS relative to those derived from neutrino-electron scattering.

What can the behaviour of the constraints obtained from electron and nuclear scattering in CDMSlite tell us about the prospects of probing the $U(1)_{B-L}$ model at SuperCDMS SNOLAB HV? If the addition of electron recoils were to improve the sensitivity beyond what is implied by Figure 5.5, we would expect to see the combined constraint in Figure 6.4 lying closer to the unexplored region of the parameter space than the constraint obtained from CEνNS alone. However, this does not appear to be the case, and the region of the parameter space to which neutrino-electron scattering provides sensitivity is already well-excluded by astrophysical and cosmological constraints. It therefore seems unlikely that SuperCDMS SNOLAB will

be able to place constraints on any new regions of the $U(1)_{B-L}$ parameter space. In the next chapter, we will see that our suspicion is confirmed, when we compute the sensitivity of the next generation of DD experiments to the $U(1)_{L_\mu - L_\tau}$ model. We will, however, find that other DD experiments will be sensitive to currently unexplored regions of that parameter space. These regions will be of particular importance due to recent results from the Muon g-2 experiment at the Fermi National Accelerator Laboratory (Fermilab) [258].

Chapter 7

Solar neutrinos, $(g-2)_\mu$, and the gauged $U(1)_{L_\mu - L_\tau}$

We have seen that DD experiments can be sensitive to models of new physics with light mediators that affect neutrino scattering with atomic matter. We will now examine the parameter space of one of these models in more detail: the $U(1)_{L_\mu - L_\tau}$ model. This model was chosen in particular as it has the potential to resolve a longstanding discrepancy within particle physics: the muon g-2 anomaly. Since publication, this work has gained additional relevance, with the long-awaited results of the Muon g-2 experiment further strengthening the anomaly.

In this chapter, we will introduce the muon anomalous magnetic moment, and show that the $U(1)_{L_\mu - L_\tau}$ model is particularly well suited to provide a solution to the current disagreement with the SM. We will also discuss the H_0 tension: an ongoing problem in cosmology that can likewise be resolved by the addition of a $U(1)_{L_\mu - L_\tau}$ gauge symmetry. We will then explore the extent to which solar neutrino scattering may be used to probe the regions of the $U(1)_{L_\mu - L_\tau}$ parameter space that can solve these problems, both at current and future DD experiments and using results from the solar neutrino detector Borexino.

This chapter is based on my work with D.W.P. Amaral, D. Cerdeño, and P. Foldenauer, which resulted in the publication of Ref. [3].

7.1   The muon anomalous magnetic moment

The study of the magnetic moments of fundamental particles, especially charged leptons, has played a crucial role in the development of particle physics over the past 100 years. In 1922, the Stern-Gerlach experiment studied the deflection of a beam of silver atoms passing through a transverse magnetic field. Famously, the beam was found to split in two, with atoms being deflected towards one of two points on either side of the original trajectory. This result confirmed the quantised nature of angular momentum, but it did not match the original prediction of the Bohr-Sommerfeld theory that the experiment had been designed to test. Initially, it had been expected that the beam would split into three, as silver atoms were assumed to have an angular momentum number of $L = 1$. In fact, silver atoms exist in the $L = 0$ state: the magnetic moment being measured was due to the spin of the electron. Although the theory of spin would not be formalised for some time later, the Stern-Gerlach experiment therefore represents one of the first pieces of evidence of the magnetic moment of a fundamental particle [259].

The magnetic moment of a lepton, $\vec{\mu}_l$, is related to its spin, $\vec{s}$, by the equation

$$\vec{\mu}_l = g_l \mu_B \vec{s}, \tag{7.1.1}$$

where μ_B is the Bohr magneton and the g-factor, g_l, is a dimensionless parameter. An early success of the Dirac equation was its prediction of the electron g-factor, $g_e = 2$ [260].

Later, Schwinger computed one of the first loop-corrections to a quantity, when he calculated the first QED correction to the electron magnetic moment. Although we colloquially refer to this "anomalous" part of the electron magnetic moment as $(g-2)_e$, the quantity that is typically measured is $a_e = (g_e - 2)/2$. Schwinger's celebrated result was that $a_e = \alpha/2\pi$, where $\alpha = 1/137$ is the fine structure constant [261]. The agreement of this result with experiment was a triumph for QED, but it was known that additional contributions should exist due to higher order quantum corrections.
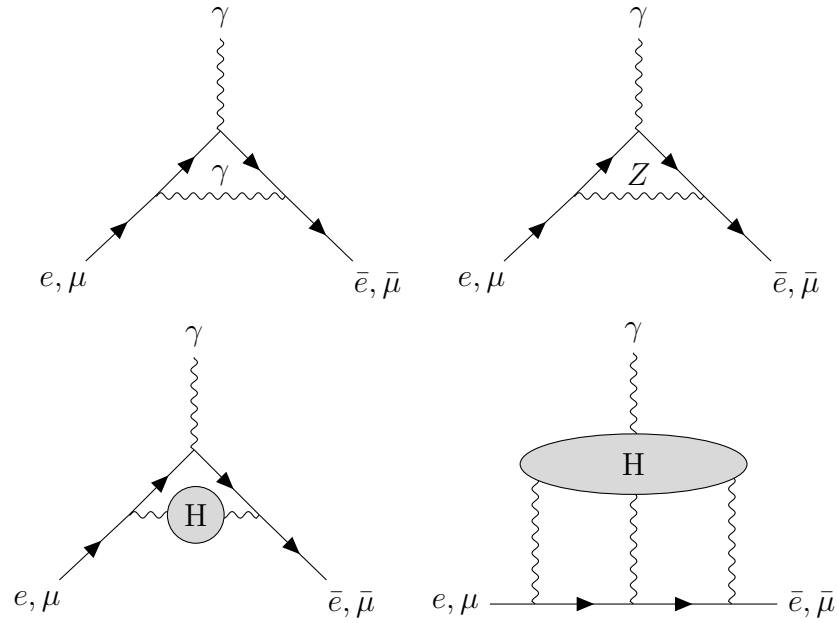
Figure 7.1: Examples of loop diagrams which contribute to a_e and a_μ. These include QED corrections (*top left*), weak corrections (*top right*), hadronic vacuum polarisation (*bottom left*), and hadronic light-by-light corrections (*bottom right*).

Over the second half of the 20th Century, the anomalous magnetic moment of the electron, and its 2nd generation counterpart, the muon, were calculated and measured to increasingly fine precision, and both values are now counted among the most precisely measured quantities in physics.

Feynman diagrams for some of the types of process that contribute to a_e and a_μ are shown in Figure 7.1. The wide range of physics that contributes to the computation of these values makes them an important tool for verifying our theories of particle physics.

In the early 2000s, the E821 experiment at Brookhaven National Laboratory measured the muon anomalous magnetic moment to a precision of 0.54 ppm. This result was in tension with the best theoretical predictions based on the SM at the time, with the measured value exceeding the theoretical prediction by around 2.2-2.7 standard deviations (σ) [262]. In the following 15 years, improvements in the precision
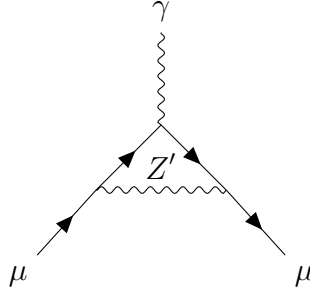
Figure 7.2: Feynman diagram for the leading order correction to a_μ resulting from a $U(1)_{L_\mu - L_\tau}$ gauge boson.

of theoretical predictions lead to an increase in this tension, eventually rising to $3.7\,\sigma$[1]. Then, in April 2021, a long-awaited result from the Muon $g-2$ experiment at Fermilab strengthened the deviation from accepted SM predictions when they measured a_μ with a precision of 0.46 ppm [258]. Combining this result with the earlier measurement at BNL leads to an overall significance of $4.2\,\sigma$ in the deviation, a significant hint of physics beyond the SM.

Meanwhile, the most precise determination of the electron anomalous magnetic moment has revealed a $2.4\,\sigma$ tension with the best SM prediction. In this case, though, the measured value lies 2.4 standard deviations below the best theoretical prediction. This combination of a positive tension in a_μ and a negative tension in a_e is difficult to resolve with any new physics models which do not involve some violation of lepton flavour universality [265].

It has been shown in many previous works that a gauged $U(1)_{L_\mu - L_\tau}$ model has the potential to alleviate the observed tension in a_μ [266–269]. Furthermore, it is the only minimal anomaly-free $U(1)$ gauge-symmetric models discussed in Chapter 4 where a solution to the a_μ discrepancy is allowed under current constraints [177,270], as it evades many of the leading constraints on those other models from electron-scattering experiments.

---

[1]A recent lattice result of the leading order hadronic vacuum polarisation [263] could significantly reduce this difference. However, this comes at the expense of worsening fits to other precision EW observables [264].
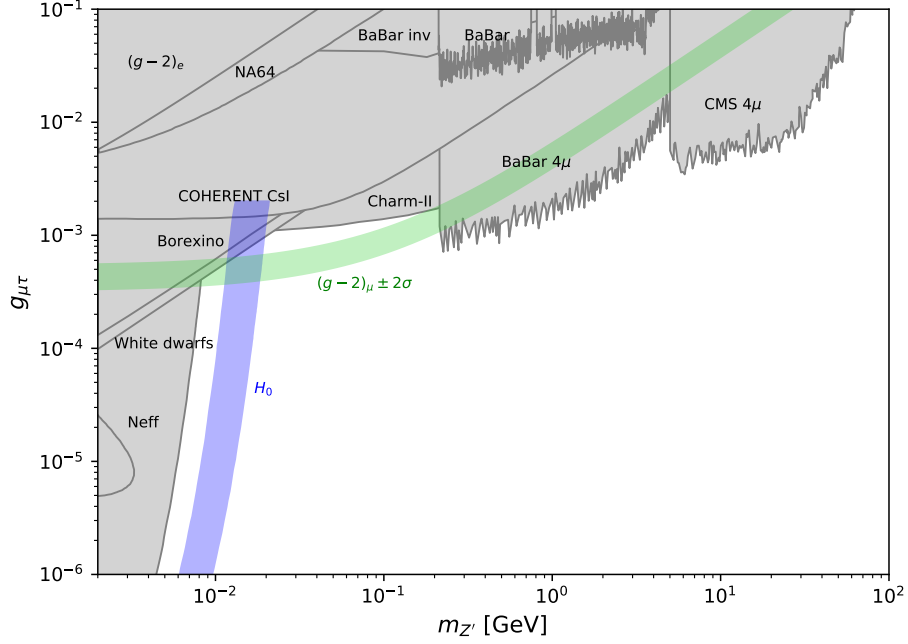
Figure 7.3: Regions of the gauged $U(1)_{L_\mu - L_\tau}$ parameter space favoured by solutions to the tensions in $(g-2)_\mu$ (green) and H_0 (blue). Existing constraints are shown in grey.

The leading additional contribution to a_μ in the gauged $U(1)_{L_\mu - L_\tau}$ model is due to the one-loop process shown in Figure 7.2. For a $U(1)$ gauge boson interacting in this way, the additional contribution to a_μ can be written in the form [271]

$$\Delta a_\mu = Q_\mu'^2 \, \frac{g_{\mu\tau}^2}{4\pi^2} \int_0^1 du \, \frac{m_\mu^2 u^2 (1-u)}{m_\mu^2 u^2 + m_{Z'}^2 (1-u)} \, , \qquad (7.1.2)$$

where Q_μ' denotes the charge of the muon under the new gauge symmetry, $Q_\mu' = 1$. Combining the results of the experiments at BNL and Fermilab, the measured deviation from the SM stands at $\Delta a_\mu = 251(59) \times 10^{11}$. From this, we can compute the $2\,\sigma$ preferred region of the $U(1)_{L_\mu - L_\tau}$ parameter space, which we show alongside existing constraints in Figure 7.3.

7.1.1 The H_0 tension and the gauged $U(1)_{L_\mu - L_\tau}$

The $U(1)_{L_\mu - L_\tau}$ has also been proposed as a solution to another ongoing problem in physics, the $> 3\,\sigma$ tension in determinations of the Hubble constant, H_0 [272]. H_0

is the key parameter of Hubble's law, which describes the current rate of expansion of the Universe,

$$v = H_0 D, \tag{7.1.3}$$

where v is the recession velocity of an object a proper distance D from the observer. The traditional approach to calculating H_0 requires us to measure the velocity (via redshift) of astronomical objects at known distances from the Earth. This involves the use of "standard candles": objects whose absolute magnitude, and therefore distance from Earth, can be determined from observable properties. However, in order to accurately determine H_0 the objects must be sufficiently distant that their velocities are not affected by the gravitational influence of the Milky Way. In order to determine the absolute magnitudes of sufficiently luminous objects, a so-called distance ladder approach is used [273]. Parallax measurements are used to measure distances to local Cepheid variables: stars whose luminosity varies with a time period related to their average luminosity. Cepheid variables can be used to calculate distances to distant galaxies, which allows for the calibration of a much brighter standard candle: Type Ia supernovae. These are then employed to measure the relationship between distance and redshift in very distant regions of the Universe. In recent years, improved measurements of all these steps in the distance ladder have allowed a precise determination of the Hubble constant, with uncertainties as low as 2.4% [274]. This method relies on accurate modelling of stellar astrophysics, though there is evidence that the determination is quite robust to changes in the underlying stellar models [275, 276].

With improvements in measurements of the Cosmic Microwave Background (CMB), an alternative approach to determine H_0 is now possible. Measurements of the CMB power spectrum by the European Space Agency's Planck satellite provide the strongest evidence yet in favour of the ΛCDM model of cosmology. The power spectrum that ΛCDM predicts is sensitive to H_0, and it is therefore fitted alongside other parameters to the data acquired by Planck [11, 277]. This provides a determination of H_0 that is independent of the above distance ladder approach, though it

is computed under the assumption of the ΛCDM model.

Upon comparing the two values, a deviation greater than 3σ is found. If this difference is assumed not to be the result of a statistical fluctuation, resolving the tension is likely to require a modification of either early-universe physics or late-time cosmology [278]. The presence of a $U(1)_{L_\mu - L_\tau}$ gauge boson with a mass around $10 - 20$ MeV could modify N_{eff}, the effective number of neutrino degrees of freedom at the time of last scattering of the CMB. This would lead to a modification in the value of H_0 determined from Planck data, alleviating the tension. The region of the $U(1)_{L_\mu - L_\tau}$ parameter space favoured by this resolution of the H_0 tension, taken from Ref. [272], is also shown in Figure 7.3. Intriguingly, the region which could resolve both the H_0 and $(g-2)_\mu$ tensions is only partly constrained by current bounds. This region represents an exciting opportunity for future experiments to test a possible simultaneous solution to two important problems in fundamental physics.

7.2 Solar neutrino probes of the gauged $U(1)_{L_\mu - L_\tau}$

We have seen that a $U(1)_{L_\mu - L_\tau}$ gauge boson can provide a solution to the tensions in a_μ and the Hubble constant. We now wish to examine whether solar neutrinos can be used to test these solutions. In order to derive constraints based on solar neutrino scattering, however, it is important that we understand the flux of solar neutrinos that will be incident on our detectors.

In Chapter 6, we calculated the rate of solar neutrino scattering with electrons, and noted that the additional SM scattering channel with electron-neutrinos meant that solar neutrino oscillation probabilities had to be considered. However, as the cross sections for ν_μ and ν_τ scattering were identical, only the electron-neutrino survival probability was needed. In the $U(1)_{L_\mu - L_\tau}$ model, each neutrino flavour has a different charge under the new symmetry: $Q_{\nu_e} = 0$, $Q_{\nu_\mu} = 1$, $Q_{\nu_\tau} = -1$. As a result, the

cross sections for both CEνNS and neutrino-electron scattering will be different for each neutrino eigenstate, and calculating the relevant scattering rates will require us to know the population of each flavour reaching Earth.

7.2.1   3-flavour solar neutrino oscillations

As we could not find any data on the three-flavour transition probabilities of solar neutrinos in previous works, we decided to compute them. In Chapter 3 we showed that solar neutrinos are produced primarily in the ν_e flavour eigenstate. This corresponds to a superposition of mass eigenstates determined by the mixing angles in matter, which depend on the vacuum mixing properties and the local density of electrons. If the electron number density evolves gradually enough along the path taken out of the Sun, the neutrinos propagate adiabatically, with the occupancy of the three mass eigenstates remaining unchanged. When they reach the surface of the Sun, the neutrinos continue to propagate to the Earth in their mass eigenstates. As the distance from the Sun to the Earth is many orders of magnitude longer than the neutrino oscillation length, the neutrinos separate into a decoherent mixture of mass eigenstates, so that the overall transition probability from the Sun's core to detection in an experiment is given by

$$P(\nu_e \to \nu_\alpha) = \sum_{i=1}^{3} |U_{\alpha i}|^2 P_i, \tag{7.2.1}$$

with P_i the probability of the neutrino arriving at the detector in the ν_i mass eigenstate and U the PMNS matrix [145, 156].

To compute P_i, we must know the matter mixing angles at the point in the Sun where the neutrinos were produced. In Section 3.2.1, we showed how the matter mixing angle could be computed in the 2-neutrino approximation. We saw that the magnitude of the matter effects depended on the ratio l_v/l_0, where l_v is the vacuum oscillation length and l_0 is the refraction length of the medium, which depends on the local electron density N_e. A similar approach can be used to calculate
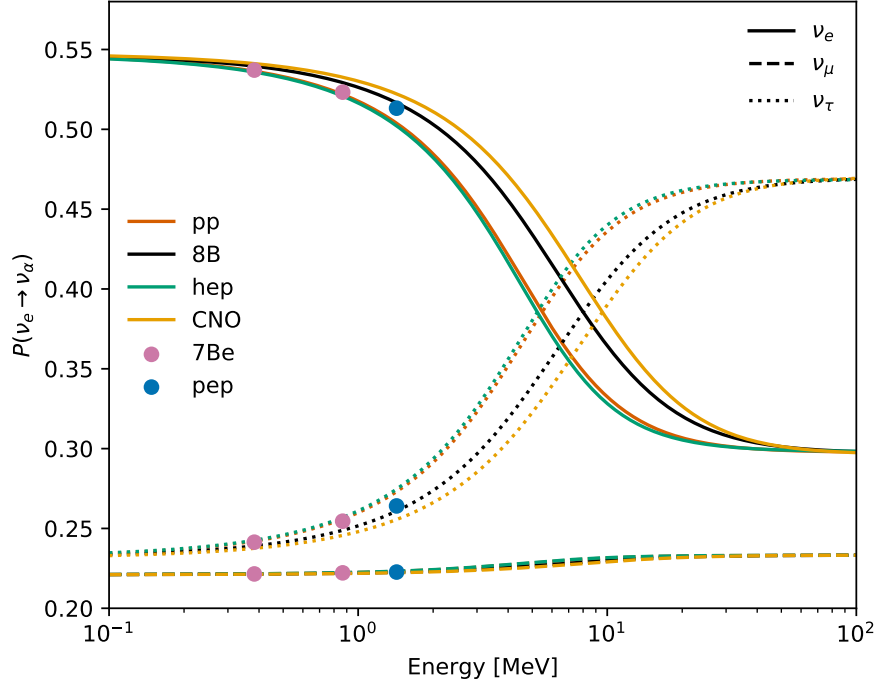
Figure 7.4: Probability of a solar neutrino produced in the ν_e flavour eigenstate being detected on Earth in the ν_α flavour eigenstate. Each neutrino flux source has a different oscillation probability as they are produced in different regions of the Sun. Terrestrial day/night effects are neglected.

matter mixing effects in the three-neutrino paradigm. Taking values for N_e from the Standard Solar Model [279], we find that for the larger of the two mass splittings, $\Delta m^2_{31} = 2.525 \times 10^{-3}$ eV (assuming normal ordering) [156], $l_v \ll l_0$ for all electron densities found in the Sun. We can therefore make the approximation that $\theta_{13,m} \approx \theta_{13}$, and $P_3 = \sin^2 \theta_{13}$ for all solar neutrinos arriving at Earth.

The matter induced mixing angle, $\theta_{12,m}$, can be calculated using Equation (3.2.9), and will vary with both the neutrino energy and the location within the Sun where the neutrino is produced. As the rates of different solar fusion reactions vary with temperature and density, each solar neutrino flux population has a different radial production distribution, $f(r)$, which we take from Ref. [237]. The fractions of each neutrino population arriving in the ν_1 and ν_2 eigenstates depend on the matter

induced mixing angles averaged over the regions in which they are produced, so

$$P_1(E) = \cos^2 \theta_{13} \int_0^{R_\odot} dr\, f(r) \cos^2 \theta_{12,m}(E, r), \qquad (7.2.2)$$

$$P_2(E) = \cos^2 \theta_{13} \int_0^{R_\odot} dr\, f(r) \sin^2 \theta_{12,m}(E, r), \qquad (7.2.3)$$

with $R_\odot$ the radius of the Sun.

Inserting these probabilities into Equation (7.2.1), we obtain the probabilities of finding a solar neutrino in each of the three flavour eigenstates in a detector on Earth, which we show in Figure 7.4. Terrestrial matter effects could further modify these probabilities and lead to a day/night asymmetry, as neutrinos arriving during the night must traverse a chord through the Earth, leading to some non-adiabatic conversion between the different mass states as the neutrinos enter the dense interior of the planet [280]. However, these effects are quite small, and we neglect them here.

One may wonder whether there would be any change in the oscillation probabilities due to the additional flavour non-universal interactions induced in the gauged $U(1)_{L_\mu - L_\tau}$ model. However, since the $U(1)_{L_\mu - L_\tau}$ gauge boson has no tree-level coupling to electrons, the dominant new physics interactions will proceed through loop-induced mixing with the photon. This mixing will allow the $U(1)_{L_\mu - L_\tau}$ boson to couple to both electrons and protons. Assuming the interior of the Sun is approximately electrically neutral, the two contributions to the matter potential from positively charged protons and negatively charged electrons will exactly cancel, leading to no modification of the neutrino oscillation probabilities [281].

Before we begin to derive constraints on the $U(1)_{L_\mu - L_\tau}$ model, there is one aspect of solar physics we must discuss: the solar metallicity problem. We mentioned this problem in passing in Chapter 3, but we will now recap its origin and discuss its impact on solar neutrino rates.

7.2.2 The solar metallicity problem

The solar metallicity problem (sometimes called the solar abundance problem) is a discrepancy that exists between different determinations of the abundance of elements heavier than helium within the Sun. In astrophysics, all elements with $Z > 2$ are generically called metals, so we refer to this abundance as the solar metallicity.

The composition of the solar surface can be determined using spectroscopic imaging, which provides an important input for the construction of the SSM [115]. In the 1990s, measurements of solar surface abundances [282] allowed detailed modelling of the Sun's interior and found good agreement with results from helioseismology [283]. Recently, updated spectroscopic measurements which incorporate more advanced atmospheric modelling have supported surface metal abundances that are lower than those early results by up to a factor of 2 [284, 285]. These results, however, are not compatible with helioseismology, and no solutions have yet been found to fully resolve the discrepancy [286].

The solar metallicity problem is of great importance in astrophysics. Almost all of our determinations of metal abundances in astrophysical objects rely in part on our measurement of solar abundances [115]. For our work, though, the question of the solar metallicity is important because it directly impacts predictions of the fluxes of solar neutrinos produced during fusion. The rate of the CNO cycle is particularly sensitive to the abundances of its catalyst elements: carbon, nitrogen, and oxygen, and the fluxes of the associated CNO neutrinos differ by almost 50% in the two metallicity scenarios. The other solar neutrino fluxes are also affected, due to differences in the solar temperature and density when computed under the two different sets of assumptions.

Measurements of solar neutrino fluxes, in particular those of CNO neutrinos, may ultimately provide a resolution to the solar metallicity problem [287]. The first confirmed detection of CNO neutrinos at the 5 σ level was recently made by the

Borexino collaboration [288]. However, the result was compatible with both the high- and low-metallicity predictions, and so could not provide an answer to the metallicity question.

In the absence of a clear solution to the solar metallicity problem, we will consider two different sets of neutrino fluxes calculated using different values for elemental abundances. Specifically, we will consider the B16-GS98 solar model, which we will refer to as the high-metallicity, or HZ model; and the B16-AGSS09met model, which we will call the low-metallicity, or LZ model. Values for the neutrino fluxes in both models are taken from Ref. [115].

In previous chapters, we took our fluxes from the high-metallicity model. These values are often used, as measurements of neutrino scattering at detectors such as Borexino currently slightly favour a high-metallicity Sun [155]. However, we note that the presence of additional particles mediating neutrino scattering could bring the results of Borexino into closer agreement with the generally smaller neutrino fluxes of the LZ solar models. In the remainder of this chapter, we will compute our limits and sensitivities using both the HZ and LZ neutrino fluxes. Although the differences in our results are small, we believe it is important to remain aware of the current discrepancy. By presenting results for both cases we hope that our work will remain relevant regardless of the eventual resolution of the solar metallicity problem.

7.2.3   Constraints from Borexino

With its large fiducial volume and low background rates, the Borexino experiment has been responsible for many of the most precise direct measurements of solar neutrino scattering to-date. Its analyses of neutrino-electron scattering have covered an energy range from 0.19 to 20 MeV, and it has measured or placed constraints on the fluxes of pp, ^{7}Be, pep, ^{8}B, hep, and CNO neutrinos [155]. These measurements allow us to place constraints on many models of new physics that would affect the neutrino-electron scattering rate.

Of the many solar neutrino flux populations, Borexino has measured the ^{7}Be flux to the highest precision. This, combined with the fact that the effect of a new light mediator is expected to be greater at low energies, means that the ^{7}Be measurement is likely to provide us with the strongest constraints on the $U(1)_{L_\mu - L_\tau}$ model.

In Ref. [289], the Borexino collaboration measured the ^{7}Be flux to a precision of 5%, finding it to be in agreement with the SM prediction. This result has been used to place constraints on a range of new physics models. In Ref. [176], a constraint was placed on a light $U(1)_{B-L}$ gauge boson, excluding any region of the parameter space which would lead to an increase in the ^{7}Be scattering rate of more than 8% (approximately corresponding to a 90% CL for a measurement with a $1\,\sigma$ uncertainty of 5%). This result has been translated into a constraint on a $U(1)_{L_\mu - L_\tau}$ gauge boson through a remapping of the related couplings [290], and it is this constraint which is labelled "Borexino" in Figure 7.3. However, we found that we were able to improve on this analysis in several ways. Firstly, we found that the $U(1)_{B-L}$ analysis had not properly accounted for theoretical uncertainties associated with the SM and SSM. They also did not consider the two possible scenarios for the solar metallicity, assuming that the HZ fluxes were accurate, despite both the HZ and LZ case being discussed in Ref. [289]. Secondly, by computing the constraint directly on the $U(1)_{L_\mu - L_\tau}$ parameter space, we were able to incorporate the full neutrino-electron cross section from Equation (4.2.9), including the interference term between SM and new physics channels, which were neglected in previous analyses. Finally, additional data from Phase-II of Borexino has allowed an even more precise determination of the ^{7}Be flux, with a total uncertainty of only 2.7% [155]. This updated result further justifies a recalculation of the Borexino constraint on both the $U(1)_{L_\mu - L_\tau}$ and the $U(1)_{B-L}$ parameter space.

Ideally, an overall constraint should be computed using the combined results of both phases of Borexino. However, this should not be done without a full understanding the systematic uncertainties associated with the two results. If the two results were treated as independent, the combined analysis would likely over-constrain the

parameter space, giving an unreliable result. To avoid this, we perform two separate analyses on the two sets of results, and display both sets of constraints. As the central value found for the ^{7}Be rate in the Phase-II analysis is larger than that found in the Phase-I analysis, the more precise measurement provides us with the weaker of the two constraints. The two results remain compatible with each other within their respective uncertainties, though, and can be consistently explained as a downward and an upward statistical fluctuation.

We compute our constraints at the 90% CL using a $\Delta\chi^2$ test. As we previously discussed, we perform separate analyses for both the HZ and LZ solar models, with the predicted ^{7}Be flux being approximately 10% smaller in the LZ model. The resulting constraints are displayed for a $U(1)_{L_\mu - L_\tau}$ model in Figure 7.6, and for a $U(1)_{B-L}$ model in Figure 7.7. We include the latter for completeness, and in the remainder of the work we will focus mostly on the $U(1)_{L_\mu - L_\tau}$ parameter space.

7.2.4   Constraints from XENON1T

Around the time that we were preparing Ref. [3], a new analysis of electron recoil data at XENON1T found an excess of events in two of its low-energy bins, between 2 and 3 keV [60]. When compared to their background model, B_0, the excess represented a 3.3 σ fluctuation, although the initial analysis noted that the tension could be eased considerably if the estimated background rate from the β-decay of tritium were revised upwards. As we had already prepared much of the machinery for computing constraints from neutrino-electron scattering in DD experiments, we decided to test the hypothesis that the excess could have been caused by an additional vector gauge boson within our mass range of interest.

We found that the enhancement to the XENON1T spectrum from either a $U(1)_{L_\mu - L_\tau}$ or $U(1)_{B-L}$ mediator with a mass $m_{Z'} \gtrsim 1$ MeV would be mostly flat over the energy range analysed by the XENON1T collaboration, giving a poor fit to the low-energy excess. To demonstrate this, in Figure 7.5 we show the enhancement to
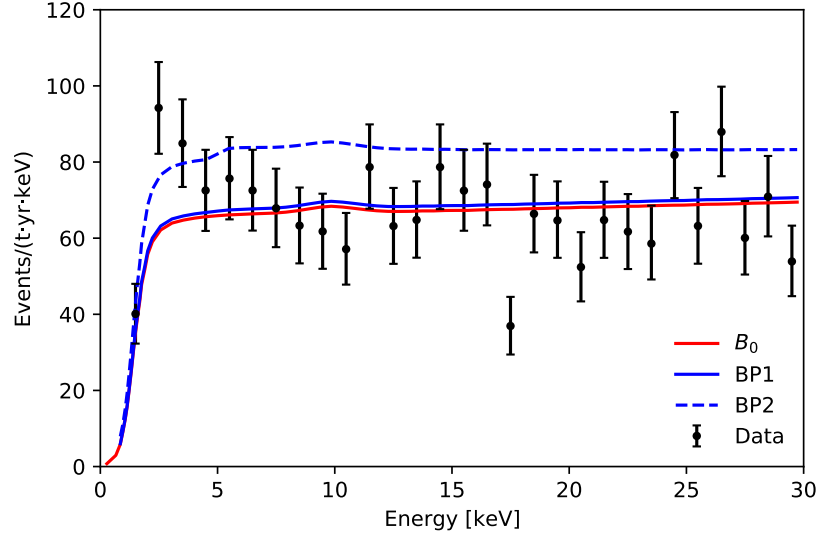
Figure 7.5: Binned spectrum of electron-scattering events observed in XENON1T [60] (points, black). The red line represents the fitted background model, B_0. The blue solid and dashed lines include contributions from scattering via a $U(1)_{L_\mu - L_\tau}$ gauge boson, with mass $M_{Z'} = 15$ MeV and coupling $g_{\mu\tau} = 5.6 \times 10^{-4}$ (BP1) and $g_{\mu\tau} = 1.5 \times 10^{-3}$ (BP2), respectively.

the XENON1T spectrum corresponding to two benchmark points in the $U(1)_{L_\mu - L_\tau}$ parameter space. For the first benchmark point, BP1, we take a mass $m_{Z'} = 15$ MeV and a coupling $g_{\mu\tau} = 5.6 \times 10^{-4}$, which places us within the region of the parameter space that can simultaneously resolve the $(g-2)_\mu$ and H_0 tensions. For the second, BP2, we keep the same mass but increase the coupling to $g_{\mu\tau} = 1.5 \times 10^{-3}$, the point at which our model disagrees with the observed data at the 90% CL, based on the analysis below. Clearly, a $U(1)_{L_\mu - L_\tau}$ gauge boson within our mass range cannot explain the observed excess, which peaks around 2 keV. A light vector mediator can produce a recoil spectrum with a similar peak at low energy, but it requires a mediator mass below ~ 100 keV, a region of the parameter space that is well constrained [171].

If we cannot explain the XENON1T excess using one of our light vector models, we can still derive constraints from it. Since our spectrum is relatively flat and featureless, we derive a constraint at the 90% CL using a simple unbinned $\Delta\chi^2$

analysis. Summing over the data points, we compute the total number of events observed in the energy range $2 - 30$ keV, N_{tot}. We then compare this value with the number of events predicted in the B_0 background model, and in the $B_0 + U(1)_{L_\mu - L_\tau}$ scenario. We then place an upper limit at the 90% confidence level using a $\Delta\chi^2$ test. These constraints are shown for a $U(1)_{L_\mu - L_\tau}$ model in Figure 7.6, and for a $U(1)_{B-L}$ model in Figure 7.7.

As we noted in Chapter 6, this is not strictly the correct way to compute constraints in a background-limited analysis. To obtain more accurate constraints, the background model B_0 should be re-fitted every time we include a new signal model. However, as we discussed in the previous chapter, this type of analysis is much more computationally expensive and requires an in-depth understanding of the underlying background models. The effect of performing this full analysis would be to weaken the constraints obtained in our simplistic approach. Since the limits we obtain from XENON1T do not constrain any new regions of our parameter spaces, we can be confident that a full analysis with variable background amplitudes would also yield constraints that are not competitive with previous works.

7.2.5   Sensitivity of future DD experiments

We now wish to examine the prospects of studying the $U(1)_{L_\mu - L_\tau}$ at future DD experiments. We consider four detectors that we believe to be representative of the future of direct detection. Two of these, SuperCDMS SNOLAB [55] and LZ [291], are considered second generation, or G2, experiments; that is, they are either currently in operation or presently under construction. Their detector properties are therefore quite well established, although some parameters related to background reduction and detector performance may be adjusted during operation. We also consider two proposed G3 experiments: DARWIN [62] and DarkSide-20k [64]. As these experiments are in much earlier stages of development, their properties are far from finalised. We have attempted to construct simplified models of these experiments
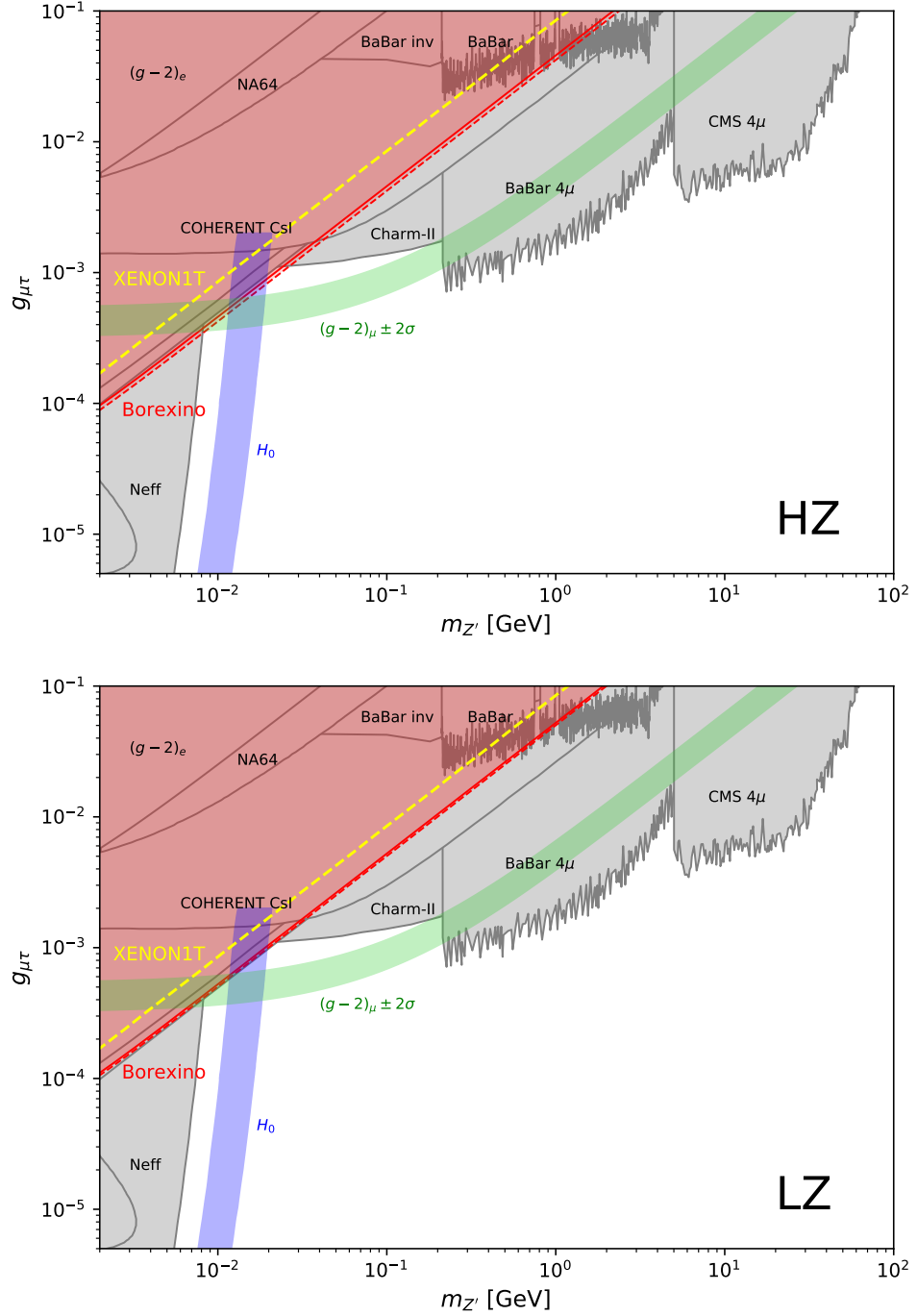
Figure 7.6: Updated constraints on a $U(1)_{L_\mu - L_\tau}$ gauge boson from Borexino (red) and XENON1T (yellow), under the assumption of a high-(*top*) and low-(*bottom*) metallicity SSM. For Borexino, two constraints are shown, derived from the Phase-I (dashed) and Phase-II (solid) results. In the HZ case, Borexino now provides the strongest constraint on the region of the parameter space favoured by $U(1)_{L_\mu - L_\tau}$ explanations of the $(g-2)\mu$ and H_0 anomalies.
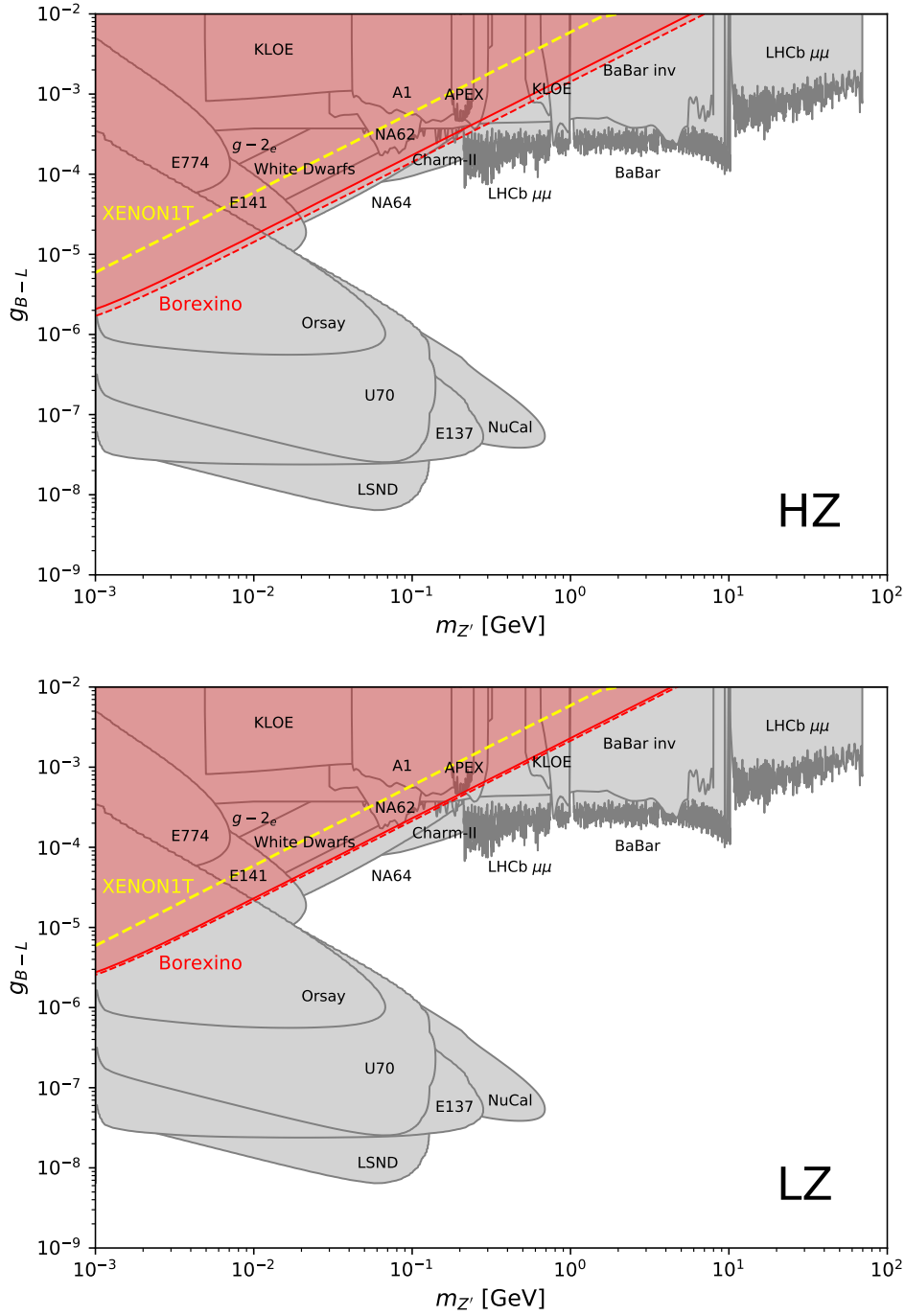
Figure 7.7: As in Figure 7.6, but for a $U(1)_{B-L}$ gauge boson. Here, the updated Borexino constraints are less constraining than those derived from NA64 [174].

Experiment		ε [t·yr]	NR [keV$_{\mathrm{nr}}$]	ER [keV$_{\mathrm{ee}}$]	NR+ER [keV$_{\mathrm{nr}}$]
G2-Ge	(SuperCDMS iZIP [55])	0.056	[0.272, 10.4]	[0.120, 50]	-
	(SuperCDMS HV [55])	0.044	-	-	[0.040, 2]
G2-Xe	(LZ [61])	15	[3, 5.8]	[2, 30]	[0.7, 100]
G3-Xe	(DARWIN [62])	200	[3, 5.8]	[2, 30]	[0.6, 100]
G3-Ar	(DarkSide-20k [64])	100	-	[7, 50]	[0.6, 15]

Table 7.1:   Simplified configurations for direct detection experiments used in this section. Where appropriate, we consider multiple analyses for each experiment, utilising only the nuclear recoil (NR) or electron recoil (ER) channel, or combining the two (NR+ER). In the latter case, energies are given in nuclear recoil equivalent units.

that are as realistic as possible, making assumptions as required.

As we have discussed at length in previous chapters, most DD experiments have some ability to discriminate between nuclear recoil (NR) and electron recoil (ER) events. This allows an analysis of nuclear scattering events free from the larger backgrounds that are generally found in the ER channel. However, in some experiments, like SuperCDMS, this discrimination power can be sacrificed to access lower energy events. We will consider a range of detector configurations: NR, ER, and NR+ER, as appropriate for each of our four future experiments. In this last analysis, we must convert all of our predicted nuclear recoil events into the electron equivalent energy, E_{ee}, as we discussed in Chapter 6.

In Table 7.1, we summarise the key properties of the various experiments: their target material, exposure, and analysis windows. We will now discuss them each in more detail, explaining our choices of detector properties and any assumptions we are making.

G2-Ge   The G2-Ge setup we consider is based on SuperCDMS SNOLAB. As we have discussed in previous chapters, SuperCDMS SNOLAB will utilise two complementary detector modes running in parallel on different detector crystals.

In the iZIP mode, phonon and ionisation signals will be measured to allow discrimination of NR and ER events, while in the HV mode this power will be sacrificed to achieve a lower energy threshold. Although SuperCDMS SNOLAB will employ both germanium and silicon targets, the germanium mass will be much larger, so we neglect the contribution from the silicon detectors here. It should be noted, however, that the silicon HV detectors will have an even lower energy threshold, and so may offer some interesting complementarity in searches for low-mass mediators. The exposures are based on five years of operation with an 80% live time, and we assume a flat 75% efficiency after analysis cuts [55]. Background rates are taken from the predictions in Ref. [55].

G2-Xe The G2-Xe setup is based on LZ and serves as a proxy for other large LXe experiments, such as XenonNT [54] and PandaX [292]. LZ will operate with a fiducial mass of 5.6 tonnes of liquid xenon, and we assume a 1000 day run time [61]. LZ measures two scintillation signals, S1 and S2, to allow a nuclear recoil analysis with 50% acceptance of signal events and 99.5% rejection of ER events [61, 293]. The declared target threshold for their NR analysis has been explicitly chosen to avoid the solar neutrino background. However, the LUX collaboration has been able to obtain 50% efficiency in both the scintillation (S1) and ionisation (S2) channels, required for the target discrimination described above, at an energy of 3.3 keV$_{\text{nr}}$ [294]. Given recent improvements in detector performance, we set our energy thresholds in the NR and ER channels to 3 keV$_{\text{nr}}$. We take our background rates from Ref. [61]. As we are extending our analyses slightly beyond the energy range for which backgrounds are quoted there, we conservatively assume a flat continuation of the background rate outside the known window.

In the NR+ER analysis, we sacrifice measurement of the S1 signal and assume that only the S2 signal is collected. We set our energy threshold at 0.7 keV$_{\text{nr}}$, the threshold achieved by XENON100 in its S2 only analysis [295]. In order to avoid extrapolating the Lindhard model well below the energy range for

which it has been tested experimentally in xenon, we conservatively assume the same lower energy threshold in units of both keV_{nr} and keV_{ee}. Explicit checks show that including the Lindhard model at low masses does not affect our constraints in regions of the parameter space relevant for our work.

G3-Xe For our G3-Xe experiment we use DARWIN, a proposed future LXe detector which aims for a greater than 10-fold improvement in sensitivity over G2-Xe experiments like LZ [62]. We assume that the NR/ER discrimination power and NR and ER analysis windows are identical to those of LZ. However, as the project is still in the early stages of development, we assume a slight improvement in the energy threshold for the combined NR+ER analysis. The lowest energy analysis of S2 signals in LXe to-date has succeeded in measuring energies as low as $0.3\,keV_{nr}$ [296]. We set our low energy threshold for DARWIN at twice this value. Backgrounds are taken from [293], and are extended to our required energy window using the same method described for G2-Xe.

G3-Ar The final detector setup we consider is G3-Ar, a liquid argon detector based on DarkSide-20k [64]. The quoted threshold for which NR/ER discrimination is possible is too large to allow any NR analysis of solar neutrino scattering, so we do not perform this analysis. The DarkSide-50 experiment achieved an S2-only threshold of $0.6\,keV_{nr}$, which we take as our threshold in the NR+ER analysis. We take our backgrounds from DarkSide-50 [297], although it is possible that some improvements will be made before DarkSide-20k is complete.

For each of these experimental setups, the projected sensitivity was calculated at the 90% CL, assuming no signals of new physics were observed. As in Chapter 6, the ER only analyses were most sensitive to mediator masses below 1 MeV. The best limits on our region of interest were therefore obtained from the NR, or NR+ER analyses. As I did not perform the calculations of these sensitivities myself, I will not discuss the process by which they were derived in detail. Instead, I will move onto the results and what they mean for the future of the $U(1)_{L_\mu - L_\tau}$ parameter space.

7.3   The future of the $U(1)_{L_\mu - L_\tau}$ parameter space

The projected sensitivities of each of the future DD experiments summarised in Table 7.1 are shown in Figure 7.8. In each case, we have taken the lower envelope of the sensitivity curves obtained in the NR, ER, and NR+ER analyses.

From Figure 7.8, we immediately see that SuperCDMS SNOLAB will not be able to probe new regions of the $U(1)_{L_\mu - L_\tau}$ parameter space. Of the various experimental setups considered for SuperCDMS in Table 7.1, the greatest sensitivity was obtained from the NR analysis of the iZIP configuration and the NR+ER analysis of the HV mode. As we predicted in Chapter 5, a study of CEνNS at SuperCDMS SNOLAB will not be able to outperform previous analyses on the $U(1)_{L_\mu - L_\tau}$ parameter space, and as our results in Chapter 6 demonstrated, the inclusion of ER events will not significantly improve the sensitivity within our preferred mass range. This result, then, is consistent with our earlier work, and supports the use of the neutrino contour in Figure 5.5 as a tool for estimating the sensitivity of DD experiments to non-DM parameter spaces. We found that the most limiting background in our analysis was the NR background generated from ^{206}Pb decays. Reducing this background should therefore be a priority if the SuperCDMS collaboration wishes to place competitive constraints on models involving new light mediators in the neutrino sector.

Similarly, we see that DarkSide-20k will also not be able to probe the unconstrained $U(1)_{L_\mu - L_\tau}$ parameter space. The line shown in Figure 7.8 is entirely due to the NR+ER analysis, as in the analysis including NR/ER discrimination the energy threshold was too high to see solar neutrino scattering through CEνNS.

For future LXe detectors, however, the prospects are far more promising. We predict that LZ, an experiment that is already beginning to collect data, will be able to constrain currently unexplored regions of the $U(1)_{L_\mu - L_\tau}$ parameter space. The projected reach of the detector covers most of the region where the preferred bands of $(g-2)_\mu$ and H_0 overlap, allowing us to test the possibility of a simultaneous solution to two physics mysteries. The results for DARWIN, which will operate using similar
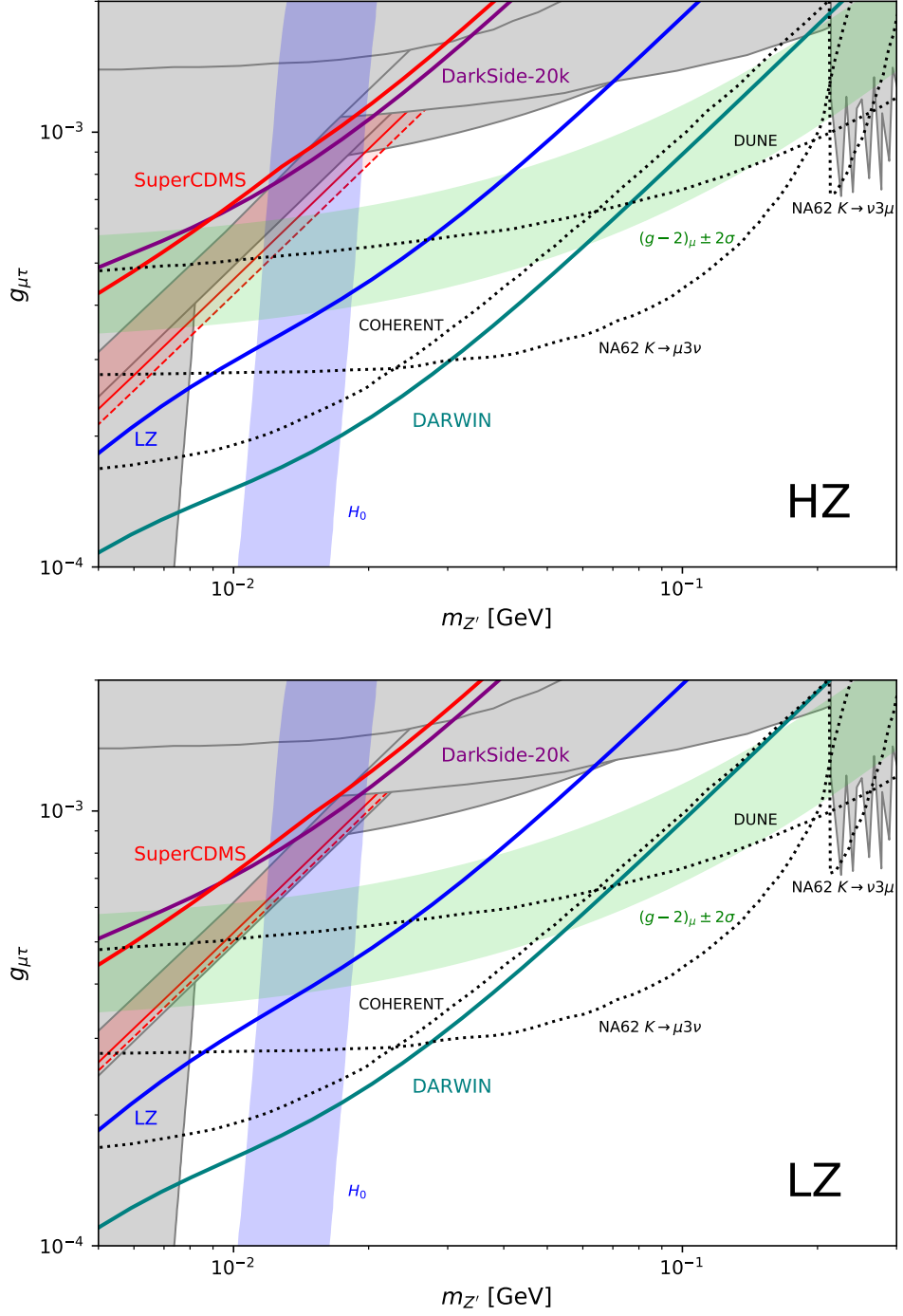
Figure 7.8: Projected sensitivities of future direct detection experiments (solid, thick) and other future experiments (dotted, black) to the parameter space of a $U(1)_{L_\mu-L_\tau}$ gauge boson. Existing constraints are shown in grey, while the shaded bands represent the regions favoured by $U(1)_{L_\mu-L_\tau}$ solutions to the muon $g-2$ and H_0 tensions.

technology to LZ but with a larger target mass, are predictably an improvement over the G2 detector. DARWIN's projected sensitivity covers the majority of the currently explored $(g-2)_\mu$ preferred region.

However, DARWIN is not expected to begin taking data for several years, and it will have competition from other upcoming experiments. Alongside the projections for future DD experiments, we show the projected sensitivities of three other upcoming experiments which have been previously calculated. These include a hypothetical upgrade of COHERENT with a 10 ton year exposure [298], searches for neutrino trident production at DUNE [299,300], and studies of kaon decays at NA62 [301]. The latter of these has the potential to probe the entire region favoured by a $U(1)_{L_\mu - L_\tau}$ explanation of the muon $g-2$ anomaly, and, if the required dedicated single muon trigger can be achieved, is likely to present results much sooner than DARWIN.

The results presented in Figure 7.8 for the HZ and LZ SSMs are qualitatively the same. The projected sensitivity curves for the four DD experiments are all slightly weaker in the LZ case, but the existing constraints from Borexino are affected more, since they depend on the ^{7}Be rather than the ^{8}B neutrino flux. The result is that in the low-metallicity scenario, more of the overlap region between the $(g-2)_\mu$ and H_0 bands is currently available to be constrained by future LXe experiments.

Studying the prospects of the four DD experiments collectively, we see that the optimal strategy for constraining the $U(1)_{L_\mu - L_\tau}$ parameter space with DD experiments is to search for coherent elastic neutrino-nucleus scattering with the largest exposure possible. Between experiments whose energy thresholds are sufficiently low to observe part of the CEνNS spectrum, those that have focused on maximising exposure, like LZ, outperform those that have additional sensitivity to low energy recoils, like SuperCDMS. For these experiments, the NR channel provides the strongest constraints. Electron recoils only provide significant improvements at mediator masses that are already well constrained, and the benefit gained by the slightly lower thresholds of the NR+ER analyses are in general outweighed by the additional backgrounds of the ER channel.

In the long term, the entire muon $g - 2$ favoured region of the parameter space is likely to be explored by other experiments, such as NA62, before G3 DD experiments like DARWIN are complete. Should a signal of new physics be seen by one of these experiments, though, data from DD experiments could provide important complementary information to test a $U(1)_{L_\mu - L_\tau}$ interpretation of their results.

Chapter 8

Conclusions

As direct detection (DD) experiments continue to increase in scale, they will eventually become sensitive to the interactions of solar neutrinos via coherent elastic neutrino-nucleus scattering (CEνNS). This is a known consequence of SM physics, and CEνNS will ultimately form a major obstacle to searches for dark matter (DM) candidates with very small scattering cross sections. However, in the presence of certain models of new physics, the neutrino scattering rate can be modified, and signals of CEνNS may appear in DD analyses sooner than expected.

In this thesis, we have explored the effects of new physics on neutrino scattering at DD experiments. We chose to study four simplified models that introduce new light mediators which interact with SM fermions. These models were discussed in Chapter 4, and include two vector models, the $U(1)_{B-L}$ and $U(1)_{L_\mu - L_\tau}$, and two scalar models, one lepton number violating (LNV) and the other lepton number conserving (LNC). In Chapter 5, we introduced the neutrino contour, a method of projecting the effects of new physics onto the parameter space of a canonical weakly interacting massive particle (WIMP). The contour represents the earliest point at which a given model could generate observable effects in DD experiments, based on existing constraints on the model. This has two significant implications for future DD experiments: one positive, and one negative.

Clearly, an enhanced rate of neutrino scattering would further limit the DM dis-

covery potential of future experiments. Additionally, as the CEνNS spectrum can closely resemble the spectrum of a canonical WIMP, the signature of some previously unknown new physics at a DD experiment could be naïvely interpreted as a signal of DM. The neutrino contour delineates the region of the WIMP parameter space within which an apparent WIMP signal could be mimicked by new physics affecting the CEνNS rate.

If, however, a DD experiment is sensitive to the WIMP parameter space below the neutrino contour and does not see any signals of new physics, this would indicate that it could constrain not only the properties of DM, but also the relevant model of new physics interacting in the neutrino sector. The neutrino contour therefore provides an immediate indication of the sensitivity of a DD experiment to models of new neutrino physics, based on its sensitivity to the canonical WIMP parameter space. In Figure 5.5, we compared the level of the neutrino contour in our two vector models with some past and future DD experiments. For these models, only LUX-ZEPLIN (LZ) appeared to have any sensitivity to the WIMP parameter space below the neutrino contour, indicating that it is a good candidate for placing competitive constraints on those simplified models.

In Figure 5.6 we see that for the two scalar models we considered, the maximum level of the neutrino contour depends heavily on our interpretation of constraints that were previously derived from supernova physics. These constraints relied on the computation of the mean free path of neutrinos within a supernova, as a large modification to this value could conflict with observations of the neutrino burst from SN 1987A. However, earlier analyses had made many simplifying assumptions that warranted further examination. We improved on these analysis in several ways, most significantly by including the effects of the temperature and density of the supernova core when computing the neutrino scattering cross section. The resulting constraints are significantly weaker than those previously calculated, and we argue that one of the limits quoted in an earlier work should not be considered a true constraint on the model of new physics. This means that in the presence of an LNV scalar, the

CEνNS rate could be enhanced by up to five orders of magnitude at low energies.

Our analysis of the neutrino contour was based solely on the effects of new physics on the rate of CEνNS. However, experiments such as CDMSlite could also be sensitive to modifications of the neutrino-electron scattering rate. Chapter 6 described our efforts to derive constraints on the $U(1)_{B-L}$ parameter space using data from CDMSlite. Although the constraints were not expected to be competitive with other experiments, the analysis would act as proof-of-concept for future analyses at Super-CDMS SNOLAB. Including neutrino-electron scattering in our analysis introduced several new challenges, some of which we have not yet resolved. In particular, our expressions for the scattering rate assume that the initial and final states of the electron are plane waves, as would be the case for free particles. In a semiconductor crystal, like the germanium crystals used by CDMSlite, this is not the case, and the free electron approximation is expected to lose accuracy at scattering energies below 1 keV. However, our simplified analysis indicated that neutrino-electron scattering is not the optimal channel for studying our models of new physics at DD experiments, and so the approximation will not affect our conclusions about the ability of DD experiments to probe new neutrino physics.

Finally, in Chapter 7 we examined in detail the prospects of using DD experiments to study the $U(1)_{L_\mu - L_\tau}$ model. This model is of particular relevance as it has the potential to resolve two ongoing problems in fundamental physics: the muon g-2 anomaly and the H_0 tension. A reevaluation of earlier constraints from Borexino found that its results are more constraining than previously calculated, but confirmed that a simultaneous resolution of both anomalies is still allowed by current constraints on the model. We calculated the sensitivity of four future DD experiments to the $U(1)_{L_\mu - L_\tau}$ parameter space. These sensitivities are shown, alongside projections for other upcoming experiments, in Figure 7.8. As we expected from the results of Chapter 5, LZ will be able to set constraints that are competitive with previous experiments, and we expect that it will be able to test almost the entire region favoured by a simultaneous explanation of the muon g-2 and H_0 tensions.

SuperCDMS SNOLAB, which has a lower energy threshold than LZ but $< 1\%$ of the exposure, will not be able to probe any unexplored regions of the parameter space. Nor will DarkSide-20k, a next-to-next generation liquid argon experiment. Although it has a significantly larger exposure than LZ, its energy threshold lies above the maximum energy that can be deposited by solar neutrinos through CEνNS. DAR-WIN, a proposed successor to LZ, will probe the majority of the region favoured by solutions of the muon g-2 anomaly, though this task is likely to be achieved sooner by other neutrino experiments.

In summary, we have assessed the ability of DD experiments to explore certain simplified models of new physics through neutrino scattering. Our work indicates that they can indeed provide valuable information about the presence of new light mediators that is complementary to other searches, including those at dedicated neutrino detectors. We believe that an optimal strategy for improving the reach of DD experiments to these models of new physics is to maximise detector exposure, while ensuring the minimum energy threshold is low enough to detect at least part of the spectrum of CEνNS from solar neutrinos. Our results are consistent with our interpretation of the neutrino contour, indicating that a projection of the neutrino scattering rate onto a DM parameter space can be a useful tool for estimating the sensitivity of DD experiments to models of new physics that would affect the rate of CEνNS.

Bibliography

[1] D. G. Cerdeño, A. Cheek, E. Reid and H. Schulz, *Surrogate Models for Direct Dark Matter Detection*, *JCAP* **08** (2018) 011, [1802.03174].

[2] C. Bœhm, D. G. Cerdeño, P. A. N. Machado, A. Olivares-Del Campo, E. Perdomo and E. Reid, *How high is the neutrino floor?*, *JCAP* **01** (2019) 043, [1809.06385].

[3] D. W. P. d. Amaral, D. G. Cerdeno, P. Foldenauer and E. Reid, *Solar neutrino probes of the muon anomalous magnetic moment in the gauged* $\mathrm{U}(1)_{L_\mu - L_\tau}$, *JHEP* **12** (2020) 155, [2006.11225].

[4] D. G. Cerdeño, M. Cermeño, M. A. Pérez-García and E. Reid, *Medium effects in supernovae constraints on light mediators*, 2106.11660.

[5] M. E. Peskin and D. V. Schroeder, *An Introduction to quantum field theory*. Addison-Wesley, Reading, USA, 1995.

[6] M. D. Schwartz, *Quantum Field Theory and the Standard Model*. Cambridge University Press, 3, 2014.

[7] M. Srednicki, *Quantum field theory*. Cambridge University Press, 1, 2007.

[8] G. Bertone, D. Hooper and J. Silk, *Particle dark matter: Evidence, candidates and constraints*, *Phys. Rept.* **405** (2005) 279–390, [hep-ph/0404175].

[9] V. Trimble, *Existence and nature of dark matter in the universe*, *Annual Review of Astronomy and Astrophysics* **25** (1987) 425–472.

[10] K. Garrett and G. Duda, *Dark Matter: A Primer*, *Adv. Astron.* **2011** (2011) 968283, [1006.2483].

[11] PLANCK collaboration, N. Aghanim et al., *Planck 2018 results. VI. Cosmological parameters*, *Astron. Astrophys.* **641** (2020) A6, [1807.06209].

[12] F. Governato, B. Willman, L. Mayer, A. Brooks, G. Stinson, O. Valenzuela et al., *Forming disk galaxies in lambda-cdm simulations*, *Mon. Not. Roy. Astron. Soc.* **374** (2007) 1479–1494, [astro-ph/0602351].

[13] M. S. Seigar and J. Berrier, *Galaxy Rotation Curves in the Context of LambdaCDM Cosmology*. 2011. 10.5772/22992.

[14] M. Schumann, *Direct Detection of WIMP Dark Matter: Concepts and Status*, *J. Phys. G* **46** (2019) 103003, [1903.03026].

[15] C. Pérez de los Heros, *Status, Challenges and Directions in Indirect Dark Matter Searches*, *Symmetry* **12** (2020) 1648, [2008.11561].

[16] A. Ringwald, *Exploring the Role of Axions and Other WISPs in the Dark Universe*, *Phys. Dark Univ.* **1** (2012) 116–135, [1210.5081].

[17] L. Badurina et al., *AION: An Atom Interferometer Observatory and Network*, *JCAP* **05** (2020) 011, [1911.11755].

[18] K. Griest, *The Search for dark matter: WIMPs and MACHOs*, *Annals N. Y. Acad. Sci.* **688** (1993) 390, [hep-ph/9303253].

[19] P. Villanueva-Domingo, O. Mena and S. Palomares-Ruiz, *A brief review on primordial black holes as dark matter*, 3, 2021, 2103.12087.

[20] A. Boveia and C. Doglioni, *Dark Matter Searches at Colliders*, *Ann. Rev. Nucl. Part. Sci.* **68** (2018) 429–459, [1810.12238].

[21] A. D. Dolgov, *Cosmological implications of neutrinos*, *Surveys High Energ. Phys.* **17** (2002) 91–114, [hep-ph/0208222].

[22] IceCube collaboration, M. G. Aartsen et al., *Detection of a particle shower at the Glashow resonance with IceCube*, Nature **591** (2021) 220–224.

[23] D. Bödeker and W. Buchmüller, *Baryogenesis from the weak scale to the grand unification scale*, `2009.07294`.

[24] B. W. Lee and S. Weinberg, *Cosmological Lower Bound on Heavy Neutrino Masses*, Phys. Rev. Lett. **39** (1977) 165–168.

[25] G. Gelmini and P. Gondolo, *DM production mechanisms*, p. 121141. Cambridge University Press, 2010. 10.1017/CBO9780511770739.008.

[26] S. Dodelson, E. I. Gates and M. S. Turner, *Cold dark matter models*, Science **274** (1996) 69–75, [`astro-ph/9603081`].

[27] G. Jungman, M. Kamionkowski and K. Griest, *Supersymmetric dark matter*, Phys. Rept. **267** (1996) 195–373, [`hep-ph/9506380`].

[28] E. W. Kolb and K. A. Olive, *The Lee-Weinberg Bound Revisited*, Phys. Rev. D **33** (1986) 1202.

[29] K. Griest and M. Kamionkowski, *Unitarity Limits on the Mass and Radius of Dark Matter Particles*, Phys. Rev. Lett. **64** (1990) 615.

[30] C. Boehm and P. Fayet, *Scalar dark matter candidates*, Nucl. Phys. B **683** (2004) 219–263, [`hep-ph/0305261`].

[31] A. Poulin, *Dark matter freeze-out in modified cosmological scenarios*, Phys. Rev. D **100** (2019) 043022, [`1905.03126`].

[32] D. G. Cerdeño and A. M. Green, *Direct detection of WIMPs*, p. 347369. Cambridge University Press, 2010. 10.1017/CBO9780511770739.018.

[33] M. Drees and F. Hajkarim, *Neutralino Dark Matter in Scenarios with Early Matter Domination*, JHEP **12** (2018) 042, [`1808.05706`].

[34] A. Aboubrahim, W.-Z. Feng and P. Nath, *Expanding the parameter space of natural supersymmetry*, *JHEP* **04** (2020) 144, [2003.02267].

[35] J. Read, *The Local Dark Matter Density*, *J. Phys. G* **41** (2014) 063101, [1404.1938].

[36] M. Gonzalez-Garcia, M. Maltoni, Y. F. Perez-Gonzalez and R. Zukanovich Funchal, *Neutrino Discovery Limit of Dark Matter Direct Detection Experiments in the Presence of Non-Standard Interactions*, *JHEP* **07** (2018) 019, [1803.03650].

[37] J. Lewin and P. Smith, *Review of mathematics, numerical factors, and corrections for dark matter experiments based on elastic nuclear recoil*, *Astropart. Phys.* **6** (1996) 87–112.

[38] J. Billard, L. Strigari and E. Figueroa-Feliciano, *Implication of neutrino backgrounds on the reach of next generation dark matter direct detection experiments*, *Phys. Rev. D* **89** (2014) 023524, [1307.5458].

[39] R. H. Helm, *Inelastic and Elastic Scattering of 187-Mev Electrons from Selected Even-Even Nuclei*, *Phys. Rev.* **104** (1956) 1466–1475.

[40] A. M. Green, *Determining the WIMP mass using direct detection experiments*, *JCAP* **08** (2007) 022, [hep-ph/0703217].

[41] P. F. de Salas, *Dark matter local density determination based on recent observations*, *J. Phys. Conf. Ser.* **1468** (2020) 012020, [1910.14366].

[42] M. Fairbairn, T. Douce and J. Swift, *Quantifying Astrophysical Uncertainties on Dark Matter Direct Detection Results*, *Astropart. Phys.* **47** (2013) 45–53, [1206.2693].

[43] C. W. Purcell, J. S. Bullock and M. Kaplinghat, *The Dark Disk of the Milky Way*, *Astrophys. J.* **703** (2009) 2275–2284, [0906.5348].

[44] V. Belokurov, D. Erkal, N. W. Evans, S. E. Koposov and A. J. Deason, *Co-formation of the disc and the stellar halo*, *Monthly Notices of the Royal Astronomical Society* **478** (06, 2018) 611–619, [https://academic.oup.com/mnras/article-pdf/478/1/611/25005885/sty982.pdf].

[45] N. W. Evans, C. A. O'Hare and C. McCabe, *Refinement of the standard halo model for dark matter searches in light of the Gaia Sausage*, *Phys. Rev. D* **99** (2019) 023012, [1810.11468].

[46] N. Bozorgnia, F. Calore, M. Schaller, M. Lovell, G. Bertone, C. S. Frenk et al., *Simulated Milky Way analogues: implications for dark matter direct searches*, *JCAP* **05** (2016) 024, [1601.04707].

[47] J. Binney and S. Tremaine, *Galactic dynamics*. 1987.

[48] S. Kang, S. Scopel, G. Tomar and J.-H. Yoon, *Present and projected sensitivities of Dark Matter direct detection experiments to effective WIMP-nucleus couplings*, *Astropart. Phys.* **109** (2019) 50–68, [1805.06113].

[49] R. Bernabei et al., *First model independent results from DAMA/LIBRA-phase2*, *Nucl. Phys. Atom. Energy* **19** (2018) 307–325, [1805.10486].

[50] J. Amare et al., *Annual Modulation Results from Three Years Exposure of ANAIS-112*, 2103.01175.

[51] D. Pinci, E. Di Marco, F. Renga, C. Voena, E. Baracchini, G. Mazzitelli et al., *Cygnus: development of a high resolution TPC for rare events*, *PoS* **EPS-HEP2017** (2017) 077.

[52] J. Street, R. Bunker, E. H. Miller, R. W. Schnee, S. Snyder and J. So, *Radon Mitigation for the SuperCDMS SNOLAB Dark Matter Experiment*, *AIP Conf. Proc.* **1921** (2018) 050002, [1708.08535].

[53] LZ collaboration, D. S. Akerib et al., *LUX-ZEPLIN (LZ) Conceptual Design Report*, 1509.02910.

[54] XENON collaboration, E. Aprile et al., *Physics reach of the XENON1T dark matter experiment*, *JCAP* **04** (2016) 027, [1512.07501].

[55] SuperCDMS collaboration, R. Agnese et al., *Projected Sensitivity of the SuperCDMS SNOLAB experiment*, *Phys. Rev. D* **95** (2017) 082002, [1610.00006].

[56] CRESST collaboration, A. H. Abdelhameed et al., *First results from the CRESST-III low-mass dark matter program*, *Phys. Rev. D* **100** (2019) 102002, [1904.00498].

[57] SuperCDMS collaboration, R. Agnese et al., *Results from the Super Cryogenic Dark Matter Search Experiment at Soudan*, *Phys. Rev. Lett.* **120** (2018) 061802, [1708.08869].

[58] SuperCDMS collaboration, R. Agnese et al., *Low-mass dark matter search with CDMSlite*, *Phys. Rev. D* **97** (2018) 022002, [1707.01632].

[59] XENON collaboration, E. Aprile et al., *Dark Matter Search Results from a One Ton-Year Exposure of XENON1T*, *Phys. Rev. Lett.* **121** (2018) 111302, [1805.12562].

[60] XENON collaboration, E. Aprile et al., *Excess electronic recoil events in XENON1T*, *Phys. Rev. D* **102** (2020) 072004, [2006.09721].

[61] B. J. Mount et al., *LUX-ZEPLIN (LZ) Technical Design Report*, 1703.09144.

[62] DARWIN collaboration, J. Aalbers et al., *DARWIN: towards the ultimate dark matter detector*, *JCAP* **11** (2016) 017, [1606.07001].

[63] DarkSide 20k collaboration, P. Agnes et al., *Sensitivity of future liquid argon dark matter search experiments to core-collapse supernova neutrinos*, 2011.07819.

[64] DARKSIDE-20K collaboration, C. E. Aalseth et al., *DarkSide-20k: A 20 tonne two-phase LAr TPC for direct dark matter detection at LNGS, Eur. Phys. J. Plus* **133** (2018) 131, [1707.08145].

[65] J. Menendez, D. Gazit and A. Schwenk, *Spin-dependent WIMP scattering off nuclei, Phys. Rev. D* **86** (2012) 103511, [1208.1094].

[66] J. Fan, M. Reece and L.-T. Wang, *Non-relativistic effective theory of dark matter direct detection, JCAP* **11** (2010) 042, [1008.1591].

[67] A. L. Fitzpatrick, W. Haxton, E. Katz, N. Lubbers and Y. Xu, *The Effective Field Theory of Dark Matter Direct Detection, JCAP* **02** (2013) 004, [1203.3542].

[68] J. B. Dent, L. M. Krauss, J. L. Newstead and S. Sabharwal, *General analysis of direct dark matter detection: From microphysics to observational signatures, Phys. Rev. D* **92** (2015) 063515, [1505.03117].

[69] N. Anand, A. L. Fitzpatrick and W. C. Haxton, *Weakly interacting massive particle-nucleus elastic scattering response, Phys. Rev. C* **89** (2014) 065501, [1308.6288].

[70] S. D. McDermott, H.-B. Yu and K. M. Zurek, *The Dark Matter Inverse Problem: Extracting Particle Physics from Scattering Events, Phys. Rev. D* **85** (2012) 123507, [1110.4281].

[71] C. Strege, R. Trotta, G. Bertone, A. H. G. Peter and P. Scott, *Fundamental statistical limitations of future dark matter direct detection experiments, Phys. Rev. D* **86** (2012) 023507, [1201.3631].

[72] C. McCabe, *The Astrophysical Uncertainties Of Dark Matter Direct Detection Experiments, Phys. Rev. D* **82** (2010) 023530, [1005.0579].

[73] D. G. Cerdeno, M. Fornasa, J. H. Huh and M. Peiro, *Nuclear uncertainties in the spin-dependent structure functions for direct dark matter detection, Phys. Rev. D* **87** (2013) 023512, [`1208.6426`].

[74] G. Bertone, D. G. Cerdeno, J. I. Collar and B. C. Odom, *WIMP identification through a combined measurement of axial and scalar couplings, Phys. Rev. Lett.* **99** (2007) 151301, [`0705.2502`].

[75] M. Pato, L. Baudis, G. Bertone, R. Ruiz de Austri, L. E. Strigari and R. Trotta, *Complementarity of Dark Matter Direct Detection Targets, Phys. Rev. D* **83** (2011) 083505, [`1012.3458`].

[76] D. G. Cerdeño et al., *Complementarity of dark matter direct detection: the role of bolometric targets, JCAP* **07** (2013) 028, [`1304.1758`].

[77] H. Rogers, D. G. Cerdeno, P. Cushman, F. Livet and V. Mandic, *Multidimensional effective field theory analysis for direct detection of dark matter, Phys. Rev. D* **95** (2017) 082003, [`1612.09038`].

[78] N. Bernal, A. Goudelis, Y. Mambrini and C. Munoz, *Determining the WIMP mass using the complementarity between direct and indirect searches and the ILC, JCAP* **0901** (2009) 046, [`0804.1976`].

[79] G. Bertone, D. G. Cerdeno, M. Fornasa, R. Ruiz de Austri and R. Trotta, *Identification of Dark Matter particles with LHC and direct detection data, Phys. Rev.* **D82** (2010) 055008, [`1005.4280`].

[80] G. Bertone, D. G. Cerdeno, M. Fornasa, L. Pieri, R. Ruiz de Austri and R. Trotta, *Complementarity of Indirect and Accelerator Dark Matter Searches, Phys. Rev.* **D85** (2012) 055014, [`1111.2607`].

[81] M. T. Frandsen, F. Kahlhoefer, A. Preston, S. Sarkar and K. Schmidt-Hoberg, *LHC and Tevatron Bounds on the Dark Matter Direct Detection Cross-Section for Vector Mediators, JHEP* **07** (2012) 123, [`1204.3839`].

[82] Y. Mambrini, M. H. G. Tytgat, G. Zaharijas and B. Zaldivar, *Complementarity of Galactic radio and collider data in constraining WIMP dark matter models*, *JCAP* **1211** (2012) 038, [1206.2352].

[83] A. Arbey, M. Battaglia and F. Mahmoudi, *Combining monojet, supersymmetry, and dark matter searches*, *Phys. Rev.* **D89** (2014) 077701, [1311.7641].

[84] S. Liem, G. Bertone, F. Calore, R. Ruiz de Austri, T. M. P. Tait, R. Trotta et al., *Effective field theory of dark matter: a global analysis*, *JHEP* **09** (2016) 077, [1603.05994].

[85] S. Baum, R. Catena, J. Conrad, K. Freese and M. B. Krauss, *Determining dark matter properties with a XENONnT/LZ signal and LHC Run 3 monojet searches*, *Phys. Rev.* **D97** (2018) 083002, [1709.06051].

[86] G. Bertone, N. Bozorgnia, J. S. Kim, S. Liem, C. McCabe, S. Otten et al., *Identifying WIMP dark matter from particle and astroparticle data*, *JCAP* **1803** (2018) 026, [1712.04793].

[87] A. Buckley, H. Hoeth, H. Lacker, H. Schulz and J. E. von Seggern, *Systematic event generator tuning for the LHC*, *Eur. Phys. J. C* **65** (2010) 331–357, [0907.2973].

[88] F. Feroz and M. P. Hobson, *Multimodal nested sampling: an efficient and robust alternative to MCMC methods for astronomical data analysis*, *Mon. Not. Roy. Astron. Soc.* **384** (2008) 449, [0704.3704].

[89] F. Feroz, M. P. Hobson and M. Bridges, *MultiNest: an efficient and robust Bayesian inference tool for cosmology and particle physics*, *Mon. Not. Roy. Astron. Soc.* **398** (2009) 1601–1614, [0809.3437].

[90] DELPHI collaboration, P. Abreu et al., *Tuning and test of fragmentation models based on identified particles and precision event shape data, Z. Phys. C* **73** (1996) 11–60.

[91] A. Buckley, C. Englert, J. Ferrando, D. J. Miller, L. Moore, M. Russell et al., *Constraining top quark effective theory in the LHC Run II era, JHEP* **04** (2016) 015, [1512.03360].

[92] C. Englert, R. Kogler, H. Schulz and M. Spannowsky, *Higgs coupling measurements at the LHC, Eur. Phys. J. C* **76** (2016) 393, [1511.05170].

[93] P. Hernandez, *Neutrino Physics*, in *8th CERN–Latin-American School of High-Energy Physics*, pp. 85–142, 2016, 1708.01046, DOI.

[94] A. J. Lowe, *Neutrino Physics and The Solar Neutrino Problem*, 0907.3658.

[95] W. Pauli, *Dear radioactive ladies and gentlemen, Phys. Today* **31N9** (1978) 27.

[96] H. Bethe and R. Peierls, *The 'neutrino', Nature* **133** (1934) 532.

[97] B. Pontecorvo, *Inverse beta process, Camb. Monogr. Part. Phys. Nucl. Phys. Cosmol.* **1** (1991) 25–31.

[98] F. Reines and C. L. Cowan, *The neutrino, Nature* **178** (1956) 446–449.

[99] C. L. Cowan, F. Reines, F. B. Harrison, H. W. Kruse and A. D. McGuire, *Detection of the free neutrino: A Confirmation, Science* **124** (1956) 103–104.

[100] L. D. Landau, *On the conservation laws for weak interactions, Nucl. Phys.* **3** (1957) 127–131.

[101] G. Feinberg, *Decays of the mu Meson in the Intermediate-Meson Theory, Phys. Rev.* **110** (1958) 1482–1483.

[102] G. Danby, J. M. Gaillard, K. A. Goulianos, L. M. Lederman, N. B. Mistry, M. Schwartz et al., *Observation of High-Energy Neutrino Reactions and the Existence of Two Kinds of Neutrinos*, *Phys. Rev. Lett.* **9** (1962) 36–44.

[103] S. E. Kopp, *Accelerator-based neutrino beams*, *Phys. Rept.* **439** (2007) 101–159, [`physics/0609129`].

[104] R. Davis, *A review of the Homestake solar neutrino experiment*, *Prog. Part. Nucl. Phys.* **32** (1994) 13–32.

[105] J. N. Bahcall, *Solar neutrino cross sections and nuclear beta decay*, *Phys. Rev.* **135** (1964) B137–B146.

[106] R. Davis, Jr., D. S. Harmer and K. C. Hoffman, *Search for neutrinos from the sun*, *Phys. Rev. Lett.* **20** (1968) 1205–1209.

[107] E. G. Adelberger et al., *Solar fusion cross sections II: the pp chain and CNO cycles*, *Rev. Mod. Phys.* **83** (2011) 195, [`1004.2318`].

[108] K. S. Krane, *Introductory nuclear physics.* Wiley, New York, NY, 1988.

[109] A. Gallo Rosso, C. Mascaretti, A. Palladino and F. Vissani, *Introduction to neutrino astronomy*, *Eur. Phys. J. Plus* **133** (2018) 267, [`1806.06339`].

[110] S. Basu and H. M. Antia, *Constraining solar abundances using helioseismology*, *Astrophys. J. Lett.* **606** (2004) L85, [`astro-ph/0403485`].

[111] M. Asplund, N. Grevesse, A. J. Sauval and P. Scott, *The Chemical Composition of the Sun*, *ARAA* **47** (Sept., 2009) 481–522, [`0909.0948`].

[112] J. N. Bahcall, S. Basu, M. Pinsonneault and A. M. Serenelli, *Helioseismological implications of recent solar abundance determinations*, *Astrophys. J.* **618** (2005) 1049–1056, [`astro-ph/0407060`].

[113] S. Basu and H. M. Antia, *Helioseismology and Solar Abundances*, *Phys. Rept.* **457** (2008) 217–283, [`0711.4590`].

[114] A. Serenelli, S. Basu, J. W. Ferguson and M. Asplund, *New Solar Composition: The Problem With Solar Models Revisited, Astrophys. J. Lett.* **705** (2009) L123–L127, [`0909.2668`].

[115] N. Vinyoles, A. M. Serenelli, F. L. Villante, S. Basu, J. Bergström, M. C. Gonzalez-Garcia et al., *A new Generation of Standard Solar Models, Astrophys. J.* **835** (2017) 202, [`1611.09867`].

[116] J. N. Bahcall, N. A. Bahcall and G. Shaviv, *Present status of the theoretical predictions for the Cl-37 solar neutrino experiment, Phys. Rev. Lett.* **20** (1968) 1209–1212.

[117] J. N. Bahcall and R. Davis, *Solar Neutrinos - a Scientific Puzzle, Science* **191** (1976) 264–267.

[118] W. C. Haxton, *The solar neutrino problem, Ann. Rev. Astron. Astrophys.* **33** (1995) 459–503, [`hep-ph/9503430`].

[119] Kamiokande-II collaboration, K. S. Hirata et al., *Observation of B-8 Solar Neutrinos in the Kamiokande-II Detector, Phys. Rev. Lett.* **63** (1989) 16.

[120] A. I. Abazov et al., *First results from the Soviet-American gallium experiment, Nucl. Phys. B Proc. Suppl.* **19** (1991) 84–93.

[121] GALLEX collaboration, R. Wink et al., *The Status of GALLEX, Nucl. Phys. B Proc. Suppl.* **19** (1991) 77–83.

[122] J. N. Bahcall and H. A. Bethe, *Do solar neutrino experiments imply new physics?, Phys. Rev. D* **47** (1993) 1298–1301, [`hep-ph/9212204`].

[123] J. N. Bahcall and R. K. Ulrich, *Solar Models, Neutrino Experiments and Helioseismology, Rev. Mod. Phys.* **60** (1988) 297–372.

[124] K. S. Hirata et al., *Observation in the Kamiokande-II Detector of the Neutrino Burst from Supernova SN 1987a, Phys. Rev. D* **38** (1988) 448–458.

[125] R. M. Bionta et al., *Observation of a Neutrino Burst in Coincidence with Supernova SN 1987a in the Large Magellanic Cloud*, Phys. Rev. Lett. **58** (1987) 1494.

[126] E. N. Alekseev, L. N. Alekseeva, V. I. Volchenko and I. V. Krivosheina, *Possible Detection of a Neutrino Signal on 23 February 1987 at the Baksan Underground Scintillation Telescope of the Institute of Nuclear Research*, JETP Lett. **45** (1987) 589–592.

[127] S. M. Bilenky and S. T. Petcov, *Massive Neutrinos and Neutrino Oscillations*, Rev. Mod. Phys. **59** (1987) 671.

[128] S. Bilenky, *Neutrino oscillations: From a historical perspective to the present status*, Nucl. Phys. B **908** (2016) 2–13, [`1602.00170`].

[129] A. Y. Smirnov, *The MSW effect and matter effects in neutrino oscillations*, Phys. Scripta T **121** (2005) 57–64, [`hep-ph/0412391`].

[130] S. M. Bilenky, *Some comments on high precision study of neutrino oscillations*, Phys. Part. Nucl. Lett. **12** (2015) 453–461, [`1502.06158`].

[131] L. Okun and B. Pontecorvo, *Some remarks on slow processes of transformation of elementary particles*, Zh. Eksp. Teor. Fiz. **32** (1957) 1587–1588.

[132] B. Pontecorvo, *Mesonium and anti-mesonium*, Sov. Phys. JETP **6** (1957) 429.

[133] B. Pontecorvo, *Neutrino Experiments and the Problem of Conservation of Leptonic Charge*, Sov. Phys. JETP **26** (1968) 984–988.

[134] Z. Maki, M. Nakagawa and S. Sakata, *Remarks on the unified model of elementary particles*, Prog. Theor. Phys. **28** (1962) 870–880.

[135] S. M. Bilenky and B. Pontecorvo, *Lepton Mixing and Neutrino Oscillations*, Phys. Rept. **41** (1978) 225–261.

[136] J. N. Bahcall, B. T. Cleveland, R. Davis, Jr. and J. K. Rowley, *Chlorine and Gallium Solar Neutrino Experiments*, *Astrophys. J. Lett.* **292** (1985) L79–L82.

[137] S. L. Glashow and L. M. Krauss, *'Just SO' Neutrino Oscillations*, *Phys. Lett. B* **190** (1987) 199–207.

[138] L. Wolfenstein, *Neutrino Oscillations in Matter*, *Phys. Rev. D* **17** (1978) 2369–2374.

[139] S. P. Mikheyev and A. Y. Smirnov, *Resonance Amplification of Oscillations in Matter and Spectroscopy of Solar Neutrinos*, *Sov. J. Nucl. Phys.* **42** (1985) 913–917.

[140] A. Y. Smirnov, *The Mikheyev-Smirnov-Wolfenstein (MSW) Effect*, in *International Conference on History of the Neutrino: 1930-2018*, 2019, `1901.11473`.

[141] Super-Kamiokande collaboration, Y. Fukuda et al., *Measurement of the solar neutrino energy spectrum using neutrino electron scattering*, *Phys. Rev. Lett.* **82** (1999) 2430–2434, [`hep-ex/9812011`].

[142] SNO collaboration, Q. R. Ahmad et al., *Direct evidence for neutrino flavor transformation from neutral current interactions in the Sudbury Neutrino Observatory*, *Phys. Rev. Lett.* **89** (2002) 011301, [`nucl-ex/0204008`].

[143] L. Wolfenstein, *Oscillations Among Three Neutrino Types and CP Violation*, *Phys. Rev. D* **18** (1978) 958–960.

[144] DONUT collaboration, K. Kodama et al., *Observation of tau neutrino interactions*, *Phys. Lett. B* **504** (2001) 218–224, [`hep-ex/0012035`].

[145] C. Giganti, S. Lavignac and M. Zito, *Neutrino oscillations: The rise of the PMNS paradigm*, *Prog. Part. Nucl. Phys.* **98** (2018) 1–54, [`1710.00715`].

[146] Daya Bay collaboration, D. Adey et al., *Measurement of the Electron Antineutrino Oscillation with 1958 Days of Operation at Daya Bay, Phys. Rev. Lett.* **121** (2018) 241805, [1809.02261].

[147] RENO collaboration, G. Bak et al., *Measurement of Reactor Antineutrino Oscillation Amplitude and Frequency at RENO, Phys. Rev. Lett.* **121** (2018) 201801, [1806.00248].

[148] Double Chooz collaboration, Y. Abe et al., *Improved measurements of the neutrino mixing angle θ_{13} with the Double Chooz detector, JHEP* **10** (2014) 086, [1406.7763].

[149] MINOS collaboration, P. Adamson et al., *Measurement of Neutrino and Antineutrino Oscillations Using Beam and Atmospheric Data in MINOS, Phys. Rev. Lett.* **110** (2013) 251801, [1304.6335].

[150] T2K collaboration, K. Abe et al., *Measurement of neutrino and antineutrino oscillations by the T2K experiment including a new additional sample of ν_e interactions at the far detector, Phys. Rev. D* **96** (2017) 092006, [1707.01048].

[151] NOvA collaboration, M. A. Acero et al., *New constraints on oscillation parameters from ν_e appearance and ν_μ disappearance in the NOvA experiment, Phys. Rev. D* **98** (2018) 032012, [1806.00096].

[152] IceCube collaboration, M. G. Aartsen et al., *Measurement of Atmospheric Neutrino Oscillations at 6–56 GeV with IceCube DeepCore, Phys. Rev. Lett.* **120** (2018) 071801, [1707.07081].

[153] Super-Kamiokande collaboration, K. Abe et al., *Atmospheric neutrino oscillation analysis with external constraints in Super-Kamiokande I-IV, Phys. Rev. D* **97** (2018) 072001, [1710.09126].

[154] Super-Kamiokande collaboration, K. Abe et al., *Solar neutrino results in Super-Kamiokande-III, Phys. Rev. D* **83** (2011) 052010, [1010.0118].

[155] Borexino collaboration, M. Agostini et al., *First Simultaneous Precision Spectroscopy of pp, ^{7}Be, and pep Solar Neutrinos with Borexino Phase-II, Phys. Rev. D* **100** (2019) 082004, [1707.09279].

[156] I. Esteban, M. C. Gonzalez-Garcia, A. Hernandez-Cabezudo, M. Maltoni and T. Schwetz, *Global analysis of three-flavour neutrino oscillations: synergies and tensions in the determination of θ_{23}, δ_{CP}, and the mass ordering, JHEP* **01** (2019) 106, [1811.05487].

[157] S. Dodelson and L. M. Widrow, *Sterile-neutrinos as dark matter, Phys. Rev. Lett.* **72** (1994) 17–20, [hep-ph/9303287].

[158] M. Lattanzi and M. Gerbino, *Status of neutrino properties and future prospects - Cosmological and astrophysical constraints, Front. in Phys.* **5** (2018) 70, [1712.07109].

[159] C. Giunti and K. C. Wook, *Fundamentals of Neutrino Physics and Astrophysics.* Oxford Univ., Oxford, 2007, 10.1093/acprof:oso/9780198508717.001.0001.

[160] S. F. King, *Neutrino mass models, Rept. Prog. Phys.* **67** (2004) 107–158, [hep-ph/0310204].

[161] Y. Cai, T. Han, T. Li and R. Ruiz, *Lepton Number Violation: Seesaw Models and Their Collider Tests, Front. in Phys.* **6** (2018) 40, [1711.02180].

[162] M. J. Dolinski, A. W. P. Poon and W. Rodejohann, *Neutrinoless Double-Beta Decay: Status and Prospects, Ann. Rev. Nucl. Part. Sci.* **69** (2019) 219–251, [1902.04097].

[163] J. D. Vergados, H. Ejiri and F. Simkovic, *Theory of Neutrinoless Double Beta Decay, Rept. Prog. Phys.* **75** (2012) 106301, [1205.0649].

[164] V. A. Bednyakov and D. V. Naumov, *On coherent neutrino and antineutrino scattering off nuclei, Phys. Part. Nucl. Lett.* **16** (2019) 638–646, [1904.03119].

[165] D. Z. Freedman, *Coherent Neutrino Nucleus Scattering as a Probe of the Weak Neutral Current, Phys. Rev. D* **9** (1974) 1389–1392.

[166] COHERENT collaboration, D. Akimov et al., *Observation of Coherent Elastic Neutrino-Nucleus Scattering, Science* **357** (2017) 1123–1126, [1708.01294].

[167] I. Brivio and M. Trott, *The Standard Model as an Effective Field Theory, Phys. Rept.* **793** (2019) 1–98, [1706.08945].

[168] *Neutrino Non-Standard Interactions: A Status Report*, vol. 2, 2019. 10.21468/SciPostPhysProc.2.001.

[169] J. Heeck and W. Rodejohann, *Gauged $L_\mu - L_\tau$ Symmetry at the Electroweak Scale, Phys. Rev. D* **84** (2011) 075007, [1107.5238].

[170] G.-y. Huang, T. Ohlsson and S. Zhou, *Observational Constraints on Secret Neutrino Interactions from Big Bang Nucleosynthesis, Phys. Rev. D* **97** (2018) 075009, [1712.04792].

[171] D. G. Cerdeño, M. Fairbairn, T. Jubb, P. A. N. Machado, A. C. Vincent and C. Bœhm, *Physics from solar neutrinos in dark matter direct detection experiments, JHEP* **05** (2016) 118, [1604.01025].

[172] D. Curtin, R. Essig, S. Gori and J. Shelton, *Illuminating Dark Photons with High-Energy Colliders, JHEP* **02** (2015) 157, [1412.0018].

[173] E. M. Riordan et al., *A Search for Short Lived Axions in an Electron Beam Dump Experiment, Phys. Rev. Lett.* **59** (1987) 755.

[174] NA64 collaboration, D. Banerjee et al., *Search for invisible decays of sub-GeV dark photons in missing-energy events at the CERN SPS, Phys. Rev. Lett.* **118** (2017) 011802, [1610.02988].

[175] TEXONO collaboration, M. Deniz et al., *Measurement of Nu(e)-bar -Electron Scattering Cross-Section with a CsI(Tl) Scintillating Crystal Array at the Kuo-Sheng Nuclear Power Reactor*, *Phys. Rev. D* **81** (2010) 072001, [0911.1597].

[176] R. Harnik, J. Kopp and P. A. N. Machado, *Exploring nu Signals in Dark Matter Detectors*, *JCAP* **07** (2012) 026, [1202.6073].

[177] M. Bauer, P. Foldenauer and J. Jaeckel, *Hunting All the Hidden Photons*, *JHEP* **07** (2018) 094, [1803.05466].

[178] M. Pospelov, A. Ritz and M. B. Voloshin, *Secluded WIMP Dark Matter*, *Phys. Lett. B* **662** (2008) 53–61, [0711.4866].

[179] C. Boehm, X. Chu, J.-L. Kuo and J. Pradler, *Scalar Dark Matter Candidates – Revisited*, 2010.02954.

[180] G. Arcadi, A. Djouadi and M. Raidal, *Dark Matter through the Higgs portal*, *Phys. Rept.* **842** (2020) 1–180, [1903.03616].

[181] J. Asaadi, E. Church, R. Guenette, B. J. P. Jones and A. M. Szelc, *New light Higgs boson and short-baseline neutrino anomalies*, *Phys. Rev. D* **97** (2018) 075021, [1712.08019].

[182] R. Primulando, J. Julio and P. Uttayarat, *Scalar phenomenology in type-II seesaw model*, *JHEP* **08** (2019) 024, [1903.02493].

[183] D. Nanda and D. Borah, *Connecting Light Dirac Neutrinos to a Multi-component Dark Matter Scenario in Gauged $B - L$ Model*, *Eur. Phys. J. C* **80** (2020) 557, [1911.04703].

[184] E. Ma and M. Maniatis, *Pseudo-Majoron as Light Mediator of Singlet Scalar Dark Matter*, *JHEP* **07** (2017) 140, [1704.06675].

[185] T. Kitabayashi, *Scalar clockwork and flavor neutrino mass matrix*, *PTEP* **2020** (2020) 123B01, [2003.06550].

[186] C. Boehm, Y. Farzan, T. Hambye, S. Palomares-Ruiz and S. Pascoli, *Is it possible to explain neutrino masses with scalar dark matter?*, Phys. Rev. D **77** (2008) 043516, [`hep-ph/0612228`].

[187] J. B. G. Alvey and M. Fairbairn, *Linking Scalar Dark Matter and Neutrino Masses with IceCube 170922A*, JCAP **07** (2019) 041, [`1902.01450`].

[188] Y. Farzan, M. Lindner, W. Rodejohann and X.-J. Xu, *Probing neutrino coupling to a light scalar with coherent neutrino scattering*, JHEP **05** (2018) 066, [`1802.05171`].

[189] J. R. Ellis, K. A. Olive, Y. Santoso and V. C. Spanos, *Update on the direct detection of supersymmetric dark matter*, Phys. Rev. D **71** (2005) 095007, [`hep-ph/0502001`].

[190] A. Crivellin, M. Hoferichter and M. Procura, *Accurate evaluation of hadronic uncertainties in spin-independent WIMP-nucleon scattering: Disentangling two- and three-flavor effects*, Phys. Rev. D **89** (2014) 054021, [`1312.4951`].

[191] M. Hoferichter, J. Ruiz de Elvira, B. Kubis and U.-G. Meißner, *High-Precision Determination of the Pion-Nucleon σ Term from Roy-Steiner Equations*, Phys. Rev. Lett. **115** (2015) 092301, [`1506.04142`].

[192] Y. Kamiya, K. Itagami, M. Tani, G. N. Kim and S. Komamiya, *Constraints on New Gravitylike Forces in the Nanometer Range*, Phys. Rev. Lett. **114** (2015) 161101, [`1504.02181`].

[193] Y. N. Pokotilovski, *Constraints on new interactions from neutron scattering experiments*, Phys. Atom. Nucl. **69** (2006) 924–931, [`hep-ph/0601157`].

[194] H. Leeb and J. Schmiedmayer, *Constraint on hypothetical light interacting bosons from low-energy neutron experiments*, Phys. Rev. Lett. **68** (1992) 1472–1475.

[195] P. S. Pasquini and O. L. G. Peres, *Bounds on Neutrino-Scalar Yukawa Coupling*, *Phys. Rev. D* **93** (2016) 053007, [1511.01811].

[196] KAMLAND-ZEN collaboration, A. Gando et al., *Limits on Majoron-emitting double-beta decays of Xe-136 in the KamLAND-Zen experiment*, *Phys. Rev. C* **86** (2012) 021601, [1205.6372].

[197] G. G. Raffelt, *Stars as laboratories for fundamental physics: The astrophysics of neutrinos, axions, and other weakly interacting particles.* 5, 1996.

[198] L. Heurtier and Y. Zhang, *Supernova Constraints on Massive (Pseudo)Scalar Coupling to Neutrinos*, *JCAP* **02** (2017) 042, [1609.05882].

[199] A. Burrows and J. M. Lattimer, *The effect of trapped lepton number and entropy on the outcome of stellar collapse*, *The Astrophysical Journal* **270** (1983) 735–739.

[200] S. Couch, *The mechanism(s) of core-collapse supernovae*, *Philos Trans A Math Phys Eng Sci* **375** (10, 2017) 20160271.

[201] A. Burrows, D. Vartanyan, J. C. Dolence, M. A. Skinner and D. Radice, *Crucial physical dependencies of the core-collapse supernova mechanism*, *Space Science Reviews* **214** (Jan, 2018) .

[202] M. Bossa, *DarkSide-50, a background free experiment for dark matter searches*, *Journal of Instrumentation* **9** (jan, 2014) C01034–C01034.

[203] M. Leyton, S. Dye and J. Monroe, *Exploring the hidden interior of the Earth with directional neutrino measurements*, *Nature Communications* **8** (2017) .

[204] G. B. Gelmini, V. Takhistov and S. J. Witte, *Casting a Wide Signal Net with Future Direct Dark Matter Detection Experiments*, *JCAP* **07** (2018) 009, [1804.01638].

[205] J. B. Dent, B. Dutta, J. L. Newstead and L. E. Strigari, *Dark matter, light mediators, and the neutrino floor*, *Phys. Rev. D* **95** (2017) 051701, [1607.01468].

[206] F. Ruppin, J. Billard, E. Figueroa-Feliciano and L. Strigari, *Complementarity of dark matter detectors in light of the neutrino background*, *Phys. Rev. D* **90** (2014) 083510, [1408.3581].

[207] J. H. Davis, *Dark Matter vs. Neutrinos: The effect of astrophysical uncertainties and timing information on the neutrino floor*, *JCAP* **03** (2015) 012, [1412.1475].

[208] C. A. J. O'Hare, A. M. Green, J. Billard, E. Figueroa-Feliciano and L. E. Strigari, *Readout strategies for directional dark matter detection beyond the neutrino background*, *Phys. Rev. D* **92** (2015) 063518, [1505.08061].

[209] L. Baudis, *WIMP Dark Matter Direct-Detection Searches in Noble Gases*, *Phys. Dark Univ.* **4** (2014) 50–59, [1408.4371].

[210] C. E. Aalseth et al., *The DarkSide Multiton Detector for the Direct Dark Matter Search*, *Adv. High Energy Phys.* **2015** (2015) 541362.

[211] G. C. McLaughlin, G. M. Fuller and J. R. Wilson, *The Influence of nuclear composition on the electron fraction in the post-core-bounce supernova environment*, *Astrophys. J.* **472** (1996) 440, [astro-ph/9701114].

[212] A. Arcones, G. Martínez-Pinedo, L. F. Roberts and S. E. Woosley, *Electron fraction constraints based on nuclear statistical equilibrium with beta equilibrium*, *Astronomy and Astrophysics* **522** (Oct, 2010) A25.

[213] H.-T. Janka, *Explosion Mechanisms of Core-Collapse Supernovae*, *Ann. Rev. Nucl. Part. Sci.* **62** (2012) 407–451, [1206.2503].

[214] R. C. Tolman, *Static solutions of Einstein's field equations for spheres of fluid*, *Phys. Rev.* **55** (1939) 364–373.

[215] J. R. Oppenheimer and G. M. Volkoff, *On Massive neutron cores*, *Phys. Rev.* **55** (1939) 374–381.

[216] S. A. Colgate and R. H. White, *The hydrodynamic behavior of supernovae explosions*, *The astrophysical journal* **143** (1966) 626.

[217] M. Rampp, R. Buras, H. T. Janka and G. Raffelt, *Core-collapse supernova simulations: variations of the input physics*, `astro-ph/0203493`.

[218] H. A. Bethe and J. R. Wilson, *Revival of a stalled supernova shock by neutrino heating*, *APJ* **295** (Aug., 1985) 14–23.

[219] H. T. Janka, *Neutrino Emission from Supernovae*, `1702.08713`.

[220] A. S. Burrows, *Neutrinos from Supernovae*, pp. 143–181. Springer New York, New York, NY, 1990. 10.1007/978-1-4612-3286-5_7.

[221] J. M. Lattimer and A. Yahil, *Analysis of the Neutrino Events from Supernova 1987A*, *APJ* **340** (May, 1989) 426.

[222] M. Cermeño, M. A. Pérez-García and J. Silk, *Diffusion of dark matter in a hot and dense nuclear environment*, *Phys. Rev. D* **94** (2016) 023509, [`1511.04071`].

[223] T. J. Leitner*Diplomarbeit: Neutrino Interactions with Nucleons and Nuclei* (2007) .

[224] T. Fischer, S. C. Whitehouse, A. Mezzacappa, F.-K. Thielemann and M. Liebendörfer, *Protoneutron star evolution and the neutrino-driven wind in general relativistic neutrino radiation hydrodynamics simulations*, *Astronomy and Astrophysics* **517** (Jul, 2010) A80.

[225] T. Fischer, G. Martínez-Pinedo, M. Hempel and M. Liebendörfer, *Neutrino spectra evolution during protoneutron star deleptonization*, *Phys. Rev. D* **85** (Apr, 2012) 083003.

[226] A. Mezzacappa and O. Messer, *Neutrino transport in core collapse supernovae*, *Journal of Computational and Applied Mathematics* **109** (1999) 281–319.

[227] J. A. Pons, S. Reddy, M. Prakash, J. M. Lattimer and J. A. Miralles, *Evolution of proto–neutron stars*, *The Astrophysical Journal* **513** (mar, 1999) 780–804.

[228] A. W. Steiner, M. Hempel and T. Fischer, *Core-collapse supernova equations of state based on neutron star observations*, *Astrophys. J.* **774** (2013) 17, [1207.2184].

[229] A. M. Suliga and I. Tamborra, *Astrophysical constraints on nonstandard coherent neutrino-nucleus scattering*, *Phys. Rev. D* **103** (2021) 083002, [2010.14545].

[230] D. A. Dicus, S. Nussinov, P. B. Pal and V. L. Teplitz, *Implications of relativistic gas dynamics for neutrino-neutrino cross sections*, *Physics Letters B* **218** (1989) 84–90.

[231] G. F. Lawler and V. Limic, *Random Walk: A Modern Introduction*. Cambridge Studies in Advanced Mathematics. Cambridge University Press, 2010, 10.1017/CBO9780511750854.

[232] J. Crank, *The mathematics of diffusion / by J. Crank*. Clarendon Press Oxford [England], 2nd ed. ed., 1975.

[233] D. Barker and D. M. Mei, *Germanium Detector Response to Nuclear Recoils in Searching for Dark Matter*, *Astropart. Phys.* **38** (2012) 1–6, [1203.4620].

[234] J. Lindhard, V. Nielsen, M. Scharff and P. V. Thomsen, *Integral equations governing radiation effects. (notes on atomic collisions, iii)*, *Kgl. Danske Videnskab., Selskab. Mat. Fys. Medd.* **33** (1, 1963) .

[235] J. Lindhard, M. Scharff and H. E. Schioett, *Range concepts and heavy ion ranges (notes on atomic collisions, ii), Kgl. Danske Videnskab. Selskab. Mat. Fys. Medd.* **33** (1, 1963) .

[236] TEXONO collaboration, A. K. Soma et al., *Characterization and Performance of Germanium Detectors with sub-keV Sensitivities for Neutrino and Dark Matter Experiments, Nucl. Instrum. Meth. A* **836** (2016) 67–82, [1411.4802].

[237] I. Lopes and S. Turck-Chièze, *Solar neutrino physics oscillations: Sensitivity to the electronic density in the Sun's core, Astrophys. J.* **765** (2013) 14, [1302.2791].

[238] Center for X-ray Optics and Advanced Light Source, Lawrence Berkeley Natl. Labor., *X-Ray Data Booklet*, 2009.

[239] H. Davoudiasl, P. B. Denton and J. Gehrlein, *Attractive scenario for light dark matter direct detection, Phys. Rev. D* **102** (2020) 091701, [2007.04989].

[240] J.-W. Chen, H.-C. Chi, K.-N. Huang, H.-B. Li, C. P. Liu, L. Singh et al., *Constraining neutrino electromagnetic properties by germanium detectors, Phys. Rev. D* **91** (2015) 013005, [1411.0574].

[241] B. M. Roberts and V. V. Flambaum, *Electron-interacting dark matter: Implications from DAMA/LIBRA-phase2 and prospects for liquid xenon detectors and NaI detectors, Phys. Rev. D* **100** (2019) 063017, [1904.07127].

[242] B. M. Roberts, V. A. Dzuba, V. V. Flambaum, M. Pospelov and Y. V. Stadnik, *Dark matter scattering on electrons: Accurate calculations of atomic excitations and implications for the DAMA signal, Phys. Rev. D* **93** (2016) 115037, [1604.04559].

[243] R. Essig, J. Mardon and T. Volansky, *Direct Detection of Sub-GeV Dark Matter, Phys. Rev. D* **85** (2012) 076007, [1108.5383].

[244] R. Essig, A. Manalaysay, J. Mardon, P. Sorensen and T. Volansky, *First Direct Detection Limits on sub-GeV Dark Matter from XENON10*, *Phys. Rev. Lett.* **109** (2012) 021301, [1206.2644].

[245] R. Essig, T. Volansky and T.-T. Yu, *New Constraints and Prospects for sub-GeV Dark Matter Scattering off Electrons in Xenon*, *Phys. Rev. D* **96** (2017) 043017, [1703.00910].

[246] B. G. Streetman, *Solid state electronic devices / Ben G. Streetman and Sanjay Banerjee.* Prentice Hall series in solid state physical electronics. Prentice Hall, Upper Saddle River, N.J, 5th ed. ed., 2000.

[247] C. Kittel, *Introduction to Solid State Physics.* Wiley, 8 ed., 2004.

[248] P. K. Misra, *Chapter 4 - nearly free electron model*, in *Physics of Condensed Matter* (P. K. Misra, ed.), pp. 95–130. Academic Press, Boston, 2012. DOI.

[249] S. Clark, M. Segall, C. Pickard, P. Hasnip, M. Probert, K. Refson et al., *First principles methods using castep*, *Zeitschrift für Kristallographie* **220** (2005) 567–570.

[250] P. J. Hasnip, K. Refson, M. I. Probert, J. R. Yates, S. J. Clark and C. J. Pickard, *Density functional theory in the solid state*, *Philosophical Transactions of the Royal Society A: Mathematical, Physical and Engineering Sciences* **372** (2014) 20130270.

[251] M. Segall, P. J. Lindan, M. a. Probert, C. J. Pickard, P. J. Hasnip, S. Clark et al., *First-principles simulation: ideas, illustrations and the castep code*, *Journal of physics: condensed matter* **14** (2002) 2717.

[252] R. Essig, M. Fernandez-Serra, J. Mardon, A. Soto, T. Volansky and T.-T. Yu, *Direct Detection of sub-GeV Dark Matter with Semiconductor Targets*, *JHEP* **05** (2016) 046, [1509.01598].

[253] J.-W. Chen, H.-C. Chi, K.-N. Huang, C. P. Liu, H.-T. Shiao, L. Singh et al., *Atomic ionization of germanium by neutrinos from an ab initio approach*, *Phys. Lett. B* **731** (2014) 159–162, [1311.5294].

[254] J.-W. Chen, H.-C. Chi, H.-B. Li, C. P. Liu, L. Singh, H. T. Wong et al., *Constraints on millicharged neutrinos via analysis of data from atomic ionizations with germanium detectors at sub-keV sensitivities*, *Phys. Rev. D* **90** (2014) 011301, [1405.7168].

[255] W. Johnson, C. Lin, K. Cheng and C. Lee, *Relativistic random-phase approximation*, *Physica Scripta* **21** (1980) 409.

[256] J. Conrad, *Statistical Issues in Astrophysical Searches for Particle Dark Matter*, *Astropart. Phys.* **62** (2015) 165–177, [1407.6617].

[257] S. Knapen, T. Lin and K. M. Zurek, *Light Dark Matter: Models and Constraints*, *Phys. Rev. D* **96** (2017) 115021, [1709.07882].

[258] Muon g-2 collaboration, B. Abi et al., *Measurement of the Positive Muon Anomalous Magnetic Moment to 0.46 ppm*, *Phys. Rev. Lett.* **126** (2021) 141801, [2104.03281].

[259] H. Schmidt-Böcking, L. Schmidt, H. J. Lüdde, W. Trageser, A. Templeton and T. Sauer, *The stern-gerlach experiment revisited*, *The European Physical Journal H* **41** (Oct, 2016) 327364.

[260] P. A. M. Dirac, *The Quantum theory of electron. 2.*, *Proc. Roy. Soc. Lond. A* **118** (1928) 351.

[261] J. Schwinger, *On quantum-electrodynamics and the magnetic moment of the electron*, *Phys. Rev.* **73** (Feb, 1948) 416–417.

[262] Muon g-2 collaboration, G. W. Bennett et al., *Final Report of the Muon E821 Anomalous Magnetic Moment Measurement at BNL*, *Phys. Rev. D* **73** (2006) 072003, [hep-ex/0602035].

[263] S. Borsanyi et al., *Leading-order hadronic vacuum polarization contribution to the muon magnetic momentfrom lattice QCD*, 2002.12347.

[264] A. Crivellin, M. Hoferichter, C. A. Manzari and M. Montull, *Hadronic vacuum polarization: $(g-2)_\mu$ versus global electroweak fits*, 2003.04886.

[265] J. Cao, Y. He, J. Lian, D. Zhang and P. Zhu, *Electron and Muon Anomalous Magnetic Moments in the Inverse Seesaw Extended NMSSM*, 2102.11355.

[266] E. Ma, D. P. Roy and S. Roy, *Gauged L(mu) - L(tau) with large muon anomalous magnetic moment and the bimaximal mixing of neutrinos, Phys. Lett. B* **525** (2002) 101–106, [hep-ph/0110146].

[267] K. Harigaya, T. Igari, M. M. Nojiri, M. Takeuchi and K. Tobe, *Muon g-2 and LHC phenomenology in the $L_\mu - L_\tau$ gauge symmetric model, JHEP* **03** (2014) 105, [1311.0870].

[268] A. Biswas, S. Choubey and S. Khan, *FIMP and Muon $(g-2)$ in a $U(1)_{L_\mu - L_\tau}$ Model, JHEP* **02** (2017) 123, [1612.03067].

[269] W. Altmannshofer, S. Gori, S. Profumo and F. S. Queiroz, *Explaining dark matter and B decay anomalies with an $L_\mu - L_\tau$ model, JHEP* **12** (2016) 106, [1609.04026].

[270] K. Asai, K. Hamaguchi, N. Nagata, S.-Y. Tseng and K. Tsumura, *Minimal Gauged $U(1)_{L_\alpha - L_\beta}$ Models Driven into a Corner, Phys. Rev. D* **99** (2019) 055029, [1811.07571].

[271] M. Pospelov, *Secluded U(1) below the weak scale, Phys. Rev. D* **80** (2009) 095002, [0811.1030].

[272] M. Escudero, D. Hooper, G. Krnjaic and M. Pierre, *Cosmology with A Very Light $L_\mu - L_\tau$ Gauge Boson, JHEP* **03** (2019) 071, [1901.02010].

[273] W. L. Freedman, *Cosmology at a Crossroads, Nature Astron.* **1** (2017) 0121, [1706.02739].

[274] A. G. Riess et al., *A 2.4% Determination of the Local Value of the Hubble Constant*, Astrophys. J. **826** (2016) 56, [`1604.01424`].

[275] B. Follin and L. Knox, *Insensitivity of the distance ladder Hubble constant determination to Cepheid calibration modelling choices*, Mon. Not. Roy. Astron. Soc. **477** (2018) 4534–4542, [`1707.01175`].

[276] A. G. Riess, L. Macri, S. Casertano, M. Sosey, H. Lampeitl, H. C. Ferguson et al., *A redetermination of the hubble constant with thehubble space telescopefrom a differential distance ladder*, The Astrophysical Journal **699** (Jun, 2009) 539563.

[277] PLANCK collaboration, P. A. R. Ade et al., *Planck 2015 results. XIII. Cosmological parameters*, Astron. Astrophys. **594** (2016) A13, [`1502.01589`].

[278] J. L. Bernal, L. Verde and A. G. Riess, *The trouble with H_0*, JCAP **10** (2016) 019, [`1607.05617`].

[279] J. N. Bahcall, M. H. Pinsonneault and S. Basu, *Solar models: Current epoch and time dependences, neutrinos, and helioseismological properties*, Astrophys. J. **555** (2001) 990–1012, [`astro-ph/0010346`].

[280] M. Blennow, T. Ohlsson and H. Snellman, *Day-night effect in solar neutrino oscillations with three flavors*, Phys. Rev. D **69** (2004) 073006, [`hep-ph/0311098`].

[281] J. Heeck, M. Lindner, W. Rodejohann and S. Vogl, *Non-Standard Neutrino Interactions and Neutral Gauge Bosons*, SciPost Phys. **6** (2019) 038, [`1812.04067`].

[282] N. Grevesse and A. J. Sauval, *Standard Solar Composition*, Space Sci. Rev. **85** (May, 1998) 161–174.

[283] S. Basu and H. Antia, *Seismic measurement of the depth of the solar convection zone*, *Monthly Notices of the Royal Astronomical Society* **287** (1997) 189–198.

[284] M. Asplund, N. Grevesse and A. J. Sauval, *The Solar Chemical Composition*, in *Cosmic Abundances as Records of Stellar Evolution and Nucleosynthesis* (I. Barnes, Thomas G. and F. N. Bash, eds.), vol. 336 of *Astronomical Society of the Pacific Conference Series*, p. 25, Sept., 2005.

[285] E. Caffau, H.-G. Ludwig, M. Steffen, B. Freytag and P. Bonifacio, *Solar chemical abundances determined withǎaǎco5bold 3d model atmosphere*, *Solar Physics* **268** (Mar, 2010) 255269.

[286] A. M. Serenelli, W. C. Haxton and C. Pena-Garay, *Solar models with accretion. I. Application to the solar abundance problem*, *Astrophys. J.* **743** (2011) 24, [`1104.1639`].

[287] D. G. Cerdeno, J. H. Davis, M. Fairbairn and A. C. Vincent, *CNO Neutrino Grand Prix: The race to solve the solar metallicity problem*, *JCAP* **04** (2018) 037, [`1712.06522`].

[288] BOREXINO collaboration, M. Agostini et al., *Experimental evidence of neutrinos produced in the CNO fusion cycle in the Sun*, *Nature* **587** (2020) 577–582, [`2006.15115`].

[289] G. Bellini et al., *Precision measurement of the 7Be solar neutrino interaction rate in Borexino*, *Phys. Rev. Lett.* **107** (2011) 141302, [`1104.1816`].

[290] Y. Kaneta and T. Shimomura, *On the possibility of a search for the $L_\mu - L_\tau$ gauge boson at Belle-II and neutrino beam experiments*, *PTEP* **2017** (2017) 053B04, [`1701.00156`].

[291] LZ collaboration, D. S. Akerib et al., *The LUX-ZEPLIN (LZ) Experiment*, *Nucl. Instrum. Meth. A* **953** (2020) 163047, [`1910.09124`].

[292] PANDAX collaboration, X. Cao et al., *PandaX: A Liquid Xenon Dark Matter Experiment at CJPL, Sci. China Phys. Mech. Astron.* **57** (2014) 1476–1494, [1405.2882].

[293] L. Baudis, A. Ferella, A. Kish, A. Manalaysay, T. Marrodan Undagoitia and M. Schumann, *Neutrino physics with multi-ton scale liquid xenon detectors, JCAP* **01** (2014) 044, [1309.7024].

[294] LUX collaboration, D. Akerib et al., *Improved Limits on Scattering of Weakly Interacting Massive Particles from Reanalysis of 2013 LUX Data, Phys. Rev. Lett.* **116** (2016) 161301, [1512.03506].

[295] XENON collaboration, E. Aprile et al., *Low-mass dark matter search using ionization signals in XENON100, Phys. Rev. D* **94** (2016) 092001, [1605.06262].

[296] B. Lenardo et al., *Measurement of the ionization yield from nuclear recoils in liquid xenon between 0.3 - 6 keV with single-ionization-electron sensitivity,* 1908.00518.

[297] DARKSIDE collaboration, P. Agnes et al., *Low-Mass Dark Matter Search with the DarkSide-50 Experiment, Phys. Rev. Lett.* **121** (2018) 081307, [1802.06994].

[298] M. Abdullah, J. B. Dent, B. Dutta, G. L. Kane, S. Liao and L. E. Strigari, *Coherent elastic neutrino nucleus scattering as a probe of a Z' through kinetic and mass mixing effects, Phys. Rev. D* **98** (2018) 015005, [1803.01224].

[299] W. Altmannshofer, S. Gori, J. Martín-Albo, A. Sousa and M. Wallbank, *Neutrino Tridents at DUNE, Phys. Rev. D* **100** (2019) 115029, [1902.06765].

[300] P. Ballett, M. Hostert, S. Pascoli, Y. F. Perez-Gonzalez, Z. Tabrizi and R. Zukanovich Funchal, *Z's in neutrino scattering at DUNE, Phys. Rev. D* **100** (2019) 055012, [1902.08579].

[301] G. Krnjaic, G. Marques-Tavares, D. Redigolo and K. Tobioka, *Probing Muonphilic Force Carriers and Dark Matter at Kaon Factories*, Phys. Rev. Lett. **124** (2020) 041802, [1902.07715].